UNIVERSITY OF STRATHCLYDE
Department of Physics

Novel micro-pixelated III-nitride light emitting diodes: fabrication, efficiency studies and applications

by

Pengfei Tian

A thesis presented in fulfilment of the
requirements for the degree of
Doctor of Philosophy

September 2014

Declaration of Authorship

This thesis is the result of the author's original research. It has been composed by the author and has not been previously submitted for examination which has led to the award of a degree.

Signed: _____

Date: _____

Frontispiece

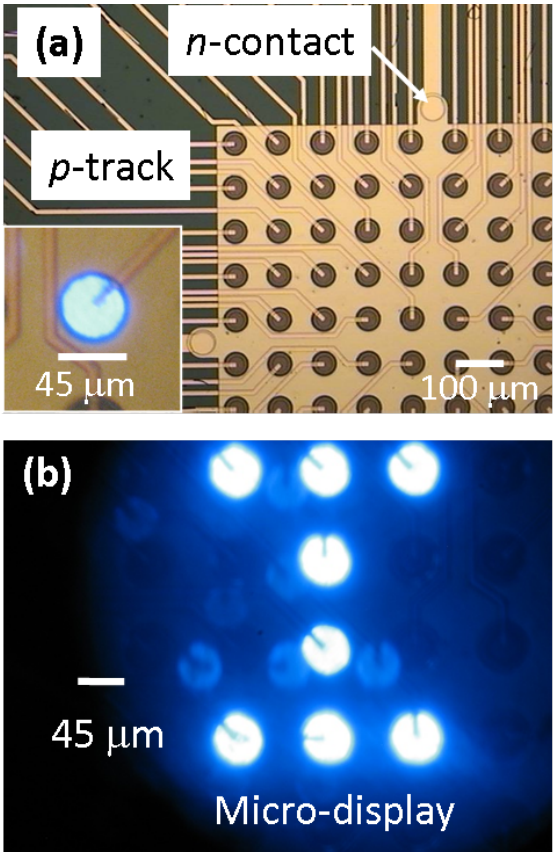

Micrographs of an individually addressable (a) 10×10 micro-LEDs array on a Si substrate (inset at bottom left: light emission through the spreading layer of a representative pixel) and (b) light emission of a simple micro-display pattern from the array.

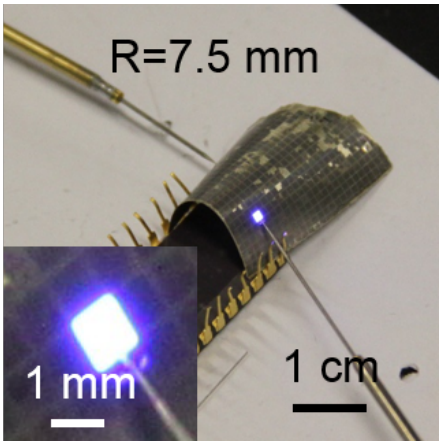

Optical images of flexible vertical LEDs with substrate bending radius of ∼7.5 mm. The inset shows the uniform light emission within an LED die.

To my family

Acknowledgements

This PhD work was completed in Prof. Martin D. Dawson's group in the Institute of Photonics, University of Strathclyde. This thesis would not have been completed without the advice and help of many people.

First of all, I'd like to thank my supervisor, Dr. Erdan Gu, who gave me the opportunity to study here. He has spent lots of valuable time on applying for my PhD funding, experiment design, paper and help with thesis writing, and even career development. I am thankful for his guidance, patience and encouragement throughout my studies.

I'd also like to thank everyone who has helped me. In particular, I would like to thank Prof. Martin D. Dawson for providing the excellent research environment and guiding my research, Dr. Ian M. Watson for providing many valuable suggestions for my experiments and paper writing, Dr. Jonathan Mckendry for giving me huge help on the device characterization and research progress, Dr. Zheng Gong for training me on the LED fabrication, Dr. Anthony E. Kelly for instructing me on the LED bandwidth measurement and analysis, Dr. Benoit Guilhabert for training my operation of AFM, PL and interference lithography setups, Dr. Johannes Herrnsdorf for LATEX and MATLAB programmings, and Prof. Robert Martin, Dr. Paul Edwards and Michael Wallace for the SEM, CL, and integrating sphere tests.

Finally, I am indebted to my parents, who brought me up and give invaluable love and support throughout my life. I'd like to express my gratitude to my wife Shihan Zeng for her selfless love.

My PhD study was financially funded by Scottish Universities Physics Alliance, China Scholarship Council, Overseas Research Students Awards Scheme, and University of Strathclyde. The work was also supported by the Engineering and Physical Sciences Research Council Grant No. EP/K00042X/1.

Publications

Papers

Drafted

[1] **P. Tian**, J. J. D. McKendry, J. Herrnsdorf, S. Watson, R. Ferreira, I. M. Watson, E. Gu, A. E. Kelly, and M. D. Dawson, "Temperature dependent efficiency droop of blue InGaN micro-light emitting diodes", submitted.

Published

[2] W. Yang, S. Zhang, J. J. D. McKendry, J. Herrnsdorf, **P. Tian**, Z. Gong, Q. Ji, I. M. Watson, E. Gu, M. D. Dawson, L. Feng, C. Wang, and X. Hu, "Size-dependent capacitance study on InGaN-based micro-light-emitting diodes", *Journal of Applied Physics*, **116**, 044512 (2014).

[3] **P. Tian**, J. J. D. McKendry, Z. Gong, S. Zhang, S. Watson, D. Zhu, I. M. Watson, E. Gu, A. E. Kelly, C. J. Humphreys, and M. D. Dawson, "Characteristics and applications of micro-pixelated GaN-based light emitting diodes on Si substrates", *Journal of Applied Physics*, **115**, 033112 (2014).

[4] **P. Tian**, J. J. D. McKendry, Z. Gong, B. Guilhabert, I. M. Watson, E. Gu, Z. Chen, G. Zhang, and M. D. Dawson, "Size-dependent efficiency and efficiency droop of blue InGaN micro-light emitting diodes", *Applied Physics Letters*, **101**, 231110 (2012).

[5] **P. Tian**, E. Xie, Z. Gong, Z. Chen, T. Yu, Y. Sun, S. Qi, Y. Chen, Y. Zhang, S. Calvez, E. Gu, G. Zhang, and M. D. Dawson, "Flexible vertical structure GaN-based light emitting diodes on an AuSn substrate", in *Proceedings of IEEE Photonics 2011 Conference*, 551 (2012).

[6] S. Zhang, Z. Gong, J. J. D. McKendry, S. Watson, A. Cogman, E. Xie, **P. Tian**, E. Gu, Z. Chen, G. Zhang, A. E. Kelly, R. K. Henderson, and M. D. Dawson, "CMOS-controlled color-tunable smart display", *IEEE Photonics Journal*, **4**, 1639 (2012).

Conference presentations

[7] **P. Tian**, J. J. D. McKendry, Z. Gong, S. Zhang, S. Watson, D. Zhu, I. M. Watson, E. Gu, A. E. Kelly, C. J. Humphreys, and M. D. Dawson, "Characteristics and applications of micro-pixelated GaN-based light emitting diodes on Si substrates" (Oral), *IEEE Photonics Conference 2013* (Bellevue Washington, USA, September 2013).

[8] **P. Tian**, J. J. D. McKendry, Z. Gong, S. Zhang, S. Watson, D. Zhu, I. M. Watson, E. Gu, A. E. Kelly, C. J. Humphreys, and M. D. Dawson, "Micro-pixelated GaN-based light emitting diodes on Si substrates" (Oral), *10th International Conference on Nitride Semiconductors* (Washington, D.C., USA, August 2013).

[9] **P. Tian**, J. J. D. McKendry, Z. Gong, S. Watson, D. Zhu, I. M. Watson, E. Gu, A. E. Kelly, C. J. Humphreys, and M. D. Dawson, "Micro-pixelated GaN-based light emitting diodes on Si substrates" (Poster), *UK Nitrides Consortium 2013 Annual Conference* (Cardiff, UK, January 2013).

[10] **P. Tian**, "Flexible GaN-Based light emitting diodes and size-dependent efficiency droop of micro-LEDs" (Poster), *CM-DTC Induction Meeting and Careers Event* (Dundee, United Kingdom, September 2012).

[11] S. Zhang, Z. Gong, J. J. D. McKendry, S. Watson, A. Cogman, E. Xie, **P. Tian**, E. Gu, Z. Chen, G. Zhang, A. E. Kelly, R. K. Henderson, and M. D. Dawson, "CMOS-controlled color-tunable smart display" (Oral), *IEEE Photonics 2012 Conference* (California, USA, September 2012).

[12] **P. Tian**, J. J. D. McKendry, E. Gu, Z. Gong, B. Guilhabert, Z. Chen, G. Zhang, and M. D. Dawson, "Size-dependent efficiency and efficiency droop of blue InGaN micro-light emitting diodes" (Oral), *International Symposium on Semiconductor Light Emitting Devices* (Berlin, Germany, July 2012).

[13] **P. Tian**, "Poised to light up the world: study the efficiency droop of light emitting diodes" (Poster), *University of Strathclyde Research Day 2012* (Glasgow, United Kingdom, June, 2012).

[14] **P. Tian**, E. Xie, Z. Gong, Z. Chen, T. Yu, Y. Sun, S. Qi, Y. Chen, Y. Zhang, S. Calvez, E. Gu, G. Zhang, and M. D. Dawson, "Flexible vertical structure GaN-based light emitting diodes on an AuSn substrate" (Oral), *IEEE Photonics Conference 2011* (Arlington, USA, October 2011).

Abstract

This thesis presents a systematic study of the fabrication, efficiency and applications of micro-pixelated III-nitride light emitting diodes (micro-LEDs). Efficiency droop studies of micro-LEDs and the development of new-types of micro-LEDs have been investigated. The size dependence and temperature dependence of micro-LED efficiency droop have been analysed, providing a deep understanding of efficiency droop issue for general lighting and also demonstrating the advantages of micro-LEDs to alleviate such efficiency droop. Micro-LEDs on flexible substrates have been fabricated, which combine the flexibility of soft substrates and the high efficiency of inorganic LEDs for potential applications in flexible displays, biomedicine, etc. In addition, micro-LEDs on Si substrates were also fabricated to reduce the micro-LED device fabrication cost.

The size-dependent efficiency droop study demonstrates that the smaller micro-LEDs have more uniform current spreading, which causes their higher efficiency and higher thermal saturation current density. In addition, the temperature-dependent efficiency droop study shows that both the radiative and Auger recombination coefficients decrease with increasing temperature, and the temperature dependence of the radiative and Auger recombination coefficients is weaker at a higher current density. So micro-LEDs possess stabler temperature dependent efficiency when operating at a high current density.

Flexible micro-LEDs have been fabricated using metal bonding and laser lift off techniques with only one transfer step. Also, the micro-LED arrays on Si substrates were developed for the first time, which have lower fabrication cost compared with micro-LEDs on sapphire substrates. The applications in micro-display and visible light communication have been demonstrated for both the devices above.

This work suggests that employing micro-LED techniques is a way to improve LED efficiency for general lighting. With development of flexible micro-LEDs and reduced fabrication cost of micro-LEDs on Si substrates, the future applications of micro-LEDs are expected to be greatly expanded.

Contents

List of Figures

List of Tables

Chapter 1

Introduction

Micro-pixelated gallium nitride (GaN)-based light emitting diodes (micro-LEDs), devices of typically square or disc-like format with smaller edge length/diameters (e.g. 40 μm) than commonly used broad-area LEDs (typically $\geq$300 μm), have demonstrated high efficiency, excellent heat dissipation, short carrier lifetime, and localized light emission compared with broad-area LEDs. Thus such micro-LEDs have applications in micro-displays, visible light communication (VLC), solid-state lighting (SSL), optogenetics and so on, and developing novel micro-LEDs is helpful to further expand their applications. For most of these applications, micro-LEDs are usually operated at a very high current density (up to tens of kA/cm^2), however, the micro-LEDs suffer from efficiency droop at high current density. It is worth mentioning that efficiency droop is also a significant problem for the wide applications of GaN-based broad-area LEDs in general SSL. Therefore, the efficiency droop study of micro-LEDs is important to help explain the carrier recombination dynamics responsible and to suggest the possible approaches to improve LED performance in general.

In this thesis, the efficiency droop of micro-LEDs with different sizes and under different temperatures is investigated. Then, to expand their applications, flexible micro-LEDs and micro-LEDs on Si substrates were fabricated and characterized. The potential applications of these novel LED devices in micro-displays and VLC were also successfully demonstrated.

This chapter first provides a brief history of LED development, mainly focussing on material development and efficiency improvement of LEDs. Then, the fabrication and

applications of GaN-based LEDs are reviewed. The applications of GaN-based micro-LEDs in micro-displays and VLC are also introduced. The final section details the operation principles, characteristics and efficiency droop study of GaN-based LEDs.

1.1 Development of LEDs

Various sources for white-light emission have been developed since the invention of incandescent light bulbs in the late 1800s. Of these, LED based white-light sources have significant advantages in terms of energy consumption, environmental protection, human health, and so on [1–3]. These advantages of LEDs come from the high luminous efficiency of LEDs compared with other commonly used white-light sources, especially incandescent and fluorescent sources for general lighting, as shown in figure 1.1 [4–6]. The luminous efficiency of LEDs is the conversion efficiency of electrical power to luminous flux [4]. LED development has been comparably short but has progressed rapidly [1].

The earliest electroluminescent (EL) emission was found from the semiconductor SiC near a metal point contact over 100 years ago [7]. As developed subsequently, all commercial LEDs in the visible range are based on III-V compound semiconductors. These compounds consist of elements belonging to group III, aluminium (Al), gallium (Ga) and indium (In), and group V, nitrogen (N), phosphorus (P) and arsenic (As), as shown in figure 1.1 [4, 8]. Red LEDs based on $GaAs_{1-x}P_x$ were introduced commercially in 1962, however for x>0.45, $GaAs_{1-x}P_x$, such LEDs have low emission efficiency due to the indirect bandgap of the material. This problem was solved in the mid 1970s by introduction of nitrogen to induce a direct bandgap and enhance emission efficiency of $GaAs_{1-x}P_x$ LEDs [9]. More details of the indirect/direct bandgap will be described in section 1.3.1.2. The red, orange and yellow LED efficiency was further enhanced by introduction of double heterostructures in the 1980s and using AlInGaP based material in 1990s [10]. The fabrication technology significantly affects the LED efficiency. Figure 1.1 shows a dramatic increase of LED efficiency upon the technology development of metal-organic chemical vapour deposition (MOCVD), also known as metal organic vapour phase epitaxy (MOVPE), for AlInGaP LEDs. Comparably, the initial blue LEDs made from SiC (also indirect bandgap) had much lower efficiency. Later, with the introduction of

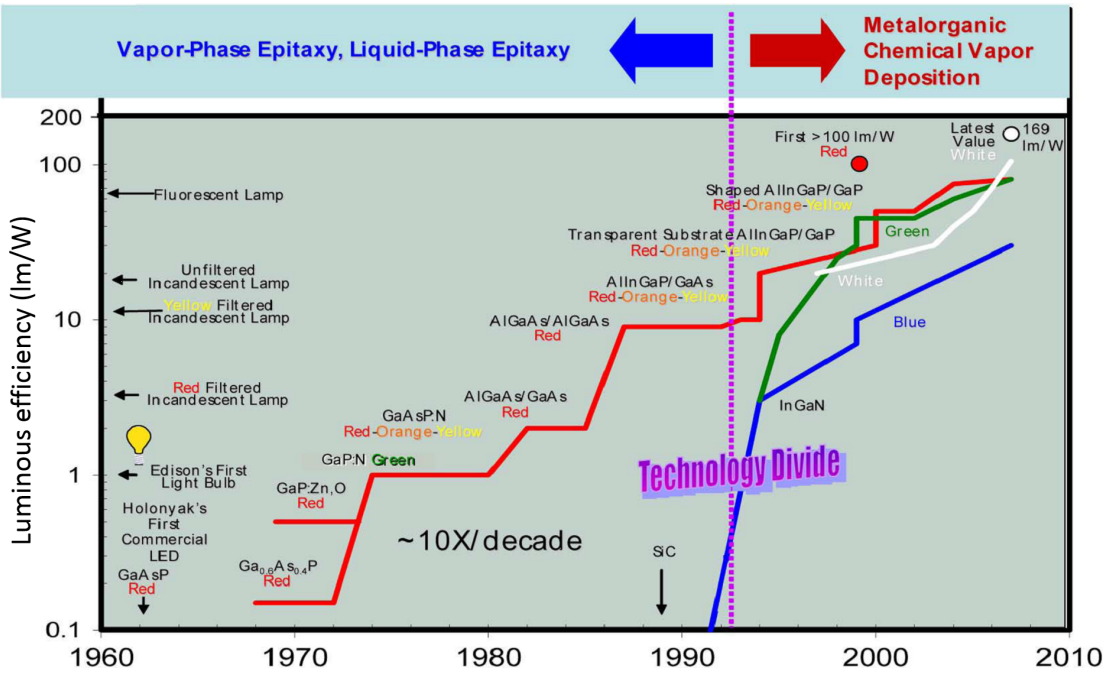

FIGURE 1.1: History of LED development from 1962 and LED efficiency comparison with other conventional lighting sources. From [4].

III-nitride compounds, high efficiency LEDs became commercially available at blue and green wavelengths.

The III-nitride compound materials were first reported in 1907 [11] and the growth of GaN films was reported in 1969 [12]. It was not until 1971, however, that the important breakthroughs began to be achieved, as follows. GaN was successfully grown by MOCVD [13], which is the most commonly used growth technique today. In 1986, Akasaki and Amano obtained smooth-surface GaN films using AlN buffer layers on sapphire substrates, bringing significant quality improvement of two-dimensional films [14]. It took several years to conquer the difficulty to fabricate p-GaN films. In 1989, activated by low-energy electron-beam irradiation (LEEBI), Mg-doped p-GaN films were demonstrated [15]. In 1992, Nakamura used the alternative technique of thermal annealing to achieve superior hole concentrations in p-GaN [16]. These developments were the key techniques for commercializing blue III-V LEDs by Nichia in 1994.

The characteristics of bandgap versus lattice constant of these III-V materials are shown in figure 1.2 [3]. For the III-phosphide material system, GaAs bulk substrates are commercially available and can be used for high quality $(Al_x, Ga_{1-x})_{1-y}In_yP$ based device growth by both MOCVD and molecular-beam epitaxy (MBE) methods. The bandgap

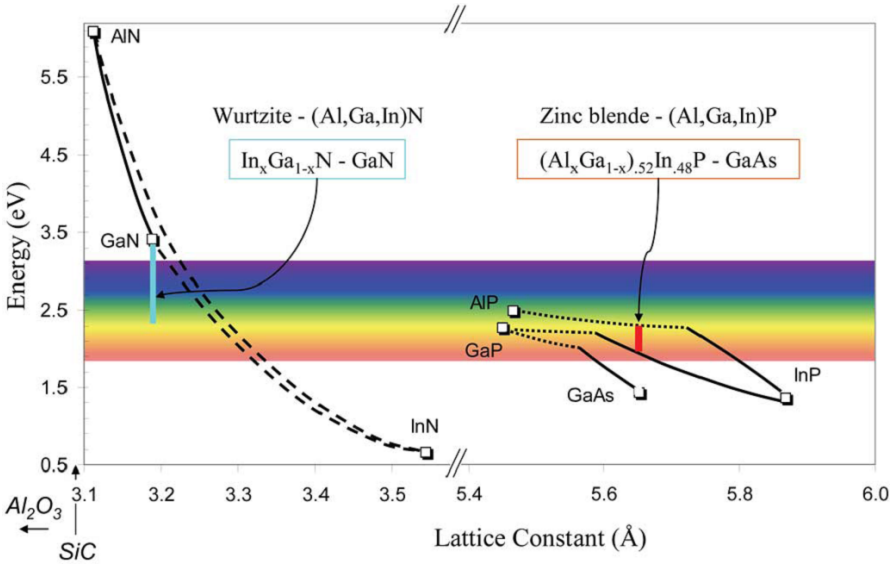

FIGURE 1.2: Energy bandgap versus lattice constant for III-V materials. From [3].

and emission wavelength of these materials can be adjusted by changing x and y parameters to achieve the bandgap from deep red ~1.9 eV (~650 nm) to yellow-green ~2.2 eV (~560 nm). For the $In_xGa_{1-x}N$ material system, through increasing the InN mole fraction from $x = 0$ to $x = 1$, the emission bandgap changes from UV ~3.4 eV (~365 nm) to infrared ~0.7 eV (~1800 nm). Although high brightness blue and green LEDs have been achieved [1, 2], some limitations still remain for some InGaN compositions. First, InGaN based LEDs are usually grown on sapphire substrates. The large lattice mismatch between GaN (3.189 Å) and sapphire (4.759 Å) leads to high dislocation densities, although over two decades of development the dislocation densities have been reduced from $\sim 10^{10}$ to $\sim 10^8$ cm^{-2} . Other growth technologies on Si, SiC, and GaN bulk substrates also have limitations. In addition, growth of InGaN on GaN results in compressive strain in InGaN layers, so a large built-in electric field is induced by spontaneous and piezoelectric polarizations. Finally, due to the miscibility characteristics of InGaN material, it is difficult to form high quality InGaN films with high InN content.

Based on the above issues, external quantum efficiency (η_{EQE}) of the high-power LED is shown in figure 1.3 [3]. η_{EQE} is the ratio of the number of photons escaping from LEDs to the number of injected carriers. It can be seen that the η_{EQE} of the green LED is significantly lower than for shorter-wavelength InGaN-based blue LEDs and longer-wavelength AlGaInP-based red LEDs. This is well-known as the "green gap"[17]. For white LEDs, mixing the light from red-green-blue (RGB) LEDs is one efficient way to improve the colour rendering index (CRI), compared with current white LEDs produced

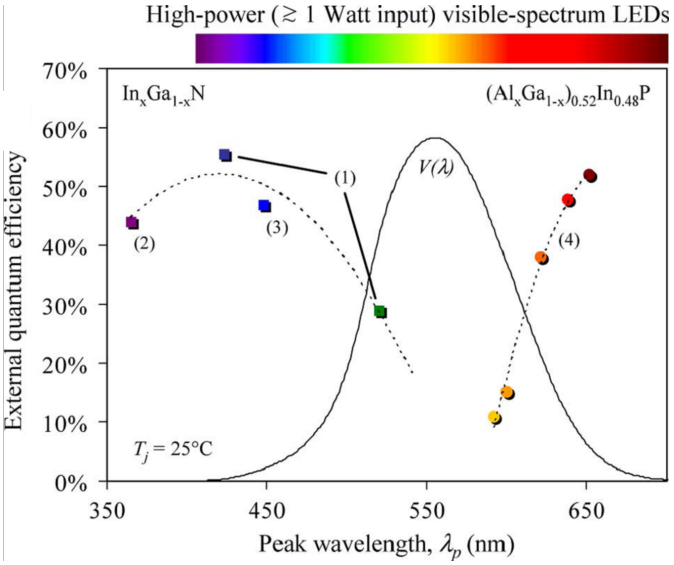

FIGURE 1.3: External quantum efficiencies of high-power LEDs at room temperature: (1) InGaN freestanding thin film LEDs; (2) InGaN vertical thin film LEDs; (3) InGaN conventional chips with patterned substrate; (4) AlGaInP LEDs. V(λ) is the luminous eye response curve. From [3].

from phosphor conversion mixing of blue LEDs. CRI is a quantitative measure of the ability of a light source to reveal the object colours compared with a natural light source. However, high-quality RGB white LEDs have not been produced due to the "green gap".

1.2 Overview of GaN-based LEDs

Among these materials for LED fabrication, GaN-based alloys are the focus of this work on micro-LED research. The techniques for micro-LED fabrication are partly compatible with the conventional broad-area LED fabrication. Thus, this section first gives an overview of common broad-area GaN-based LEDs, including growth, chip designs, packaging and applications. However, compared with broad-area LEDs, the fabrication techniques, characteristics and applications of micro-LEDs also show large differences, as demonstrated in the later section.

1.2.1 GaN-based broad-area LEDs

Growth

Hydride vapour phase epitaxy (HVPE), MBE, and MOCVD techniques have been successfully used for the growth of GaN-based films and LED structures. Of these, MOCVD

is most commonly used for commercial production. InGaN and AlGaN can be grown by gas-source precursors including trimethylgallium ($Ga(CH_3)_3$), trimethylaluminum ($Al(CH_3)_3$), trimethylindium ($In(CH_3)_3$), and ammonia (NH_3). Typical GaN structures are grown on [0001] sapphire substrates. A low-temperature AlN or GaN buffer layer is deposited at 550 °C, followed by GaN epitaxy at 700-1100 °C. The carrier concentration of n-type GaN and p-type GaN can be controlled by silicon (Si) and magnesium (Mg) doping, respectively [8]. The GaN crystal structure is shown in figure 1.4 [18].

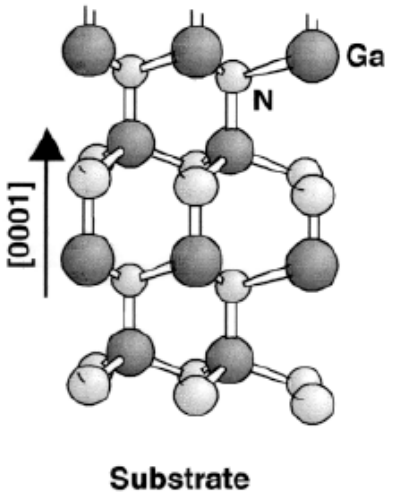

FIGURE 1.4: Wurtzite GaN crystal structure. From [18].

The first GaN-based blue LEDs were grown by Nichia in 1994, with an InGaN/AlGaN double heterostructure [19]. In the same year, candela-class blue-green LEDs were fabricated through increased In content in the InGaN layers. The GaN-based LEDs were insensitive to high threading dislocation (TD) densities in the films, compared with LEDs fabricated with other materials. Shown in figure 1.5 is a transmission electron microscopy (TEM) image of a typical GaN-based LED structure with TD density of 10^{10} cm^{-2} [20]. The dislocations appear as dark lines propagating in a direction normal to the substrate. Furthermore, through spatially resolved catholuminescence (CL) spectrum mapping of an InGaN quantum well (QW), In composition fluctuation has been confirmed [21], which indicates that carrier localization in In-rich area may explain the TD insensitive emission. The illustration of a QW structure is shown in figure 1.6 with a small-bandgap semiconductor layer as the QW/active region and two large-bandgap semiconductor layers as the barrier regions. The injected carriers are confined to the QW and then recombine giving photon emission. In GaN-based LEDs, an InGaN/GaN QW structure is commonly employed.

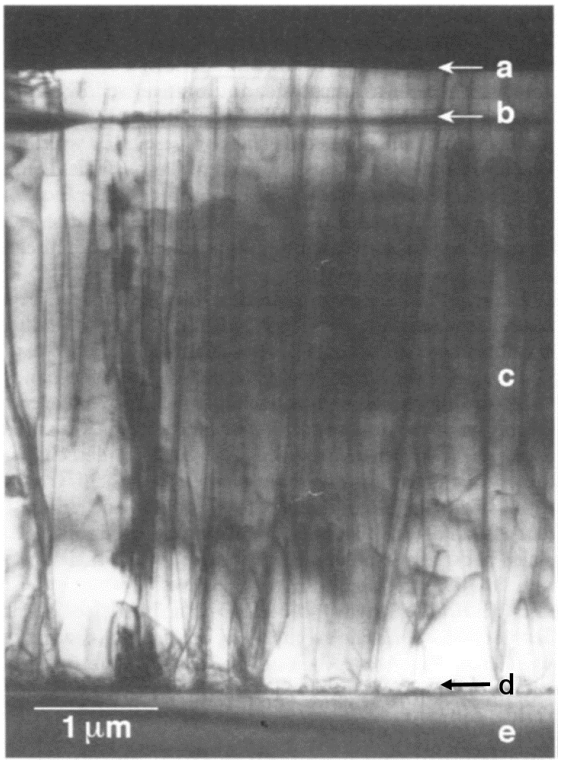

FIGURE 1.5: Cross-sectional TEM image of a typical blue LED with TD density of 10^{10} cm^{-2}. (a)-(e) represent the top surface, active region, GaN film, buffer layer, and sapphire substrate, respectively. From [8, 20].

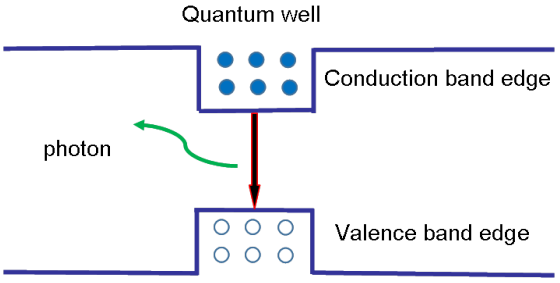

FIGURE 1.6: Illustration of a typical QW structure.

LED chip designs

LED chip design is important for the light extraction efficiency and heat dissipation of LEDs, which has been a challenge for decades [3]. Several different designs have been reported for GaN-based LEDs as shown in figure 1.7.

Conventional chip design is commonly employed for GaN-based LEDs grown on sapphire substrates which are not electrically conducting. In figure 1.7(a), LED mesas are achieved by etching down the epitaxial structure to n-type GaN layer and then an n-type ohmic contact/pad is formed. The p-type GaN layer does not provide good current spreading without a semi-transparent current spreading layer. Usually Ni/Au or indium-tin-oxide

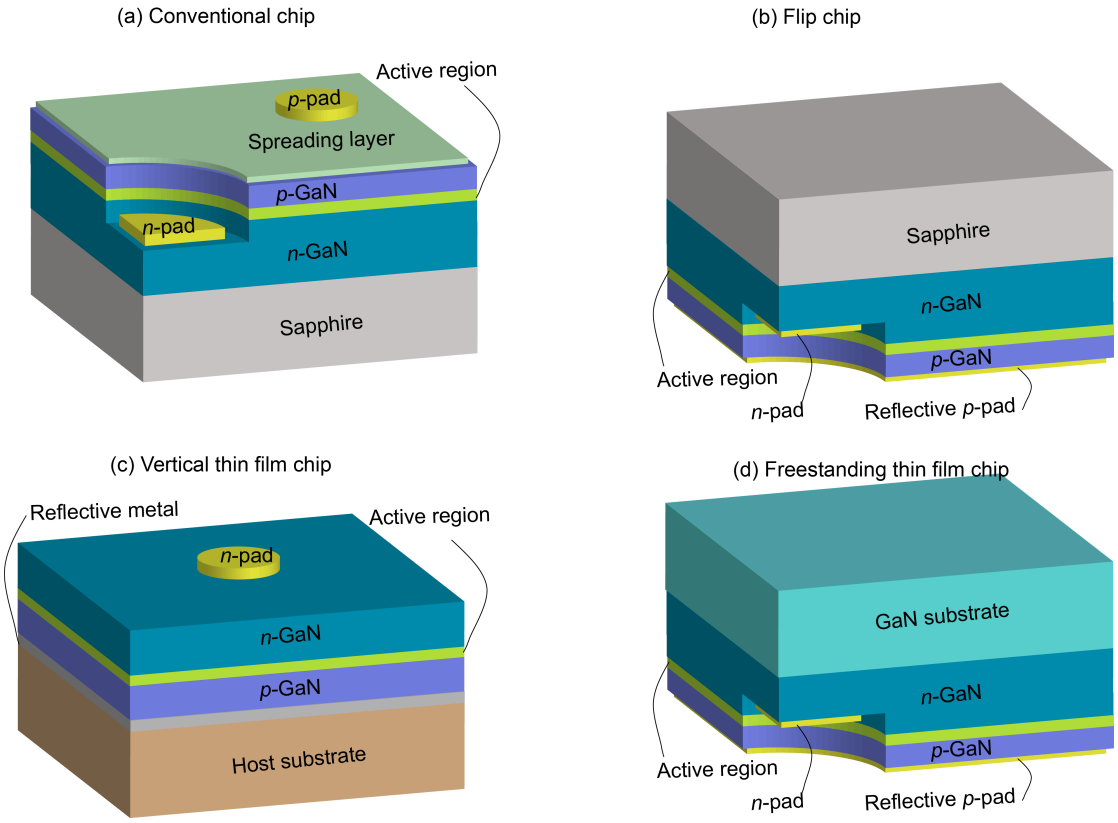

FIGURE 1.7: GaN-based LED chip designs: (a) conventional chip, (b) flip chip, (c) vertical thin film chip, and (d) freestanding thin film chip. Reproduced from [3].

(ITO) is used for current spreading in conventional chips. In addition, for this design, sapphire substrates provide poor heat dissipation which further limits the power output of LEDs.

Flip chip design could partly solve the problems of conventional chip by extracting the emitted light through sapphire substrates as shown in figure 1.7(b). In this design, thick reflective metal can be deposited on p-type GaN to improve the current spreading and light reflection. Then, solder or Au-Au bump attach mount can be used for connecting the chip to cathode and anode. In this design, the QWs are also close to the package heat sink, allowing excellent heat dissipation.

The third design is the vertical thin film chip as shown in figure 1.7(c). The LED epitaxial layers grown on sapphire substrates are first bonded onto host substrates with good heat dissipation, such as Si, Cu, etc. Then, laser lift-off (LLO) technology is employed to remove the sapphire substrate. As n-type GaN has lower electrical resistivity compared with p-type GaN, a semi-transparent current spreading layer is not required. Also the top surface of n-GaN can be textured to improve light extraction efficiency. In addition,

the quality of LED epitaxial layers grown on Si substrates has been greatly improved recently, so removing Si substrates by wet chemical etching is possible and then vertical thin film chip can be fabricated with similar processing steps to those shown in figure 1.7(c) [22–24].

Another design is freestanding thin film LEDs using thick GaN as substrates, as shown in figure 1.7(d). For this structure, LED epitaxial layers are grown on thick GaN films, so the quality of the epitaxial layer can be greatly improved compared with LEDs grown on sapphire substrates. Usually the thick GaN films are prepared by HVPE growth. An alternative way is to grow thick GaN buffer layer on sapphire substrates by HVPE, and then grow the LED epitaxial layers by MOCVD, after which LLO can be employed to remove the sapphire substrates and to achieve a freestanding wafer. The freestanding LED design not only benefits high-quality LED structure growth, but also facilitates the heat dissipation.

LED packaging

The reliability and lifetime of LEDs are strongly influenced by the device packaging. To package white LEDs for SSL, a phosphor material needs to be used to produce yellow emission excited by the blue InGaN LED as shown in figure 1.8(a). The mixed blue and yellow light can provide white light with a colour temperature in the 4000-8000 K range, as well as a CRI in the 70-80 range [3].

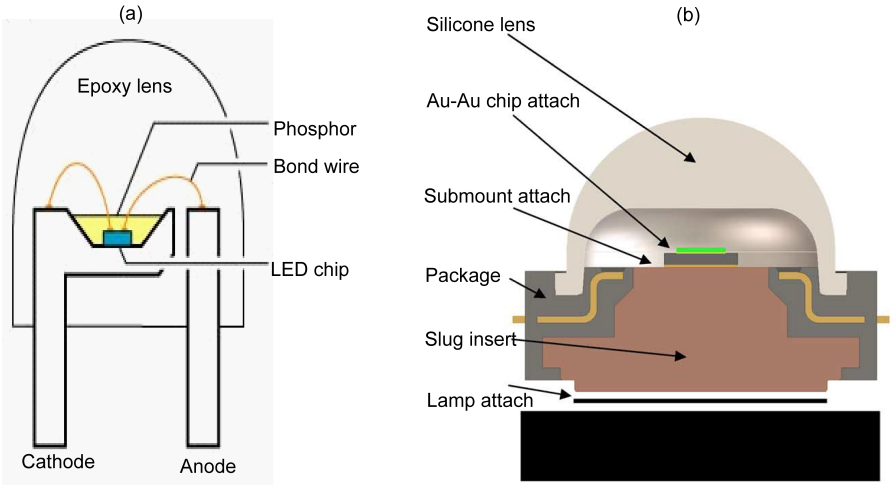

FIGURE 1.8: (a) Typical low power LED package with epoxy lens. Adapted from [25]. (b) High power LED package. Adapted from [3].

Figure 1.8(a) shows a typical low power LED package. The LED chip is bonded to a reflector cup in a cathode lead. The LED is connected to the cathode and anode leads

by bond wires. The epoxy can reduce the internal reflection at the epoxy/air interface, as the angle of emitted light at the epoxy/air interface is near normal.

A high power LED package with excellent thermal dissipation is shown in figure 1.8(b). The package contains a heatsink metal slug with low thermal resistivity and the LED submount is bonded to this heatsink by metal solder. Similar to the low power LED package, the attached silicone lens serves to improve LED light extraction.

Applications

The most important application of LEDs is general SSL. Through replacing the incandescent lamps now and fluorescent tubes in the future by LED-based lamps, great reduction of worldwide energy consumption is expected. The current commercial LEDs have much higher efficiency than incandescent lamps, as well as smaller size and much longer lifetime (more than 50000 hours) [26].

Automotive forward lighting (headlight) is another important application for LEDs, through directing the emitted light in specific direction. Due to the small size of LEDs, the precise emitting area not only facilitates a better radiation pattern to improve visibility, but also allows compact and multifunctional design of forward lighting.

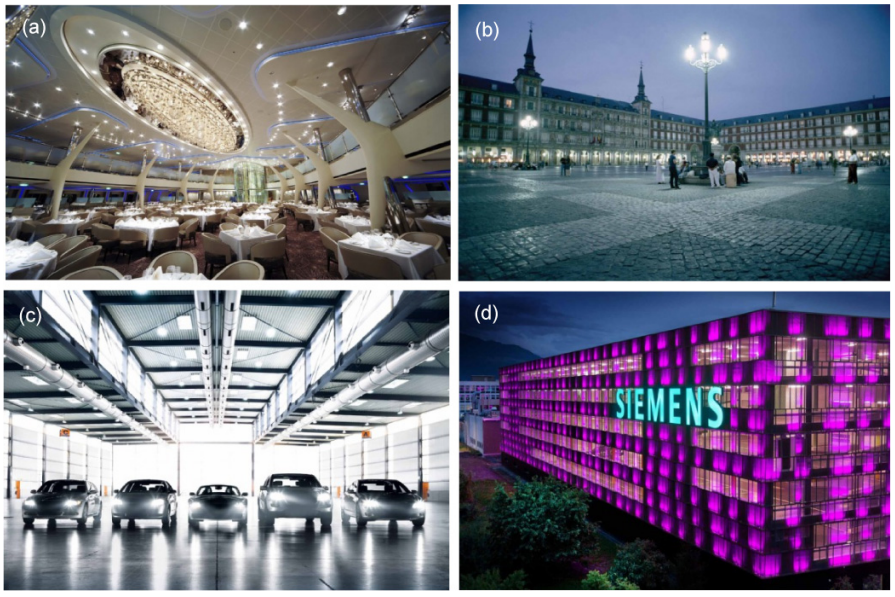

FIGURE 1.9: (a)Indoor lighting of a restaurant. (b)Outdoor city and street lighting. (c)Passenger car lighting. (d)Profile lettering signal. From Osram [27].

Also, the low power consumption, saturated colours, and high-speed switching help to expand the applications of LEDs in backlighting of TVs and cellphones, signals for traffic, and the flash of digital cameras, etc.

Figure 1.9 demonstrates some applications of such LEDs [27], including indoor, outdoor and car lighting, and profile lettering signals.

1.2.2 Micro-pixelated GaN-based LEDs

Due to the smaller sizes, micro-LEDs (e.g. 40 μm) have higher external quantum efficiency, much better thermal dissipation ability, and can sustain much higher current densities than broad area LEDs (e.g. 300 μm). The self-heating effect and spectral shift of micro-LEDs have been investigated [28, 29]. In particular, the efficiency droop of micro-LEDs has been studied in this work [30]. In addition, small-size micro-LED arrays can be achieved with each pixel addressable individually. Based on these special characteristics, micro-LEDs have been used for various applications, including micro-displays [31], single chip AC-LEDs for SSL [32], visible light communication (VLC) [33, 34], direct LED writing [35], emitter arrays for optogenetics [36, 37], and optical tweezing systems [38]. This thesis will focus on the applications of novel micro-LEDs in micro-displays and visible light communication, and therefore we mainly discuss these two applications in this section.

Application in self-emissive micro-displays

GaN-based micro-displays have an area typically less than 1 square inch, and high brightness, high efficiency and robustness compared with the micro-displays based on liquid crystal on silicon (LCOS), digital light processor (DLP), and organic LEDs (OLEDs). Furthermore, these emissive micro-displays can be magnified to form an enlarged image or a projected image for potential applications in head-mounted displays, video headsets, and projection TV [32].

Usually two basic kinds of driving schemes are used to operate the micro-displays. Passive driving through X-Y scanning is a low cost method, while active driving is based on each driving cell corresponding to each pixel, suitable for high resolution micro-displays. In a passive-driving micro-display, each micro-LED pixel is connected with an anode (p-line) in the columns and a cathode (n-line) in the rows, as shown in figure 1.10(a) and (b).

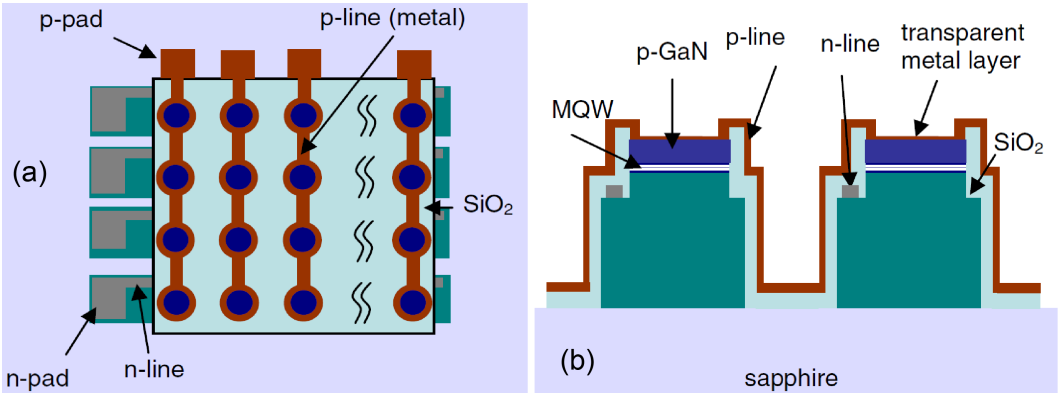

FIGURE 1.10: Structure of passive-driven micro-display in (a) top and (b) cross-section views. From [32].

To achieve high resolution micro-displays, active matrix driving is chosen [31]. Figure 1.11(a) shows a schematic structure of a flip-chip bonded micro-display on a CMOS driver by indium bump bonding. The displayed image of penguins in figure 1.11(b) was taken from the transparent sapphire side. All the micro-LED pixels share one n-type contact and the p-type contact of each pixel is bonded to the CMOS. The image of an individually addressable 640 $\times$ 480 micro-LED array is shown in figure 1.11(c). For this micro-display, the LED pixel has a size of 12 μm and the diameter of the indium bump is only $\sim$6 μm.

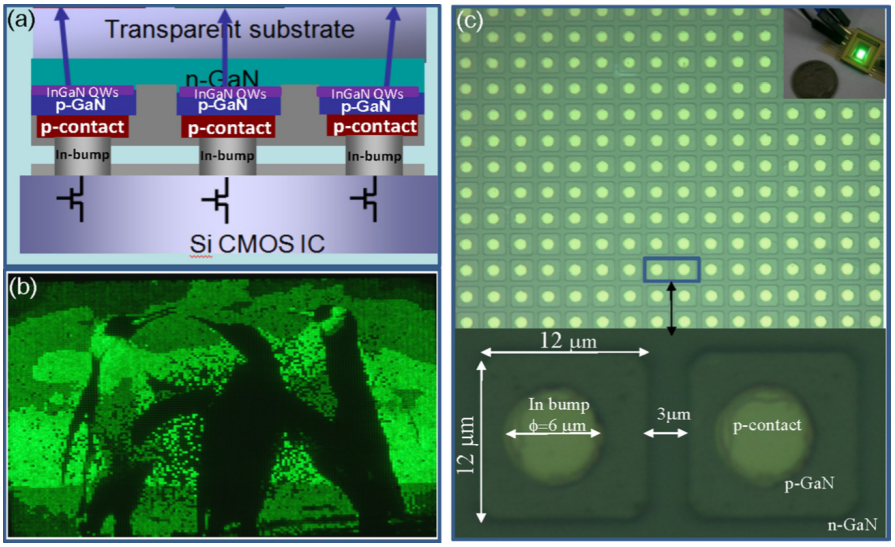

FIGURE 1.11: (a) Structure of a micro-LED array bonded onto a CMOS driver by indium bumps. (b) A gray scale projected image of penguins from a green GaN-based micro-display. (c) The images of micro-LED pixels and indium bumps from the sapphire side. The top inset shows a fully assembled green micro-display in operation. From [31].

Application in visible light communication

Micro-LEDs also show advantages in application to VLC in both free-space and fibre-based embodiments. Akhter et al. achieved a data transmission rate of 200 Mbit/s over 100 m plastic optical fibre (POF) by a green resonant cavity LED (RCLED) [39]. Free-space VLC using LEDs is also rapidly advancing. Vučić et al. demonstrated a 513 Mbit/s data transmission rate based on a white LED with a bandwidth of ~35 MHz [40]. McKendry et al. reported optical modulation bandwidth of blue micro-LEDs up to 245 MHz and an error-free data transmission rate up to 1 Gbit/s [34]. Through using a Gallium-doped ZnO current spreading layer, a high modulation bandwidth of 225.4 MHz and light output power of 1.6 mW of a blue LED were obtained by Liao et al. [41]. Of these, micro-LEDs show very high achievable modulation bandwidths without requiring specialised structures [33].

Figure 1.12(a) shows optical -3 dB frequency response bandwidth versus injection current for a 450 nm micro-LED with diameter 72 μm. The frequency responses of micro-LEDs at a current of 20 mA with different wavelengths 370 nm, 405 nm and 450 nm are shown in figure 1.12(b). In figure 1.12(c), eye diagrams at data transmission rates of 155, 622,

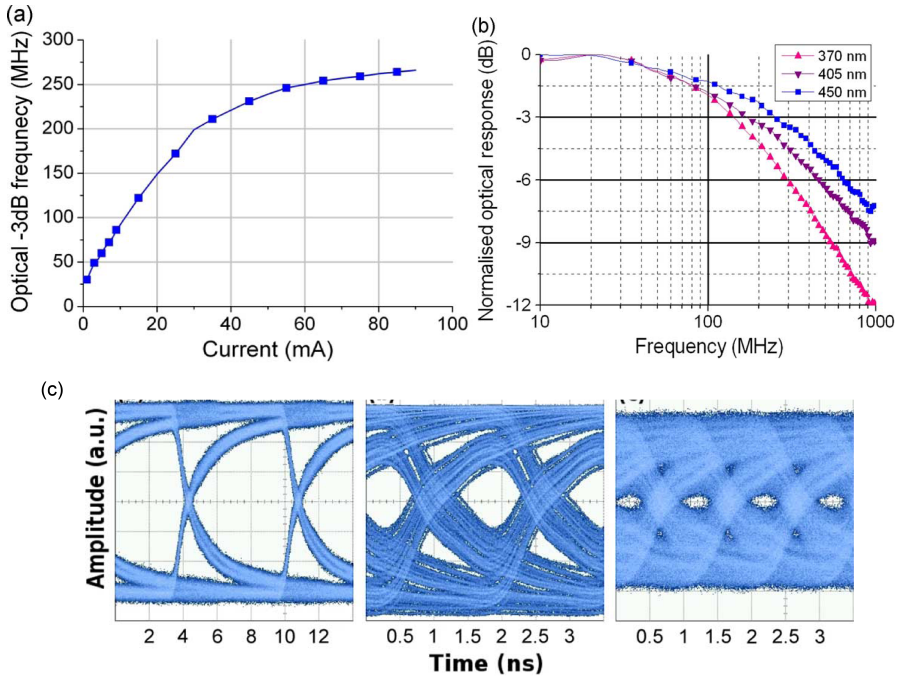

FIGURE 1.12: (a)Bandwidth of a 450 nm micro-LED. (b) Frequency responses for micro-LEDs with different wavelength, 370 nm, 405 nm and 450 nm, at current 20 mA. (c) Eye diagrams of blue 450 nm micro-LEDs at 40 mA, with data transmission rate of 155, 622 and 1000 Mbit/s. The micro-LED size is 72 μm in diameter. From [34].

and 1000 Mbit/s are shown, demonstrating that a high error-free data transmission rate could be achieved [34].

1.3 Efficiency droop of GaN-based LEDs

The efficiency of GaN-based LEDs has been continuously improved over the last two decades. However, the present GaN-based LEDs only deliver high efficiency at low current and thus low brightness. The high efficiency at high current is required for high-brightness applications, but the LEDs show reduced efficiency at high current, termed "efficiency droop".

This section first discusses the operation principles of LEDs, including the basic physics to explain their electrical and optical characteristics. Then the efficiency droop mechanisms and potential remedies are reviewed.

1.3.1 LED operation principles

1.3.1.1 Electrical properties

An abrupt p-n junction is considered with a donor concentration N_D and an acceptor concentration N_A. Assuming all dopants are fully ionized and no compensation of the dopants occurs, the free electron and hole concentrations are expressed as $n = N_D$ and $p = N_A$, respectively.

In a p-n junction under zero bias, electrons on the n-type side diffuse to the p-type side and holes on the p-type side diffuse to the n-type side. The electrons encounter many holes and the holes encounter many electrons. After the electron-hole recombination, a depletion region is formed near the p-n junction in absence of free carriers. Thus, the ionized donors and acceptors in the space charge region produce a diffusion voltage.

The band diagrams of a p-n junction under zero bias and forward bias V are shown in figure 1.13(a) and (b), respectively. In figure 1.13(a), the diffusion voltage V_D and the width of depletion region W_D are shown. From figure 1.13(a), the following equation is obtained:

$$eV_D - E_g + (E_F - E_V) + (E_C - E_F) = 0 \tag{1.1}$$

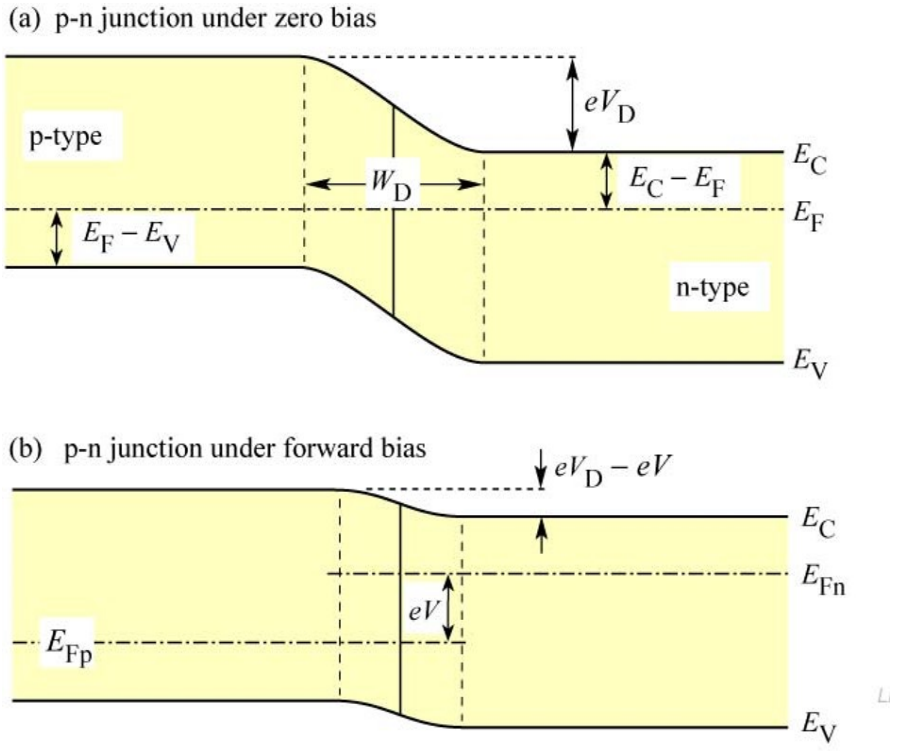

FIGURE 1.13: *P-n* junction under (a) zero bias and (b) forward bias. From [25].

where V_D is the diffusion voltage, E_g is the bandgap, and E_F, E_C and E_V are the Fermi level, the bottom of the conduction band, and the top of the valence band, respectively.

The current versus voltage (I-V) characteristics of a p-n junction can be derived from the band diagram in figure 1.13(b). Under a forward bias, electrons and holes diffuse into the regions with opposite conductivity type, after which the carriers recombine and emit photons. The I-V characteristics of the p-n junction can be expressed by the Shockley equation:

$$I = eA\left(\sqrt{\frac{D_p}{\tau_p}}\frac{{n_i}^2}{N_D} + \sqrt{\frac{D_n}{\tau_n}}\frac{{n_i}^2}{N_A}\right)\left(e^{eV/kT} - 1\right) \tag{1.2}$$

where A is the diode cross-sectional area, n_i is the intrinsic carrier concentration, $D_{n,p}$ and $\tau_{n,p}$ are the electron and hole diffusion constants and electron and hole minority carrier lifetime, respectively.

At a typical current of 20 mA, the forward voltage of a GaN-based LED is higher than for those made by other semiconductor materials [25], which is caused by the large bandgap

discontinuities, less mature contact technology, low conductivity of p-type GaN, and parasitic resistance of the n-type buffer layer.

The typical I-V characteristics of GaN-based LEDs at different temperatures are shown in figure 1.14(a) [42]. Three domains named I, II, and III are distinguished. An equivalent electric circuit with three resistors is used to interpret the three domains as shown in figure 1.14(b). The first resistor R_j is related to the space charge zone. The second resistor R_{sh} is related to the leakage current in shunt with R_j. The third one R_s is the series resistor as mentioned which causes a larger forward LED voltage.

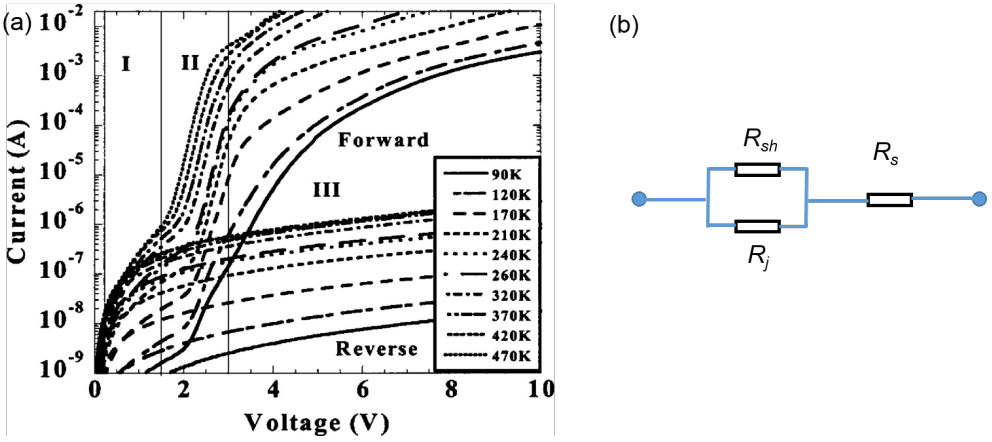

FIGURE 1.14: (a)Typical I-V characteristics of GaN-based LEDs under different temperatures for forward and reverse biases. Three domains can be defined due to different mechanisms. From [42]. (b)The equivalent electric circuit for the LEDs.

From figure 1.14(b), the relation of current and voltage is expressed as

$$I = (V - R_s I)\,(1/R_j + 1/R_{sh})\,. \tag{1.3}$$

In domain I, both forward and reverse I-V curves show the same characteristics and thus should be interpreted in the same way. Under low forward bias (V<1.5V) and reverse bias, the resistances have the relations: $R_j \gg R_{sh} \gg R_s$, so the leakage current dominates and the current can be described by $I \approx V/R_{sh}$. The LED leakage current may be caused by dislocations and the sidewall damage due to dry etching [43, 44].

In domain II (1.5 V<V<3 V), the carrier injection becomes high and the resistances follow the relations: $R_{sh} \gg R_j \gg R_s$. In this case, the current can be expressed as: $I \approx V/R_j$. The dependence of current on voltage is interpreted by drift diffusion model followed by recombination in neutral zones or by the generation-recombination process in

the space charge zone or by both [45, 46]. In GaN-based LEDs, radiative recombination mainly takes place in the nearest QW from the p-GaN side [47]. This phenomenon is caused by the low mobility of holes and the energy barrier that the holes have to cross to populate the QW, while electrons can easily populate the QW nearest to p-GaN. Therefore, in this domain, the carrier transport is mainly limited by hole injection [42].

In domain III (V>3 V), the p-n junction can be considered as a short-circuit. The resistances have relations: $R_{sh} \gg R_s \gg R_j$, so the current can be expressed as $I \approx V/R_s$. The R_s is mainly determined by the p-GaN, p-contact, and so on. The series resistance R_s can be evaluated at a high voltage ($V > E_g/e$). At a sufficiently high voltage, the I-V characteristics tend to be linear and the series resistance can be expressed as $R_s = dV/dI$ [25].

1.3.1.2 Optical properties

LED efficiency calculation

The emission photon energy of an LED with a bandgap E_g is given by $h\nu \approx E_g$, where h is Planck's constant and ν is the frequency of the photon. In an ideal LED, every carrier injected to the QWs will generate a photon, resulting an internal quantum efficiency (η_{IQE}) of unity. The η_{IQE} is defined as [25]

$$\eta_{IQE} = \frac{P_{int}/h\nu}{I/e} \tag{1.4}$$

where P_{int} is the optical power emitted from QWs and I is the injected current. As the photons may be reabsorbed by the LED substrate and the metal contacts, not all the photons emitted from QWs can escape to the free space. In addition, total internal reflection will significantly reduce the light extraction possibility from the QWs. For InGaN LEDs, the refractive index of InGaN is ~2.4 which will cause a large light reflection possibility at the GaN/air interface. The light extraction efficiency is defined as

$$\eta_{EXE} = \frac{P/h\nu}{P_{int}/h\nu} \tag{1.5}$$

where P is the optical power emitted into the free space. With η_{IQE} and η_{EXE}, the external quantum efficiency is defined as

$$\eta_{EQE} = \frac{P/h\nu}{I/e} = \eta_{IQE} \cdot \eta_{EXE} \tag{1.6}$$

The wall-plug efficiency (η_{WPG}) or power efficiency is defined as

$$\eta_{WPG} = \frac{P}{IV} \tag{1.7}$$

where IV is the input electrical power of the LED.

Emission spectrum

Spontaneous recombination of electron-hole pairs causes the photon emission from LEDs and this process is illustrated in figure 1.15(a) for direct-bandgap materials. The minimal-energy state in the conduction band and maximal-energy state in the valence band are each characterized by a wave vector k. The direct-bandgap materials have the same k-vectors, while the indirect-bandgap material have different k-vectors. In figure 1.15(a), electrons in the conduction band and holes in the valence band have energy $E_e = E_C + \hbar^2k^2/2m_e^*$ and $E_h = E_V - \hbar^2k^2/2m_h^*$, respectively, where m_e^* and m_h^* are the electron and hole effective masses, $\hbar$ is Planck's constant divided by 2π, k is the wave number, and E_V and E_C are the valence and conduction band edges, respectively.

Due to energy conservation, the photon energy is given by the difference between the electron energy E_e and hole energy E_h: $h\nu = E_e - E_h \approx E_g$. Thus, the emission wavelength of an LED is determined by the bandgap of the semiconductor material used. If the electron and hole momenta are same (as for direct-bandgap materials), the photon energy can be expressed as

$$h\nu = E_C + \frac{\hbar^2k^2}{2m_e^*} - E_V + \frac{\hbar^2k^2}{2m_h^*} = E_g + \frac{\hbar^2k^2}{2m_r^*}, \tag{1.8}$$

where m_r^* is the reduced mass, which can be expressed as $1/m_r^* = 1/m_e^* + 1/m_h^*$.

The density of states for bulk material is calculated as

$$\rho\left(E\right) = \frac{1}{2\pi^2}\left(\frac{2m_r^*}{\hbar^2}\right)^{3/2}\sqrt{E - E_g}. \tag{1.9}$$

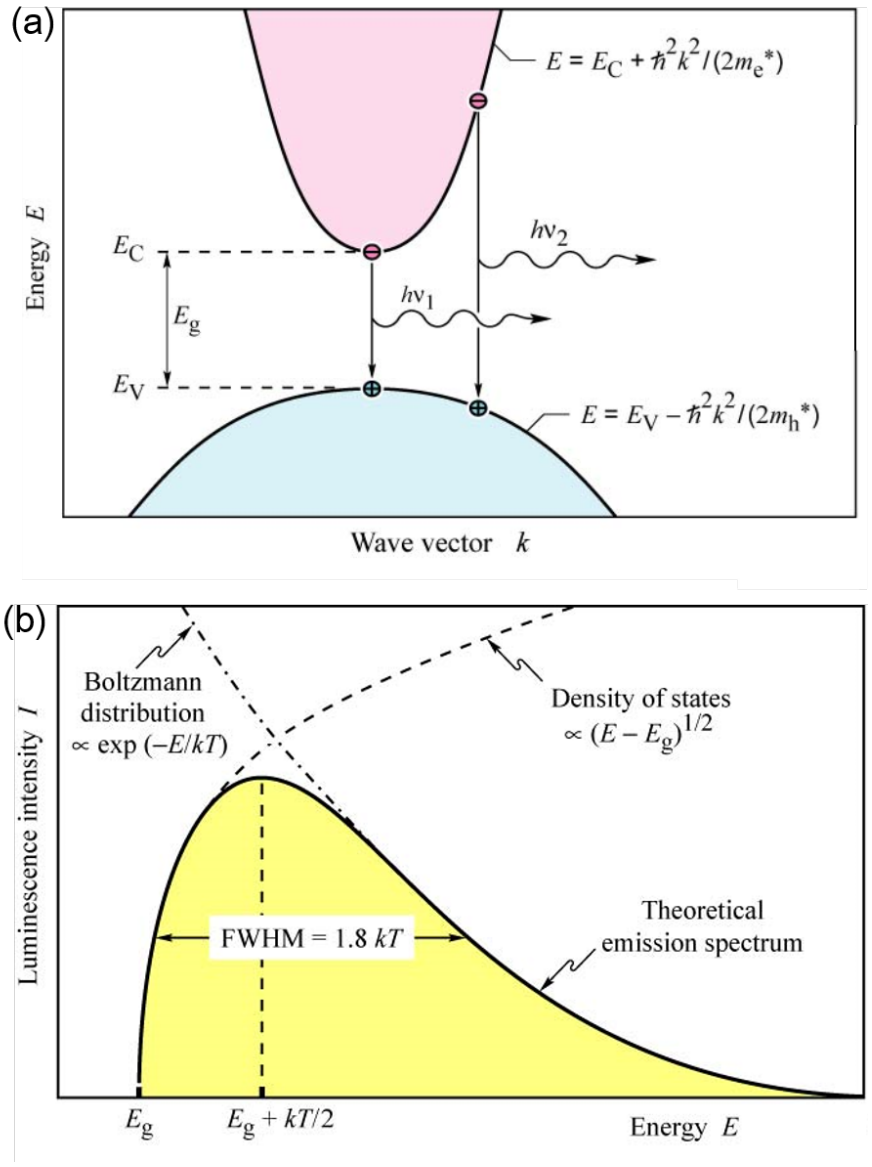

FIGURE 1.15: (a) Processes of electron-hole recombination and photon emission. (b) Schematic emission spectrum. From [25].

The distribution of carriers is determined by Boltzmann distribution:

$$f_B(E) = e^{-E/(kT)}. \tag{1.10}$$

Thus, the emission intensity can be calculated as

$$I(E) \propto \sqrt{E - E_g} e^{-E/(kT)}. \tag{1.11}$$

Then, the theoretical LED emission spectrum can be obtained as shown in figure 1.15(b). The maximum emission intensity is at $E = E_g + kT/2$, and full-width at half-maximum

of the emission is $\Delta E = 1.8kT$ [25].

1.3.2 Mechanisms of efficiency droop

For practical applications, LEDs need to be driven at high current for high brightness, however, the LED efficiency suffers from efficiency droop at high current. Efficiency droop occurs over a broad spectrum of GaN-based LEDs at various temperatures. Several mechanisms have been proposed to explain the efficiency droop, including Auger recombination, electron leakage, carrier delocalization, etc. [48] Various technologies have been developed to alleviate the efficiency droop based on these mechanisms. In this section, a general overview of the efficiency droop mechanisms is given.

1.3.2.1 Current components for LED efficiency calculation

It has been shown in equation 1.6 that LED efficiency can be expressed as $\eta_{EQE} = \eta_{IQE} \cdot \eta_{EXE}$. Both η_{IQE} and η_{EXE} may cause efficiency droop, however reduction of η_{IQE} with higher current is believed to be the key reason for efficiency droop. The η_{IQE} can be defined as the ratio of the current fraction I_{rad} that participates in the radiative recombination inside the QWs to the total current I

$$\eta_{IQE} = \frac{I_{rad}}{I} = \frac{I_{rad}}{I_{rad} + I_{lost}}. \tag{1.12}$$

As shown in figure 1.16, the total current can be split up into the current that generates photons I_{rad} in QWs and the current that is lost in other processes I_{lost}. When I_{lost} increases stronger than I_{rad} at higher current, the efficiency droop begins. The non-radiative recombination processes inside the QWs are either defect-related Schockley-Read-Hall (SRH) recombination I_{SRH} or Auger recombination I_{Auger}. The non-radiative current outside the QWs is electron leakage $I_{leakage}$. Therefore, the total current can be expressed as:

$$I = I_{rad} + I_{SRH} + I_{Auger} + I_{leakage}. \tag{1.13}$$

The total carrier recombination inside the QWs can be expressed by a simple ABC model [48]

$$I_{QW} = I_{SRH} + I_{rad} + I_{Auger} = qV_{active}\left(An + Bn^2 + Cn^3\right), \tag{1.14}$$

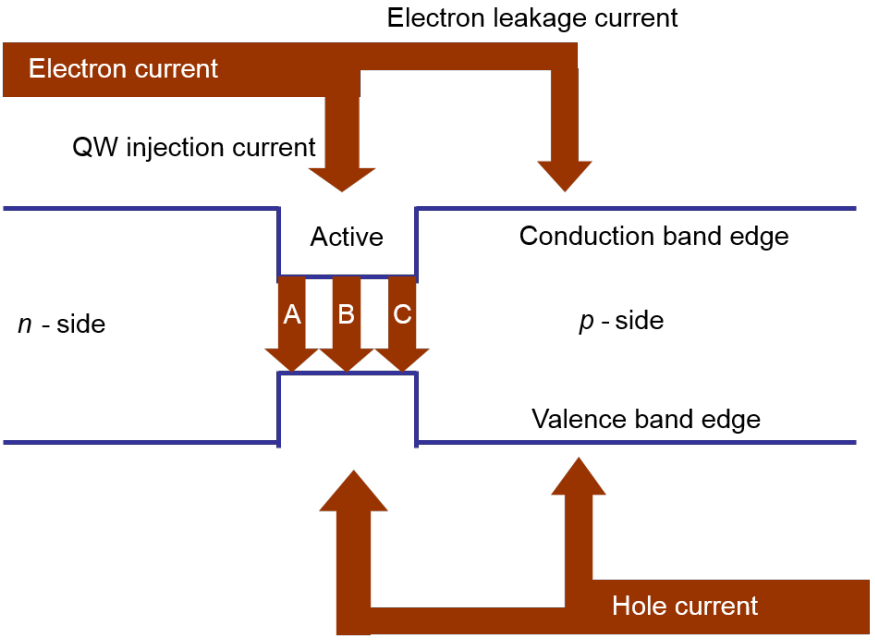

FIGURE 1.16: Schematic illustration of LED current components for efficiency droop analysis. A, B and C represent SRH recombination, spontaneous recombination and Auger recombination, respectively. Reproduced from [48].

where q is electron charge, V_{active} is the effective volume of active region, n is the carrier concentration in the QWs, and A, B and C are the coefficients of SRH recombination, radiative recombination and Auger recombination, respectively.

The electron leakage outside the QWs can be expressed by a phenomenological formula

$$I_{leakage} = aI_{QW}^{m}, \tag{1.15}$$

where a and m are fitted parameters.

Thus, combining the above equations together, η_{IQE} is expressed as

$$\eta_{IQE} = \frac{qV_{active}Bn^2}{I_{QW} + aI_{QW}^{m}} = \frac{\eta_{INJ} \cdot Bn^2}{An + Bn^2 + Cn^3}, \tag{1.16}$$

where the injection efficiency η_{INJ} represents the fraction of recombination carriers in the QWs

$$\eta_{INJ} = \frac{I_{QW}}{I} = \frac{I_{QW}}{I_{QW} + aI_{QW}^{m}}. \tag{1.17}$$

1.3.2.2 Defect-assisted recombination

The typical non-radiative recombination due to defects is described by the SRH model. At low current, other high-order non-radiative recombinations are relatively weak. Assuming there are no current leakage and Auger recombination, η_{IQE} is expressed as:

$$\eta_{IQE} = \frac{Bn^2}{An + Bn^2}. \tag{1.18}$$

In this case, SRH recombination influences the peak efficiency but will not cause efficiency droop [48]. LEDs with different dislocation densities [49] and different defect densities [50] have been used to confirm this phenomenon.

In another case, if the SRH carrier lifetime decreases with increasing current density, defects may contribute to efficiency droop. This mechanism is based on the non-uniform indium distribution and thereby the induced band gap inhomogeneity (potential fluctuation) inside InGaN QWs [51]. Indium-rich clusters are associated with lower bandgap, causing carrier localization. At low current, carriers are localized in indium-rich areas without being captured by defects. At higher current, indium-rich areas are filled up, and carriers spill over into areas with low indium concentration and then recombine with the defects. Also, the potential fluctuation is caused by other factors, such as QW width fluctuation as shown in figure 1.17 [52]. A density-activated defect recombination (DADR) model based on this idea has been proposed so as to explain the droop phenomenon [53]. The DADR model assumes a specific carrier density N_0 after which DADR sets in. The DADR current is expressed as $J_{DADR} = 0$ for $N < N_0$ and if $N > N_0$,

$$J_{DADR} = \frac{en_w}{\tau_{DADR}} \frac{(N - N_0)^2}{2N_0}, \tag{1.19}$$

where n_w is the number of wells, N is carrier density, and τ_{DADR} is the DADR recombination lifetime. τ_{DADR} ~3.8 ns has been obtained, much shorter than typical SRH recombination lifetime ~36 ns [48, 53]. In this case, DADR is possible to induce efficiency droop.

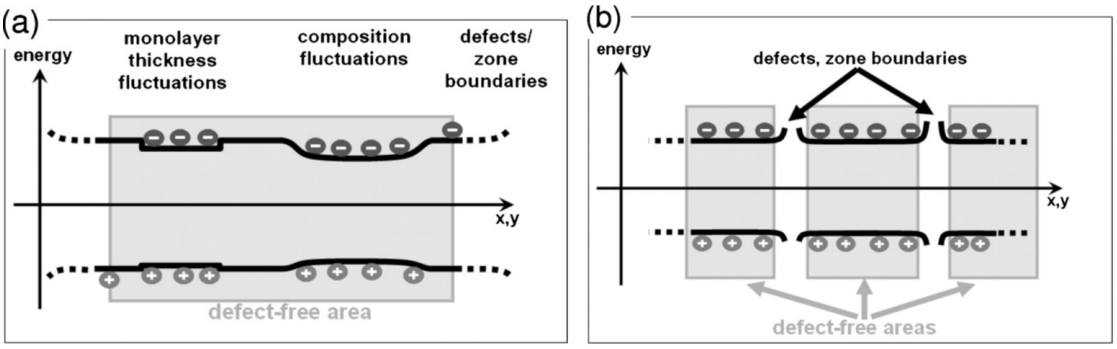

FIGURE 1.17: Illustration of potential fluctuation (a) due to local well width fluctuation and composition fluctuation or (b) due to local energy activated defect states. From [53].

1.3.2.3 Radiative recombination

It is reported that the radiative recombination is proportional to n^2 at low current. At high current, the radiative recombination approaches a more linear dependency on n due to the phase space filling effect [54]. As shown in figure 1.18 for 430 nm GaN-based LEDs, the experimental B coefficient decreases with n. Using $B = B_0/(1 + n/N^*)$ to fit the phase space filling effect, $B_0 = 7 \times 10^{-11}$ cm^{3}s^{-1} and $N^* = 5 \times 10^{18}$ cm^{-3} are obtained [55]. B coefficient does not cause efficiency droop, but the phase space filling effect lowers the barrier for non-radiative recombination to trigger the efficiency reduction [48].

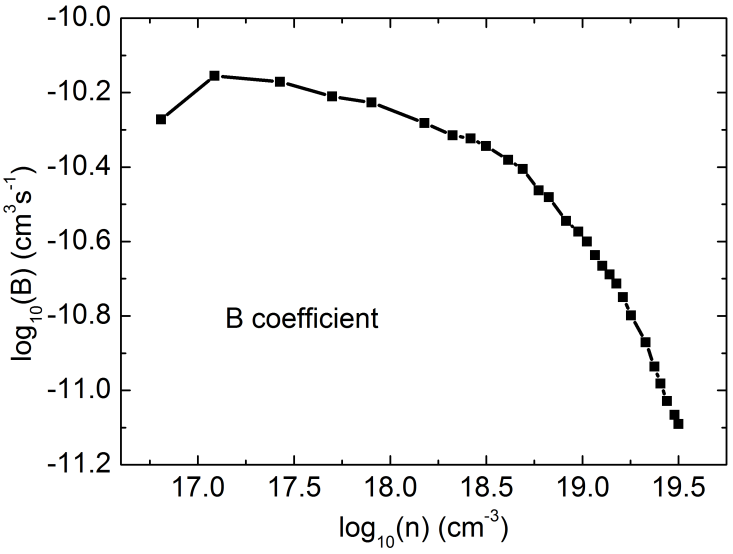

FIGURE 1.18: The experimental B coefficient as a function of n. Reproduced from data in [55].

1.3.2.4 Auger recombination

Auger recombination means that the non-radiative recombination processes transfer the excess carrier energy to other carriers that are excited to higher energy levels. The Auger recombination probability decreases significantly with increasing bandgap and thus it was previously considered negligible in wide-gap materials. For GaN material, the Auger recombination coefficient is expected to be $\sim 10^{-34}$ cm^6s^{-1} (band gap ~3.4 eV), however recent experimental and theoretical results confirm that the Auger recombination coefficient is much larger and that Auger recombination is one important reason for efficiency droop.

Generally, the Auger coefficient is calculated by neglecting electron leakage, and thus η_{IQE} can be expressed as:

$$\eta_{IQE} = \frac{Bn^2}{An + Bn^2 + Cn^3}. \tag{1.20}$$

Auger recombination as the dominant mechanism for efficiency droop was proposed by Shen et al. [56]. They used a photoluminescence (PL) technique to measure the Auger coefficient of quasi-bulk $In_xGa_{1-x}N(x \sim 9\% - 15\%)$ layers grown on GaN substrate. The measured Auger coefficient ranges from 1.4×10^{-30} to 2.0×10^{-30} cm^6s^{-1}. After that, a number of groups used different methods to extract the Auger coefficient [23, 55–62]. Based on these works, the Auger coefficient has been obtained for various materials, including InGaN layers and InGaN nanowires with emisson wavelength from violet to green on freestanding GaN, sapphire and Si substrates. These results are summarized in table 1.1 and the Auger coefficient ranges from 10^{-34} to 10^{-29} cm^6s^{-1} [23, 55–62]. Different assumptions, including the effective QW thickness, η_{IQE} determination method, carrier concentration n determination, phase space filling effect, etc., have been made for each of these methods which may be the reason for the large variation of obtained Auger coefficient. The theoretical value of the Auger coefficient was also calculated in the range from 10^{-34} to 10^{-30} cm^6s^{-1} [63–66] as shown in table 1.1. Recently, Iveland et al. reported the direct measurement of Auger electrons emitted from cesiated GaN-based LEDs under electrical injection by analysing the emitted conduction-band electrons [67]. A good linear correlation was achieved between the Auger electron current obtained by measuring the high-energy peak of the electron spectrum and the non-radiative current acquired by LED emission intensity. However, it is also argued that the observed

TABLE 1.1: Summary of measured$^{(a)}$ and theoretical$^{(b)}$ coefficients of SRH recombination, radiative recombination and Auger recombination.

Authors	Wavelength λ(nm)/InN(%)	A(s^{-1})	B(cm^3s^{-1})	C(cm^6s^{-1})
Shen et al.[56]$^{(a)}$	InN(9%-15%)	2.4-11.3×10^7	1.1-3.0×10^{-11}	1.4-2.0×10^{-30}
Zhang et al. [57]$^{(a)}$	λ(407 nm)	1×10^7	2×10^{-11}	1.5×10^{-30}
David et al.[55]$^{(a)}$	λ(430 nm)	2×10^7	7×10^{-11}	1×10^{-29}
Scheibenzuber et al.[58]$^{(a)}$	λ(415 nm)	(4.2±0.4)×10^7	(3±1)×10^{-12}	(4.5±0.9)×10^{-31}
Guo et al.[59]$^{(a)}$	λ(∼500 nm)			4.1×10^{-33}-6.1×10^{-32}
Nguyen et al.[60]$^{(a)}$	λ(∼550 nm)	5.5×10^7-4.6×10^8		∼10^{-34}
Galler et al.[23]$^{(a)}$	λ(428-457 nm)	∼10^7	1-2×10^{-11}	3-4×10^{-31}
Green et al.[61]$^{(a)}$	λ(450-520 nm)	0.8-3.2×10^8	0.4-15×10^{-12}	3-10×10^{-30}
Schiavon et al.[62]$^{(a)}$	λ(440-531 nm)	∼10^7	3×10^{-12}-2×10^{-11}	3-6×10^{-31}
Hader et al. [63]$^{(b)}$	InN(37%)		3.5×10^{-12}	3.5×10^{-34}
Delaney et al.[64]$^{(b)}$	InN(9%-15%)			1.4-2.0×10^{-30}
Kioupakis et al.[65]$^{(b)}$	InN(12%-29%)			1-3×10^{-31}
Vaxenburg et al.[66]$^{(b)}$	λ(445-472 nm)			10^{-31}-10^{-30}

high-energy electron peaks could correspond to electrons that gain kinetic energy in the strong near-surface electric field or the reabsorption of LED light by free charge carriers [68]. These researches on Auger recombination indicates that this process contributes significantly to efficiency droop.

1.3.2.5 Electron leakage

The electron leakage beyond the QW region is a well-known problem in GaN-based LEDs and an AlGaN electron blocker (EBL) layer between QWs and p-GaN is usually employed to alleviate electron leakage. Direct experimental observation of electron leakage was reported by measuring spontaneous emission from the p-side of LEDs [69]. An extra QW was inserted between the EBL and p-GaN, so the light emission from this QW indicated that some electrons leaked from the active region and recombined in this QW. Electron leakage was observed when increasing the LED current density to the intermediate range, at which efficiency droop occurred. Another experimental determination of electron leakage was directly observed by measuring the change in the forward current generated by a resonant excitation [70]. This work found that carrier leakage indeed played an important role in efficiency droop but could not single-handedly explain the efficiency droop.

Electron leakage may be induced by several issues: a poor hole injection efficiency, an ineffective EBL, an incomplete capture of electrons by the QWs and electron escape from the QWs [71]. First, although the EBL is intended to confine electrons to the active region, the valence band offset of AlGaN/GaN also results in a barrier for hole transport. Second, an EBL is often unable to completely block electron leakage. Figure 1.19(a) shows the calculated energy band diagram of a InGaN LED at a current of 350 mA. The spontaneous and piezoelectric polarizations strongly affect the band diagram, causing triangular barriers. As shown in figure 1.19(b), the electrons are attracted by the positive sheet charges near the EBL, indicating complete confinement of electrons into the active region may not be possible. Third, electrons and holes located preceding a QW may be transported across the QW or reflected from the QW, while only the carriers captured by the QW contribute to radiative recombination. In figure 1.19(c), electrons injected into the QW face large triangular barriers, resulting from the mismatch in polarization of GaN quantum barrier(QB) and InGaN QW.

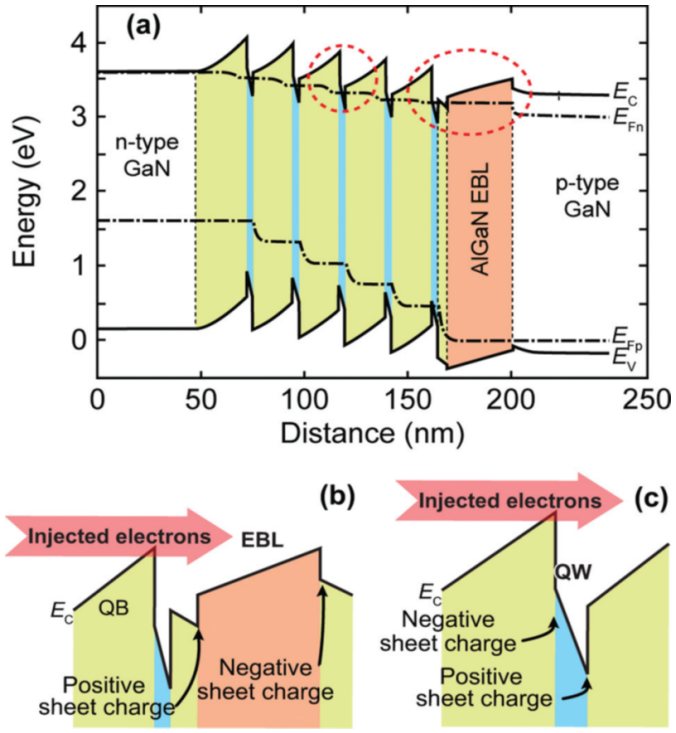

FIGURE 1.19: (a) Calculated energy band diagram of a InGaN LED with area 1×1 mm^2 at current 350 mA. Enlarged diagram (b) near the EBL and (c) near a QW. From [71].

1.3.2.6 Thermal droop problems

Besides the commonly called efficiency droop with increased current density (called J-droop), GaN-based LEDs also suffer from a strong efficiency decrease with increasing temperature, called T-droop [72]. Figure 1.20 shows that the η_{EQE} peak value decreases

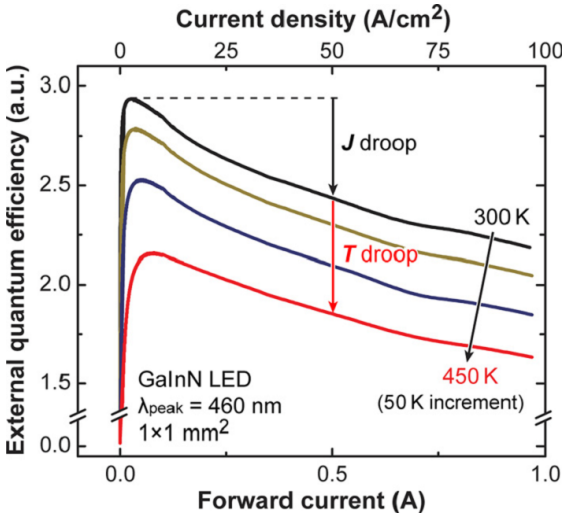

FIGURE 1.20: Measured η_{EQE} versus current of a typical 460 nm LED at various ambient temperatures. From [72].

about 30% from 300 K to 450 K, indicating that T-droop is more detrimental than J-droop. Regarding the applications of LEDs in a high-temperature environment, T-droop is an important issue to consider. It is found that SRH recombination increases with temperature and greatly reduces the LED efficiency at low current densities [72]. At high current densities, more current leakage with increasing temperature is suggested as one possible T-droop mechanism [73].

1.3.3 Remedies of efficiency droop

To reduce the efficiency droop, remedies have been proposed, including reducing QW carrier concentration, improving electron confinement, and enhancing hole injection [74].

Reducing QW carrier concentration at the same driving current can be achieved by methods including increasing the QW thickness, increasing the QW number, and improving current spreading, etc. A double-heterostructure LED with a 9-nm thick QW exhibits a significant reduced efficiency droop compared with a multiple QW (MQW) LED with 2.5-nm thick QW [75]. The optimized QW thickness depends on the material quality grown on substrates. For high In-content LEDs, the thick QW LEDs suffer from poor material quality and reduced efficiency, so increasing QW number is suggested to be a better solution [76]. Reduced efficiency droop have been demonstrated for a 9-QW LED compared with a 6-QW one with QW thickness 4 nm [77]. One later simulation result demonstrates that increasing QW number can improve lateral current spreading and reduce the electron leakage [78]. The lateral current spreading optimization benefits significantly on the efficiency droop improvement, through optimizing the LED contact [79] and designing LEDs with smaller sizes [30].

Many methods of enhancing electron confinement in the QWs have been employed to suppress the electron leakage. Instead of AlGaN, newly designed EBLs, such as $In_{0.18}Al_{0.82}N$ [80] or $In_{0.18}Al_{0.82}N$/GaN superlattices [81], can reduce the efficiency droop. Engineered QBs, including AlInGaN [82], $In_{0.1}Ga_{0.9}N$/GaN/$In_{0.1}Ga_{0.9}N$ multilayer [83], and graded InGaN with In mole fraction from 0.05 to 0 [84], are used to replace commonly used GaN QBs, so polarization charges in the MQW region are reduced to attenuate electron leakage. Other designs to suppress electron leakage include reversed polarization of QWs [85], and non-polar or semi-polar LED [86, 87].

Approaches to enhance hole injection into QWs have also been developed as follows. *P*-type doped QBs helped to move the efficiency peak up to 900 A/cm^2 [88]. In addition, a *p*-type hole reservoir layer of $In_{0.05}Ga_{0.95}N$ between the MQW and EBL was simulated predicting droop reduction [89].

1.4 Summary and thesis structure

In summary, this chapter has described the history of LED development, detailed the fabrication and applications of GaN-based broad-area LEDs and micro-LEDs, and reviewed the progress in efficiency droop research.

This thesis is organized as follows. After the introduction of chapter 1, the fabrication and characterization techniques will be described in chapter 2. Then, this work will analyse the size-dependent and temperature-dependent efficiency droop mechanisms of micro-LEDs in chapter 3 and 4, respectively. The related carrier recombination dynamics connect with the modulation bandwidth for VLC application [61], while the efficiency improvement at high current density also facilitates the application in micro-displays. Furthermore, in chapter 5, to optimize the device fabrication and to expand the applications of micro-LEDs, flexible micro-LEDs have been demonstrated for the applications in flexible micro-displays and VLC, as well as future applications in biomedicine due to their bio-compatibility. Also, in chapter 6, micro-LEDs on Si substrates have been fabricated for possible applications. Due to the low cost and scalability of the wafers grown on large area Si substrates, the cost of micro-LEDs may be significantly reduced. A summary and perspective will be given in chapter 7.

References

[1] S. Pimputkar, J. S. Speck, S. P. DenBaars, and S. Nakamura. Prospects for LED lighting. *Nature Photonics*, 3(4):180–182, 2009.

[2] E. F. Schubert and J. K. Kim. Solid-state light sources getting smart. *Science*, 308(5726): 1274–1278, 2005.

[3] M. R. Krames, O. B. Shchekin, R. Mueller-Mach, G. O. Mueller, L. Zhou, G. Harbers, and M. G. Craford. Status and future of high-power light-emitting diodes for solid-state lighting. *Journal of Display Technology*, 3(2):160–175, 2007.

[4] R. D. Dupuis and M. R. Krames. History, development, and applications of high-brightness visible light-emitting diodes. *Journal of Lightwave Technology*, 26(9):1154–1171, 2008.

[5] J. K. Kim and E. F. Schubert. Transcending the replacement paradigm of solid-state lighting. *Optics Express*, 16(26):21835–21842, 2008.

[6] S. Chhajed, Y. Xi, Y. L. Li, T. Gessmann, and E. F. Schubert. Influence of junction temperature on chromaticity and color-rendering properties of trichromatic white-light sources based on light-emitting diodes. *Journal of Applied Physics*, 97(5):054506, 2005.

[7] H. J. Round. A note on carborundum. *Electrical World*, 49:309, 1907.

[8] F. A. Ponce and D. P. Bour. Nitride-based semiconductors for blue and green light-emitting devices. *Nature*, 386(6623):351–359, 1997.

[9] W. O. Groves, A. H. Herzog, and M. G. Craford. The effect of nitrogen doping on $GaAs_{1-x}P_x$ electroluminescent diodes. *Applied Physics Letters*, 19(6):184–186, 1971.

[10] C. P. Kuo, R. M. Fletcher, T. D. Osentowski, M. C. Lardizabal, M. G. Craford, and V. M. Robbins. High performance AlGaInP visible light-emitting diodes. *Applied Physics Letters*, 57(27):2937–2939, 1990.

[11] Fr. Fichter. Über Aluminiumnitrid. *Zeitschrift für anorganische Chemie*, 54(1):322–327, 1907.

[12] H. P. Maruska and J. J. Tietjen. The preparation and properties of vapor-deposited single-crystalline GaN. *Applied Physics Letters*, 15(10):327–329, 1969.

[13] H. M. Manasevit and W. I. Simpson. The use of metal-organics in the preparation of semiconductor materials. *Journal of The Electrochemical Society*, 118(11):1864–1868, 1971.

[14] H. Amano, N. Sawaki, I. Akasaki, and Y. Toyoda. Metalorganic vapor phase epitaxial growth of a high quality GaN film using an AlN buffer layer. *Applied Physics Letters*, 48 (5):353–355, 1986.

[15] H. Amano, M. Kito, K. Hiramatsu, and I. Akasaki. P-type conduction in Mg-doped GaN treated with low-energy electron beam irradiation (LEEBI). *Japanese Journal of Applied Physics*, 28(12):L2112–L2114, 1989.

[16] S. Nakamura, T. Mukai, M. Senoh, and N. Iwasa. Thermal annealing effects on p-type Mg-doped GaN films. *Japanese Journal of Applied Physics*, 31(2B):L139–L142, 1992.

[17] T. Langer, A. Kruse, F. A. Ketzer, A. Schwiegel, L. Hoffmann, H. Jönen, H. Bremers, U. Rossow, and A. Hangleiter. Origin of the "green gap": increasing nonradiative recombination in indium-rich GaInN/GaN quantum well structures. *Physica Status Solidi (c)*, 8 (7-8):2170–2172, 2011.

[18] O. Ambacher. Growth and applications of group III-nitrides. *Journal of Physics D: Applied Physics*, 31(20):2653, 1998.

[19] S. Nakamura, T. Mukai, and M. Senoh. Candela-class high-brightness InGaN/AlGaN double-heterostructure blue-light-emitting diodes. *Applied Physics Letters*, 64(13):1687, 1994.

[20] S. D. Lester, F. A. Ponce, M. G. Craford, and D. A. Steigerwald. High dislocation densities in high efficiency GaN-based light-emitting diodes. *Applied Physics Letters*, 66(10):1249–1251, 1995.

[21] S. Chichibu, K. Wada, and S. Nakamura. Spatially resolved cathodoluminescence spectra of InGaN quantum wells. *Applied Physics Letters*, 71(16):2346–2348, 1997.

[22] Osram. Osram Opto unveils R&D results from GaN LEDs grown on silicon. `http://ledsmagazine.com/news/9/1/19`, 2012.

[23] B. Galler, P. Drechsel, R. Monnard, P. Rode, P. Stauss, S. Froehlich, W. Bergbauer, M. Binder, M. Sabathil, B. Hahn, and J. Wagner. Influence of indium content and temperature on Auger-like recombination in InGaN quantum wells grown on (111) silicon substrates. *Applied Physics Letters*, 101(13):131111, 2012.

[24] F. Jiang, C. Xiong, W. Fang, and L. Wang. Semiconductor light-emitting device with metal support substrate, January 29 2013. US Patent 8,361,880.

[25] E. F. Schubert. *Light emitting diodes*. Second edition, Cambridge University Press, 2006.

[26] Osram. Osram LED: longer lifetime at high temperatures. `http://www.osram.co.uk/osram_uk/news-and-knowledge/led-home/professional-knowledge/technologies/led-lamps/index.jsp`, 2013.

[27] Osram. `http://www.osram.com/`.

[28] Z. Gong, S. Jin, Y. Chen, J. McKendry, D. Massoubre, I. M. Watson, E. Gu, and M. D. Dawson. Size-dependent light output, spectral shift, and self-heating of 400 nm InGaN light-emitting diodes. *Journal of Applied Physics*, 107(1):013103, 2010.

[29] T. I. Kim, Y. H. Jung, J. Song, D. Kim, Y. Li, H. S. Kim, I. S. Song, J. J. Wierer, H. A. Pao, Y. Huang, and J. A. Rogers. High-efficiency, microscale GaN light-emitting diodes and their thermal properties on unusual substrates. *Small*, 8(11):1643–9, 2012.

[30] P. Tian, J. J. D. McKendry, Z. Gong, B. Guilhabert, I. M. Watson, E. Gu, Z. Chen, G. Zhang, and M. D. Dawson. Size-dependent efficiency and efficiency droop of blue InGaN micro-light emitting diodes. *Applied Physics Letters*, 101(23):231110, 2012.

[31] J. Day, J. Li, D. Y. C. Lie, C. Bradford, J. Y. Lin, and H. X. Jiang. III-Nitride full-scale high-resolution microdisplays. *Applied Physics Letters*, 99(3):031116, 2011.

[32] Z. Y. Fan, J. Y. Lin, and H. X. Jiang. III-nitride micro-emitter arrays: development and applications. *Journal of Physics D: Applied Physics*, 41(9):094001, 2008.

[33] J. J. D. McKendry, D. Massoubre, S. Zhang, B. R. Rae, R. P. Green, E. Gu, R. K. Henderson, A. E. Kelly, and M. D. Dawson. Visible-light communications using a CMOS-controlled micro-light-emitting-diode array. *Journal of Lightwave Technology*, 30(1):61–67, 2012.

[34] J. J. D. McKendry, R. P. Green, A. E. Kelly, Z. Gong, B. Guilhabert, D. Massoubre, E. Gu, and M. D. Dawson. High-speed visible light communications using individual pixels in a micro light-emitting diode array. *IEEE Photonics Technology Letters*, 22(18):1346–1348, 2010.

[35] B. Guilhabert, D. Massoubre, E. Richardson, J. J. D. McKendry, R. K. Henderson, I. M. Watson, E. Gu, and M. D. Dawson. Sub-micron lithography using InGaN micro-LEDs: mask-free fabrication of LED arrays. *IEEE Photonics Technology Letters*, 24(24):2221–2224, 2012.

[36] V. Poher, N. Grossman, G. T. Kennedy, K. Nikolic, H. X. Zhang, Z. Gong, E. M. Drakakis, E. Gu, M. D. Dawson, P. M. W. French, P. Degenaar, and M. A. A. Neil. Micro-LED arrays: a tool for two-dimensional neuron stimulation. *Journal of Physics D: Applied Physics*, 41 (9):094014, 2008.

[37] M. Scanziani and M. Häusser. Electrophysiology in the age of light. *Nature*, 461(7266): 930–939, 2009.

[38] A. Zarowna-Dabrowska, S. L. Neale, D. Massoubre, J. McKendry, B. R. Rae, R. K. Henderson, M. J. Rose, H. Yin, J. M Cooper, E. Gu, and M. D. Dawson. Miniaturized optoelectronic tweezers controlled by GaN micro-pixel light emitting diode arrays. *Optics Express*, 19(3):2720–2728, 2011.

[39] M. Akhter, P. Maaskant, B. Roycroft, B. Corbett, P. de Mierry, B. Beaumont, and K. Panzer. 200 Mbit/s data transmission through 100 m of plastic optical fibre with nitride LEDs. *Electronics Letters*, 38(23):1457–1458, 2002.

[40] J. Vučić, C. Kottke, S. Nerreter, K.-D. Langer, and J. W. Walewski. 513 Mbit/s visible light communications link based on DMT-modulation of a white LED. *Journal of Lightwave Technology*, 28(24):3512–3518, 2010.

[41] C.-L. Liao, Y.-F. Chang, C.-L. Ho, and M.-C. Wu. High-speed GaN-based blue light-emitting diodes with Gallium-doped ZnO current spreading layer. *IEEE Electron Device Letters*, 34(5):611 – 613, 2013.

[42] L. Hirsch and A.-S. Barriere. Electrical characterization of InGaN/GaN light emitting diodes grown by molecular beam epitaxy. *Journal of Applied Physics*, 94(8):5014–5020, 2003.

[43] J. W. P. Hsu, M. J. Manfra, D. V. Lang, S. Richter, S. N. G. Chu, A. M. Sergent, R. N. Kleiman, L. N. Pfeiffer, and R. J. Molnar. Inhomogeneous spatial distribution of reverse bias leakage in GaN Schottky diodes. *Applied Physics Letters*, 78(12):1685–1687, 2001.

[44] X. Guo, Y.-L. Li, and E. F. Schubert. Efficiency of GaN/InGaN light-emitting diodes with interdigitated mesa geometry. *Applied Physics Letters*, 79(13):1936–1938, 2001.

[45] W. Schockley. The theory of pn junctions in semiconductors and pn-junction transistors. *Bell System Technical Journal*, 28(3):435–489, 1949.

[46] C.-T. Sah, R. N. Noyce, and W. Shockley. Carrier generation and recombination in pn junctions and pn junction characteristics. *Proceedings of the IRE*, 45(9):1228–1243, 1957.

[47] A. David, M. J. Grundmann, J. F. Kaeding, N. F. Gardner, T. G. Mihopoulos, and M. R. Krames. Carrier distribution in (0001) InGaN/ GaN multiple quantum well light-emitting diodes. *Applied Physics Letters*, 92(5):053502, 2008.

[48] J. Piprek. Efficiency droop in nitride-based light-emitting diodes. *Physica Status Solidi (a)*, 207(10):2217–2225, 2010.

[49] M. F. Schubert, S. Chhajed, J. K. Kim, E. F. Schubert, D. D. Koleske, M. H. Crawford, S. R. Lee, A. J. Fischer, G. Thaler, and M. A. Banas. Effect of dislocation density on efficiency droop in GaInN/ GaN light-emitting diodes. *Applied Physics Letters*, 91(23):231114, 2007.

[50] X. Shao, H. Lu, D. Chen, Z. Xie, R. Zhang, and Y. Zheng. Efficiency droop behavior of direct current aged GaN-based blue light-emitting diodes. *Applied Physics Letters*, 95(16): 163504, 2009.

[51] S. F. Chichibu, A. Uedono, T. Onuma, B. A. Haskell, A. Chakraborty, T. Koyama, P. T. Fini, S. Keller, S. P. Denbaars, J. S. Speck, U. K. Mishra, S. Nakamura, S. Yamaguchi, S. Kamiyama, H. Amano, I. Akasaki, J. Han, and T. Sota. Origin of defect-insensitive emission probability in In-containing (Al, In, Ga) N alloy semiconductors. *Nature Materials*, 5(10):810–816, 2006.

[52] S. F. Chichibu, A. C. Abare, M. S. Minsky, S. Keller, S. B. Fleischer, J. E. Bowers, E. Hu, U. K. Mishra, L. A. Coldren, S. P. DenBaars, and T. Sota. Effective band gap inhomogeneity and piezoelectric field in InGaN/GaN multiquantum well structures. *Applied Physics Letters*, 73(14):2006–2008, 1998.

[53] J. Hader, J. V. Moloney, and S. W. Koch. Density-activated defect recombination as a possible explanation for the efficiency droop in GaN-based diodes. *Applied Physics Letters*, 96(22):221106, 2010.

[54] J. Hader, J. V. Moloney, and S. W. Koch. Supression of carrier recombination in semiconductor lasers by phase-space filling. *Applied Physics Letters*, 87(20):201112, 2005.

[55] A. David and M. J. Grundmann. Droop in InGaN light-emitting diodes: a differential carrier lifetime analysis. *Applied Physics Letters*, 96(10):103504, 2010.

[56] Y. C. Shen, G. O. Mueller, S. Watanabe, N. F. Gardner, A. Munkholm, and M. R. Krames. Auger recombination in InGaN measured by photoluminescence. *Applied Physics Letters*, 91(14):141101, 2007.

[57] M. Zhang, P. Bhattacharya, J. Singh, and J. Hinckley. Direct measurement of Auger recombination in InGaN/GaN quantum wells and its impact on the efficiency of InGaN/GaN multiple quantum well light emitting diodes. *Applied Physics Letters*, 95(20):201108, 2009.

[58] W. G. Scheibenzuber, U. T. Schwarz, L. Sulmoni, J. Dorsaz, J.-F. Carlin, and N. Grandjean. Recombination coefficients of GaN-based laser diodes. *Journal of Applied Physics*, 109(9): 093106, 2011.

[59] W. Guo, M. Zhang, P. Bhattacharya, and J. Heo. Auger recombination in III-nitride nanowires and its effect on nanowire light-emitting diode characteristics. *Nano Letters*, 11(4):1434–1438, 2011.

[60] H. P. T. Nguyen, M. Djavid, K. Cui, and Z. Mi. Temperature-dependent nonradiative recombination processes in GaN-based nanowire white-light-emitting diodes on silicon. *Nanotechnology*, 23(19):194012, 2012.

[61] R. P. Green, J. J. D. McKendry, D. Massoubre, E. Gu, M. D. Dawson, and A. E. Kelly. Modulation bandwidth studies of recombination processes in blue and green InGaN quantum well micro-light-emitting diodes. *Applied Physics Letters*, 102(9):091103, 2013.

[62] D. Schiavon, M. Binder, M. Peter, B. Galler, P. Drechsel, and F. Scholz. Wavelength-dependent determination of the recombination rate coefficients in single-quantum-well GaInN/GaN light emitting diodes. *Physica Status Solidi (b)*, 250(2):283–290, 2012.

[63] J. Hader, J. V. Moloney, B. Pasenow, S. W. Koch, M. Sabathil, N. Linder, and S. Lutgen. On the importance of radiative and Auger losses in GaN-based quantum wells. *Applied Physics Letters*, 92(26):261103, 2008.

[64] K. T. Delaney, P. Rinke, and C. G. Van de Walle. Auger recombination rates in nitrides from first principles. *Applied Physics Letters*, 94(19):191109, 2009.

[65] E. Kioupakis, P. Rinke, K. T. Delaney, and C. G. Van de Walle. Indirect Auger recombination as a cause of efficiency droop in nitride light-emitting diodes. *Applied Physics Letters*, 98(16):161107, 2011.

[66] R. Vaxenburg, E. Lifshitz, and Al. L. Efros. Suppression of Auger-stimulated efficiency droop in nitride-based light emitting diodes. *Applied Physics Letters*, 102(3):031120, 2013.

[67] J. Iveland, L. Martinelli, J. Peretti, J. S. Speck, and C. Weisbuch. Direct measurement of Auger electrons emitted from a semiconductor light-emitting diode under electrical injection: identification of the dominant mechanism for efficiency droop. *Physical Review Letters*, 110 (17):177406, 2013.

[68] A. G. Smart. New clues to LEDs' efficiency droop. *Physics Today*, 66(7):12–14, 2013.

[69] K. J. Vampola, M. Iza, S. Keller, S. P. DenBaars, and S. Nakamura. Measurement of electron overflow in 450 nm InGaN light-emitting diode structures. *Applied Physics Letters*, 94(6):061116, 2009.

[70] B.-J. Ahn, T.-S. Kim, Y. Dong, M.-T. Hong, J.-H. Song, J.-H. Song, H.-K. Yuh, S.-C. Choi, D.-K. Bae, and Y. Moon. Experimental determination of current spill-over and its effect

on the efficiency droop in InGaN/GaN blue-light-emitting-diodes. *Applied Physics Letters*, 100(3):031905, 2012.

[71] J. Cho, E. F. Schubert, and J. K. Kim. Efficiency droop in light-emitting diodes: challenges and countermeasures. *Laser & Photonics Reviews*, 7(3):408–421, 2013.

[72] D. S. Meyaard, Q. Shan, J. Cho, E. F. Schubert, S.-H. Han, M.-H. Kim, C. Sone, S. J. Oh, and J. K. Kim. Temperature dependent efficiency droop in GaInN light-emitting diodes with different current densities. *Applied Physics Letters*, 100(8):081106, 2012.

[73] D. S. Meyaard, Q. Shan, Q. Dai, J. Cho, E. F. Schubert, M.-H. Kim, and C. Sone. On the temperature dependence of electron leakage from the active region of GaInN/GaN light-emitting diodes. *Applied Physics Letters*, 99(4):041112, 2011.

[74] G. Verzellesi, D. Saguatti, M. Meneghini, F. Bertazzi, M. Goano, G. Meneghesso, and E. Zanoni. Efficiency droop in InGaN/GaN blue light-emitting diodes: physical mechanisms and remedies. *Journal of Applied Physics*, 114(7):071101, 2013.

[75] N. F. Gardner, G. O. Müller, Y. C. Shen, G. Chen, S. Watanabe, W. Götz, and M. R. Krames. Blue-emitting InGaN–GaN double-heterostructure light-emitting diodes reaching maximum quantum efficiency above 200A/cm^2. *Applied Physics Letters*, 91(24):243506, 2007.

[76] A. Laubsch, W. Bergbauer, M. Sabathil, Ma. Strassburg, H. Lugauer, M. Peter, T. Meyer, G. Brüderl, J. Wagner, N. Linder, K. Streubel, and B. Hahn. Luminescence properties of thick InGaN quantum-wells. *Physica Status Solidi (c)*, 6(S2):S885–S888, 2009.

[77] S. Tanaka, Y. Zhao, I. Koslow, C.-C. Pan, H.-T. Chen, J. Sonoda, S. P. DenBaars, and S. Nakamura. Droop improvement in high current range on PSS-LEDs. *Electronics Letters*, 47(5):335–336, 2011.

[78] C. S. Xia, Z. M. S. Li, Z. Q. Li, Y. Sheng, Z. H. Zhang, W. Lu, and L. W. Cheng. Optimal number of quantum wells for blue InGaN/GaN light-emitting diodes. *Applied Physics Letters*, 100(26):263504, 2012.

[79] C.-K. Li and Y.-R. Wu. Study on the current spreading effect and light extraction enhancement of vertical GaN/InGaN LEDs. *IEEE Transactions on Electron Devices*, 59(2): 400–407, 2012.

[80] S. Choi, H. J. Kim, S.-S. Kim, J. Liu, J. Kim, J.-H. Ryou, R. D. Dupuis, A. M. Fischer, and F. A. Ponce. Improvement of peak quantum efficiency and efficiency droop in III-nitride visible light-emitting diodes with an InAlN electron-blocking layer. *Applied Physics Letters*, 96(22):221105, 2010.

[81] Y.-Y. Zhang, X.-L. Zhu, Y.-A. Yin, and J. Ma. Performance enhancement of near-UV light-emitting diodes with an InAlN/GaN superlattice electron-blocking layer. *IEEE Electron Device Letters*, 33(7):994–996, 2012.

[82] M. F. Schubert, J. Xu, J. K. Kim, E. F. Schubert, M. H. Kim, S. Yoon, S. M. Lee, C. Sone, T. Sakong, and Y. Park. Polarization-matched GaInN/ AlGaInN multi-quantum-well light-emitting diodes with reduced efficiency droop. *Applied Physics Letters*, 93(4):041102, 2008.

[83] H. J. Chung, R. J. Choi, M. H. Kim, J. W. Han, Y. M. Park, Y. S. Kim, H. S. Paek, C. S. Sone, Y. J. Park, J. K. Kim, and E. F. Schubert. Improved performance of GaN-based blue light emitting diodes with InGaN/GaN multilayer barriers. *Applied Physics Letters*, 95(24): 241109, 2009.

[84] C. H. Wang, S. P. Chang, P. H. Ku, J. C. Li, Y. P. Lan, C. C. Lin, H. C. Yang, H. C. Kuo, T. C. Lu, S. C. Wang, and C. Y. Chang. Hole transport improvement in InGaN/GaN light-emitting diodes by graded-composition multiple quantum barriers. *Applied Physics Letters*, 99(17):171106, 2011.

[85] F. Akyol, D. N. Nath, S. Krishnamoorthy, P. S. Park, and S. Rajan. Suppression of electron overflow and efficiency droop in N-polar GaN green light emitting diodes. *Applied Physics Letters*, 100(11):111118, 2012.

[86] S.-C. Ling, T.-C. Lu, S.-P. Chang, J.-R. Chen, H.-C. Kuo, and S.-C. Wang. Low efficiency droop in blue-green m-plane InGaN/GaN light emitting diodes. *Applied Physics Letters*, 96 (23):231101, 2010.

[87] Y. Zhao, S. Tanaka, C.-C. Pan, K. Fujito, D. Feezell, J. S. Speck, S. P. DenBaars, and S. Nakamura. High-power blue-violet semipolar (2021) InGaN/GaN light-emitting diodes with low efficiency droop at 200 A/cm^2. *Applied Physics Express*, 4(8):082104, 2011.

[88] J. Xie, X. Ni, Q. Fan, R. Shimada, Ü. Özgür, and H. Morkoç. On the efficiency droop in InGaN multiple quantum well blue light emitting diodes and its reduction with p-doped quantum well barriers. *Applied Physics Letters*, 93(12):121107, 2008.

[89] T. Lu, S. Li, C. Liu, K. Zhang, Y. Xu, J. Tong, L. Wu, H. Wang, X. Yang, Y. Yin, G. Xiao, and Y. Zhou. Advantages of GaN based light-emitting diodes with a p-InGaN hole reservoir layer. *Applied Physics Letters*, 100(14):141106, 2012.

Chapter 2

Fabrication and characterization techniques of micro-LEDs

In this chapter, the main techniques for LED/micro-LED fabrication and characterization will be described. First, the fabrication techniques are introduced. The typical micro-LED fabrication processes in the clean room include pattern definition by photolithography, pattern etching by dry and wet etching, current spreading layer deposition by electron beam evaporation (e-beam) followed by rapid thermal annealing (RTA), SiO_2 isolation layer deposition by plasma enhanced chemical vapour deposition (PECVD), and p-pad and n-pad deposition by sputtering. To remove the sapphire substrates for GaN-based LEDs, bonding and laser lift off (LLO) techniques are commonly utilized. Then, two typical characterization techniques are briefly discussed. To characterize the luminescence properties of an LED structure, photoluminescence (PL) is a convenient technique without needing to fabricate a completed LED device. Finally, the modulation characteristics and eye diagrams of the fabricated LEDs have also been measured which determine their optical data communication speed for VLC application. The fabrication techniques of micro-LEDs and broad-area LEDs are largely compatible in this work.

2.1 LED fabrication techniques

This section mainly discusses the LED fabrication techniques, including the clean room, photolithography for pattern definition, dry and wet etching, SiO_2 and metal depositions,

RTA, and sapphire lift off. The processing principles and related equipment are also introduced.

2.1.1 The clean room

A clean processing room is required for LED fabrication, especially for photolithography. The class of a clean room is defined by the maximum allowable number of particles 0.5 μm and larger, per cubic foot [1]. The dust particles in the air can settle on the LED wafers and photomasks, which may induce unexpected device defects or failure. Thus, the total number of dust particles per unit volume in a clean room must be tightly controlled along with the temperature and humidity. Figure 2.1 shows the clean room, illuminated with yellow light, for LED fabrication in this work. The class of this clean room is 10000 for most areas, and the class is 1000 around the operation benches and photolithography equipment. The yellow lighting is critical for photolithography, in order to prevent unwanted exposure of photoresist from short-wavelength light. The operation benches are for photoresist processing, wet etching, sample baking, and sample cleaning, etc.

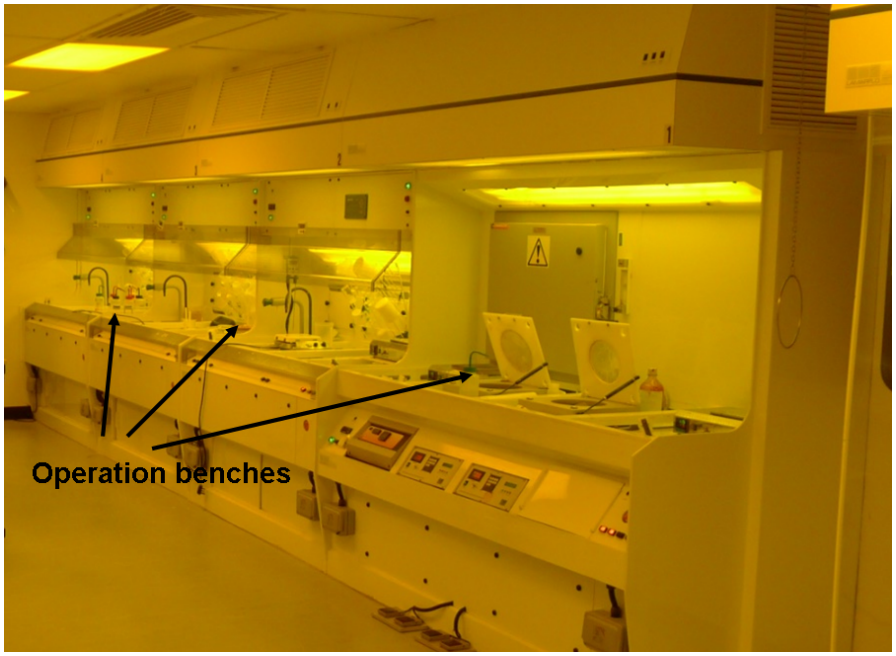

FIGURE 2.1: Photograph of the clean room with yellow lighting.

2.1.2 Photolithography

Photolithography is widely used in the modern semiconductor industry to develop patterns on semiconductor wafers. The photolithography performance can be determined by three parameters: resolution, registration, and throughput [1]. Resolution is the minimum feature size that can be transferred onto a wafer. Registration is a measure of the alignment accuracy. Throughput is the number of wafers that can be produced per hour.

Mask aligner

In this work, the photolithography has been undertaken on a Karl Suss MA6 Mask Aligner as shown in figure 2.2. The main parts of the mask aligner are a lamp housing, an alignment stage and a microscope. The high pressure mercury arc lamp with its electrical circuit is the exposure light source in the lamp housing. The lamp housing model for the MA6 mask aligner is UV400, with the high pressure arc lamp emitting light at wavelengths between 350 nm and 450 nm. Before the exposure process, the alignment between the photomask and the sample is achieved by using the adjustment screws and the microscope. Using a designed photomask (chrome pattern on glass), the photomask pattern is replicated into the photoresist by light exposure process. The positive photoresist will produce a replica of the photomask, while the negative photoresist will produce

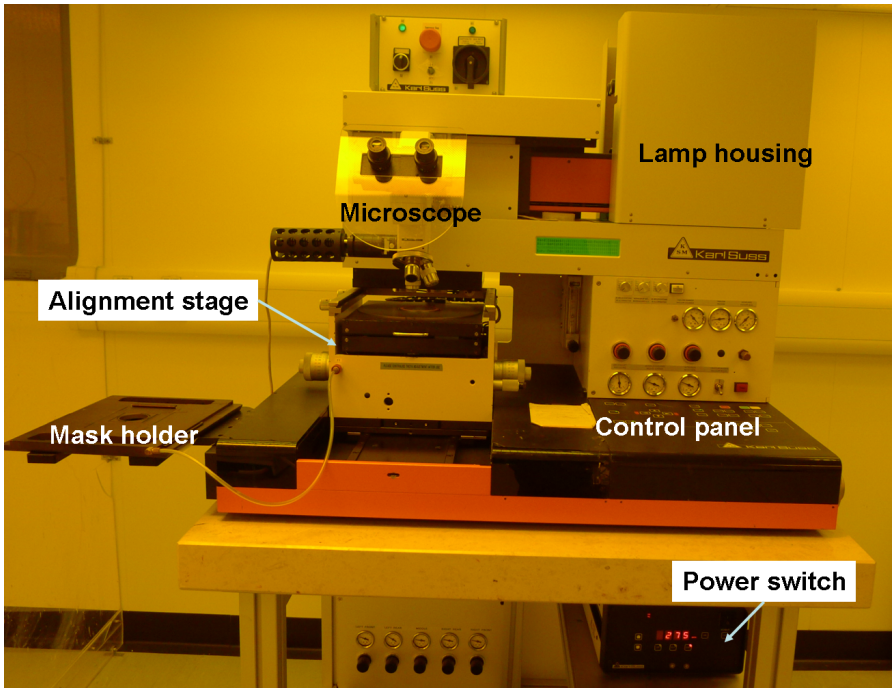

FIGURE 2.2: Photograph of the Karl Suss MA6 Mask Aligner.

the complementary pattern. Through the developing process the undesired photoresist material will be removed and the corresponding pattern will be obtained.

Photoresists

Photoresists are radiation-sensitive compounds and include positive and negative photoresists. The positive photoresists used in this work are S1805, S1818, and SPR220-4.5 from the Shipley Company, whose absorption spectrum matches the emission spectrum of the high pressure arc lamp of the aligner. Using a standard spin coating process (400 rpm for 60 seconds), S1805 has a thickness of 500 nm and as such is commonly used to define high-resolution features. Following the same spin coating processes, the S1818 has a thickness 1.8 μm and such a thick photoresist pattern can be used as an etching mask. The 4.5 μm thick photoresist layer obtained from SPR220-4.5 is suitable for a metal lift-off process. The typical processing steps for creating patterns on these positive photoresist are sample pre-bake, photoresist spin coat, photoresist post-bake, exposure, development, rinse and dry. The thickness of the coated photoresist can be adjusted by the spin coating speed and time; the bake, exposure and development times are determined by the photoresist type and thickness.

A typical negative photoresist used in this work is SU8 2002, mainly used here as a flexible isolation layer. The processing steps of SU8 2002 are similar to those of the positive photoresist, however for applications where such photoresist is to be left as part of the final device, a hard bake should be incorporated into the processes. To keep stable properties of SU8 during applications, the hard bake temperature should be higher than

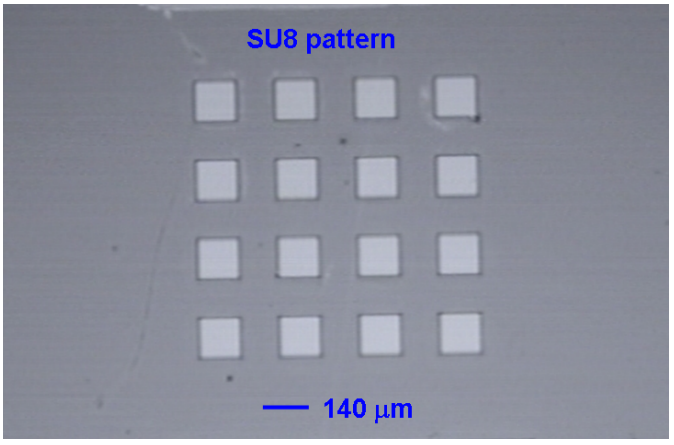

FIGURE 2.3: Microscopic image of a typical SU8 pattern created on a Si substrate.

the device application temperature, usually in the range from 150°C to 250°C. A typical SU8 pattern on a Si substrate is shown in figure 2.3.

2.1.3 Etching for pattern transfer

In the pattern transfer process, a photoresist pattern defined by photolithography serves as a mask for etching of its underlying layers. For most amorphous or polycrystalline materials, the etching is generally isotropic in a wet chemical etchant. As illustrated in figure 2.4, if h_f is the thickness of the etched layers and l is the lateral etched distance underneath the photoresist mask, the degree of anisotropy A_f is defined by $A_f = 1 - l/h_f$ [1]. The major disadvantage of wet chemical etching for pattern transfer is the reduced resolution due to the undercutting of layers underneath the mask, e.g. $A_f = 0$. Regarding micro-LED fabrication, the patterned SiO_2 isolation layer for p-pad and n-pad is usually defined by wet chemical etching. A longer etching process may cause excessive undercutting of the SiO_2 and introduce a current leakage path for micro-LED devices. To achieve a high-resolution transferred pattern, i.e. $A_f \approx 1$, dry etching methods have been developed. The wet and dry etching processes are discussed as follows.

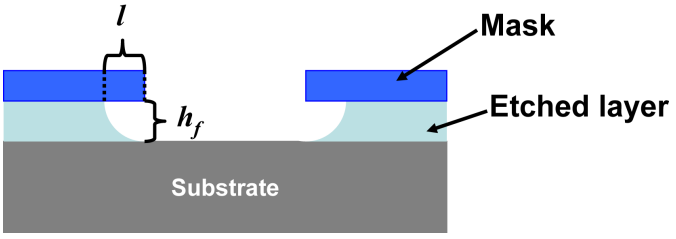

FIGURE 2.4: Schematic illustration of the anisotropy of etching.

Wet chemical etching

For wet etching, wafer cleanness, agitation and the temperature of the etchant solution, and the adhesion of the photoresist to the wafer will influence the etch rate and uniformity. The semiconductor wafers need to be chemically cleaned to remove contaminations that result from handling and storing, prior to photoresist spin coating. A hard baking process for the photoresist pattern is necessary to increase the adhesion of photoresist to the wafer. Then, SiO_2 wet etching is undertaken in a dilute solution of HF with the addition of NH_4F, the so-named buffered-oxide-etch (BOE). NH_4F is added to maintain HF concentration and to control pH (to minimize photoresist attack). The chemical

reaction of SiO_2 etching is [1]

$$SiO_2 + 6HF \rightarrow H_2SiF_6 + 2H_2O. \tag{2.1}$$

Wet chemical etching has been extensively used for LED processing. As mentioned, in our work SiO_2 is used as the isolation layer for the p-pad and n-pad in micro-LEDs. In this case, achieving a well-defined SiO_2 pattern is essential to the micro-LED performance.

Dry etching

Plasma-assisted dry etching tools mainly include reactive ion etching (RIE) and inductively coupled plasma etching (ICP), using atoms, radicals and ions from inert molecular gas [2]. Plasma etching proceeds in five steps: the etchant species are generated in the plasma; the reactant is adsorbed on the sample surface; a chemical reaction and physical effect such as ion bombardment takes place to form volatile compounds; the compounds are desorbed from the surface, diffused into the bulk gas, and pumped out by the vacuum system [1].

The dry etching tools can be equipped with a monitor, e.g. laser interferometry, to continuously monitor etching rates. During etching, the intensity of laser light reflected off a thin film surface oscillates, because of the phase interference between the light reflected from the outer and inner interfaces of the etching layer. The period of the oscillation is related to the change of the film thickness by $\delta d = \lambda/2n$, where δd is the change of film thickness for one period, λ is the wavelength of the laser, and n is the refractive index of the etching layer [1].

In an RIE machine with parallel-plate diode configuration, a radio-frequency (RF) capacitive-coupled bottom electrode holds the wafer. The large grounded area and the low operating pressure cause the wafers to be etched by a heavy bombardment of energetic ions from the plasma [1]. Shown in figure 2.5(a) is the Oxford PlasmaLab 80+ RIE system used in this work. Figure 2.5(b) shows the schematic diagram of the RIE chamber. In this work, the RIE dry etching of SiO_2 can define a SiO_2 pattern with anisotropy $A_f \approx 1$.

In comparison, the ICP system has a high-density plasma source (10^{11}-10^{12} cm^{-3}) and low processing pressure ($<$ 20 mTorr) [1]. Other advantages of ICP include the wafer

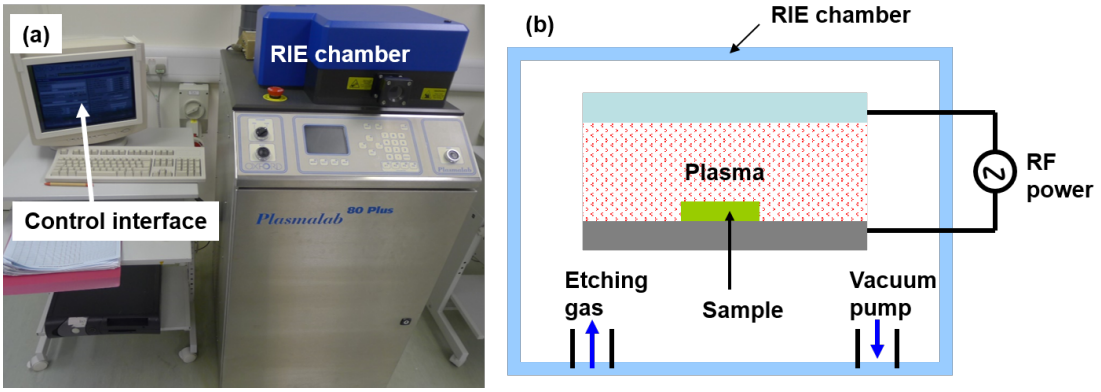

FIGURE 2.5: (a) Photograph of the Oxford PlasmaLab 80+ RIE system. (b) Schematic diagram of the etching process in the RIE chamber.

platen being powered independently of the source, higher etching rates, and high controllable etching selectivity. our STS ICP system with an etching rate monitor and the schematic diagram of the ICP chamber are shown in figure 2.6(a) and (b), respectively. In this work, the ICP system is mainly used to etch GaN mesas. With a charge-coupled device (CCD) camera and an etching rate monitor, the material etching rate can be continuously monitored.

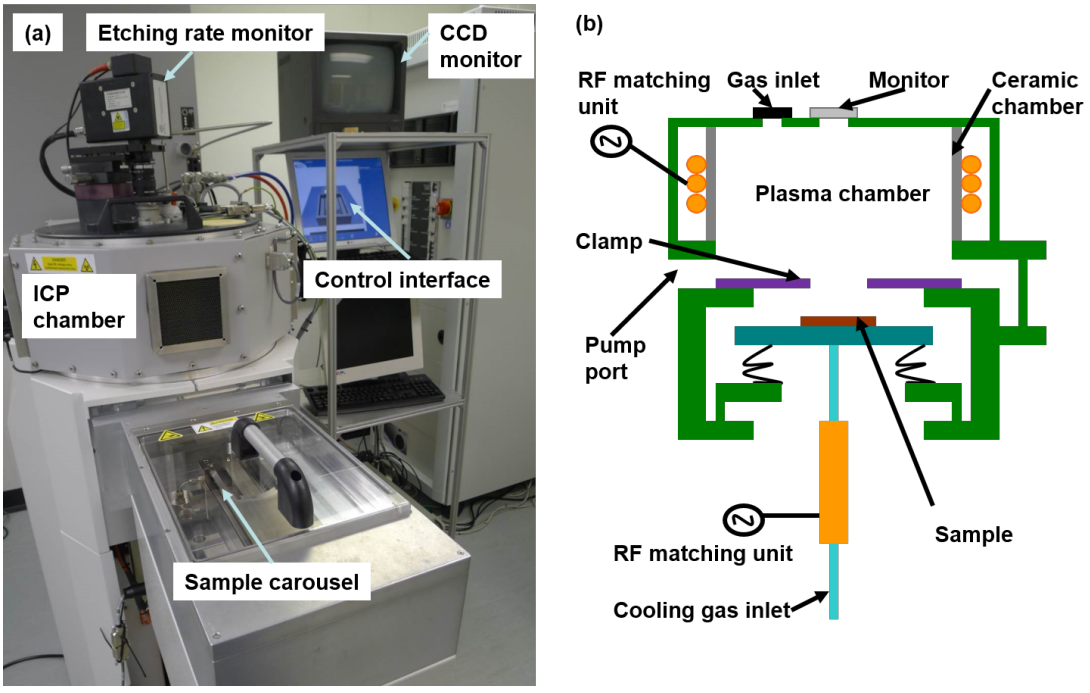

FIGURE 2.6: (a) Photograph of the ICP system from Surface Technology Systems. (b) Schematic diagram of the ICP chamber.

To fabricate a high-quality micro-LED device, dry etching and wet etching methods usually need be combined together, to effectively use the advantages and to avoid the

drawbacks of each technique. For example, to etch SiO_2 pattern on micro-LED devices, pure dry etching may cause damage to the surface of LED layers and pure wet etching will cause large undercutting. An effective method for etching SiO_2 pattern is using dry etching at the beginning and wet etching later to achieve an etched structure with a large degree of anisotropy and without damaging the semiconductor surface.

2.1.4 Pattern transfer

As an example of pattern transfer, figure 2.7 illustrates the processing steps to transfer a pattern from a photomask to a Si wafer with SiO_2 on its surface [1]. After cleaning

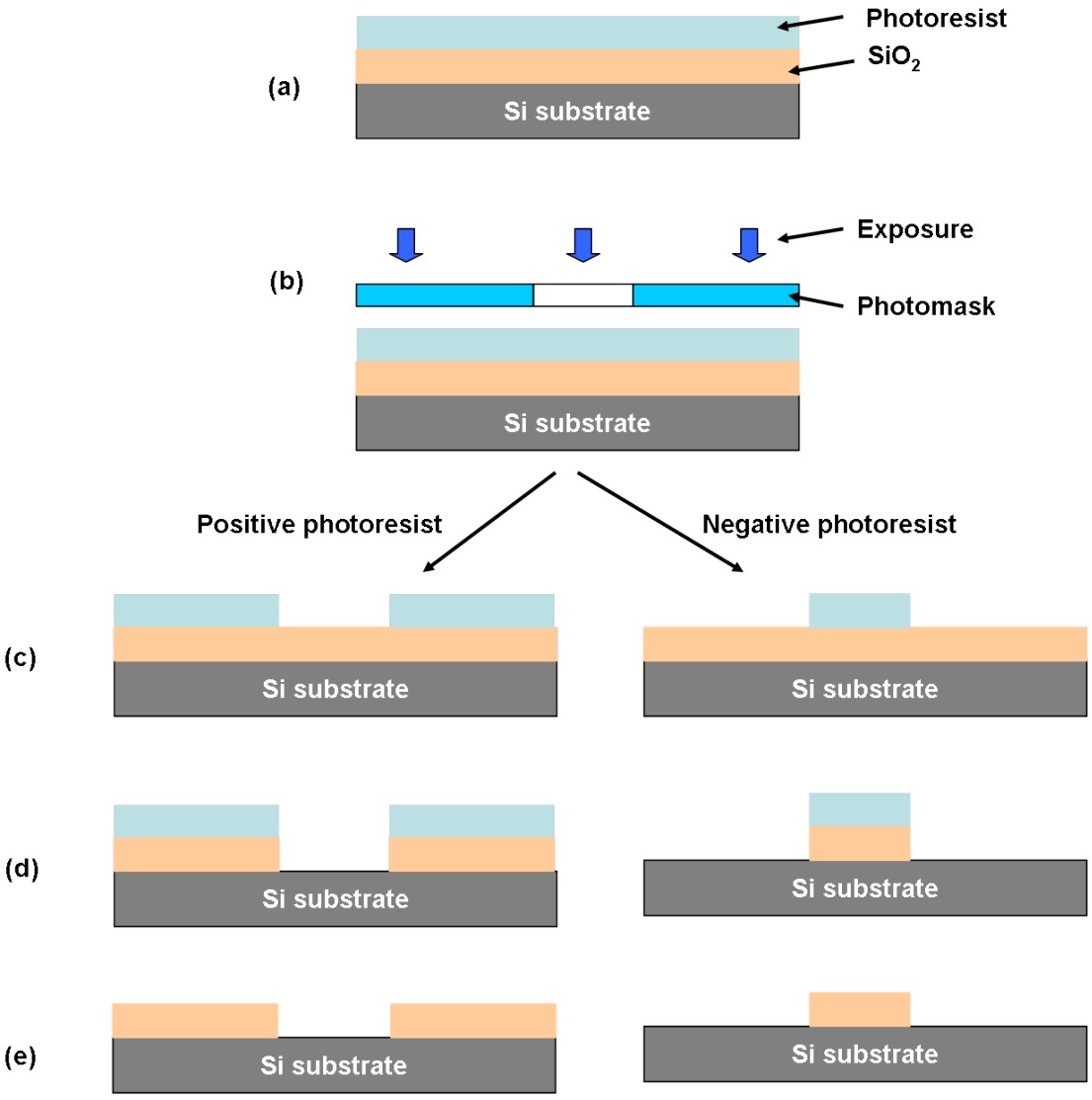

FIGURE 2.7: Pattern transfer processes by photolithography for positive and negative photoresists, respectively.

the wafer surface in the yellow room, photoresist is coated on the surface of SiO_2 as shown in figure 2.7(a). After a pre-bake to remove the solvent from the photoresist and to increase resist adhesion to the wafer, the wafer is then aligned with a photomask and exposed by UV light in figure 2.7(b). If a positive photoresist is used the exposed photoresist is dissolved in the developer; if a negative photoresist is used the unexposed photoresist is removed (figure 2.7(c)). After a further baking step, the wafer is put into a chemical solution or a plasma-assisted dry etching system to etch the exposed SiO_2 without damaging the SiO_2 under the photoresist layer, as shown in figure 2.7(d). Finally, the photoresist is removed, leaving a transferred pattern of SiO_2 (figure 2.7(e)). This SiO_2 pattern may also be used as a mask for subsequent etching.

Lift-off is another pattern transfer process. For this method, a photoresist pattern is formed on the substrate first as shown in figure 2.8 (a) and (b). A metal film is then deposited over the photoresist pattern and substrate in figure 2.8(c). The metal on the photoresist is removed by immersing the sample in an appropriate solvent, achieving the required final metal pattern as shown in figure 2.8(d). The patterns for the Ni/Au spreading layer and Ti/Au pads in our LED devices are mainly fabricated by this technique.

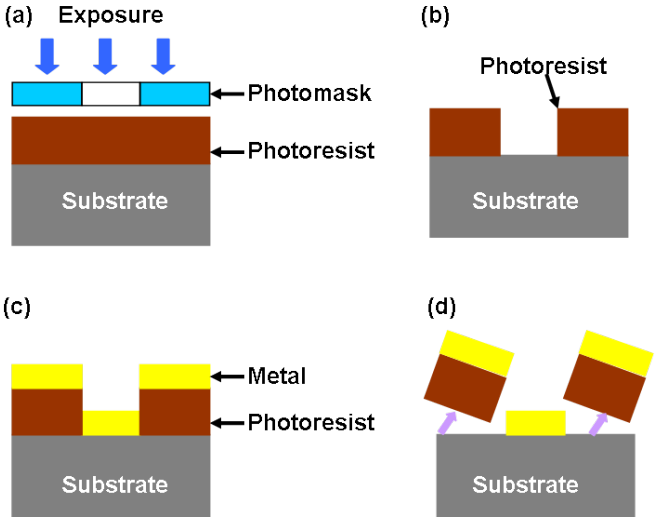

FIGURE 2.8: Metal lift off process for pattern transfer.

2.1.5 SiO_2 deposition

In this work, SiO_2 films are deposited by PECVD at temperature $\sim$ 300 °C using an Oxford Plasmalab 80+ PECVD System. Chemical vapour deposition (CVD) is defined as

the formation of a non-volatile solid film on a substrate by the reaction of vapour phase chemicals that contain the required constituents. The reactant gases are introduced into the chamber and are decomposed and reacted at a heated substrate surface to form a thin film. PECVD uses an RF-induced glow discharge to transfer energy into the reactant gases, maintaining a relatively low substrate temperature. In comparison, other deposition methods may require high temperature, so some materials can not be deposited due to their thermal instability. In addition, PECVD can enhance the deposition rate. In this work, the SiO_2 films deposited by PECVD are formed by the following reaction [3]

$$SiH_4 + 2N_2O \rightarrow SiO_2 + 2N_2 + 2H_2. \tag{2.2}$$

As discussed in previous sections, the deposited SiO_2 layer is used as either an etching mask or an isolation layer for micro-LED fabrication.

2.1.6 Metal deposition

In this work, two metal deposition methods are used: sputtering and e-beam evaporation, which are both classified as physical vapour deposition (PVD).

Sputtering

For sputtering, atoms of a material target are dislodged by collision with high energy particles then deposited onto a substrate. The sputtering technique is widely used for metal film deposition due to the following advantages: sputtering can be achieved from large-area targets and as such is suitable for depositing uniform-thickness films over large wafers; the film thickness can be easily controlled by adjusting the deposition time based on the known deposition rate; alloy deposition can be more easily controlled than for evaporated films. However, sputtering also has some drawbacks, including high equipment cost and low deposition rate for some materials (e.g. SiO_2) [3].

Shown in figure 2.9(a) is the CVC AST 601 Sputter System used in this work. It is a DC magnetron sputter system mainly for depositing Ti, Al, and Au as bonding pads for LED device fabrication. The system consists of the deposition chamber, sputtering targets, gas supply, vacuum pumps, power supplies, control interface, etc. The sputtering processes and mechanism in a sputtering deposition chamber are shown in figure 2.9(b).

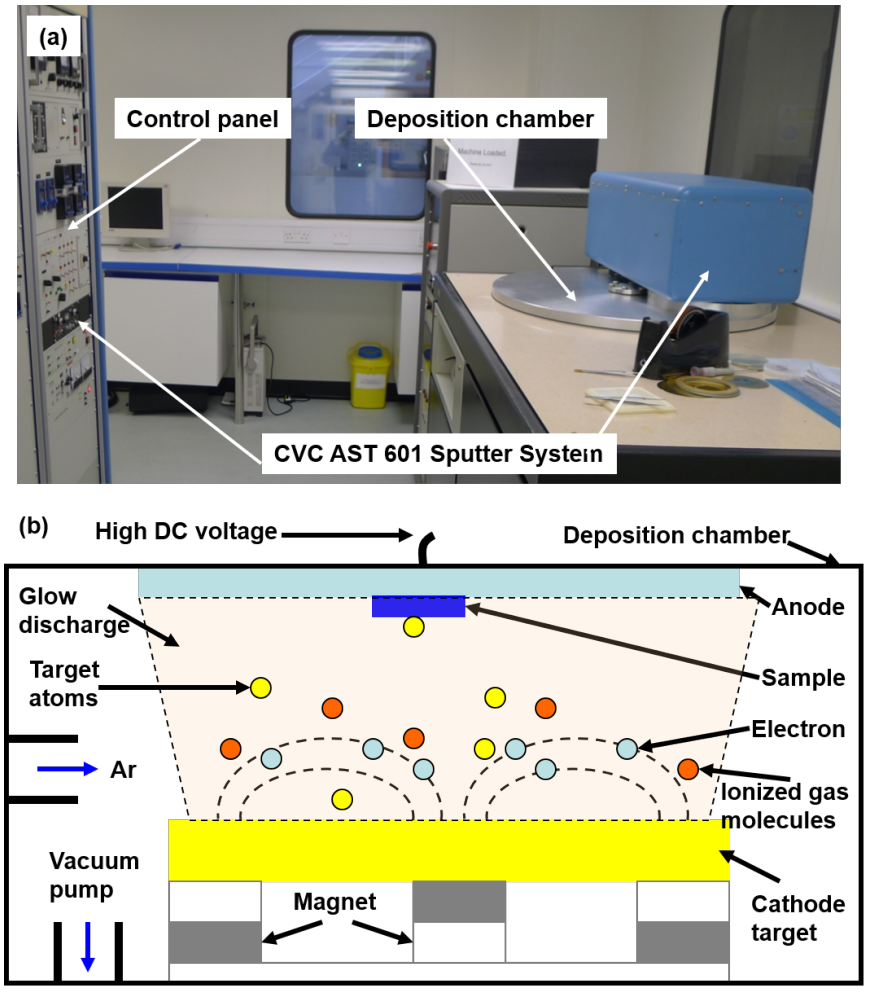

FIGURE 2.9: (a) Photograph of the CVC AST 601 Sputter System. (b) Schematic diagram of the sputtering processes in the deposition chamber.

Generally, the sputtering process consists of four steps: ions are generated and directed at the source targets; target atoms are sputtered by the ions; the sputtered atoms are transported onto the substrates; these atoms form the deposited films.

Direct current (DC), RF and magnetron sputtering are widely used for sputter systems. Compared with RF sputtering, DC sputtering has the drawback that it cannot be used to sputter insulators, e.g. SiO_2, due to the fact that the glow discharge cannot be maintained with a DC voltage if the electrodes are covered with insulating layers. In both DC and RF sputtering systems, most secondary electrons emitted from the target do not cause ionization of Ar atoms, which are collected by the anode, substrates, etc., causing unwanted heating. In comparison, the magnetron sputtering increases the percentage of electrons that cause ionizing collisions, by using magnetic fields to confine the electrons near the target surface. Thus in the magnetron sputtering system, the ionic

bombardment and sputtering rate of the target, and the deposition rate are significantly enhanced.

Vacuum pumps to create the vacuum environment are utilized in a range of equipment, including the sputter system and e-beam system, so it is worth describing the vacuum pumps. Generally, two-stage vacuum pumping, i.e. a roughing pump and a high vacuum pump, are required for a high vacuum system. As an example, figure 2.10 shows the vacuum pump system of the CVC AST 601 Sputter Coater. After venting the chamber by opening the vent valve, samples can be loaded into the chamber. Then the chamber and vent valve are closed for rough pumping by using the mechanical pump (roughing valve open), typically achieving a vacuum of ~ 0.05 Torr. Afterward, the roughing valve is closed and the high vacuum valve is opened for high vacuum pumping by a cryosorption pump, reaching $\sim 5\times10^{-7}$ Torr, which is suitable for metal deposition. The foreline valve is a vacuum valve to connect the diffusion pump and mechanical pump.

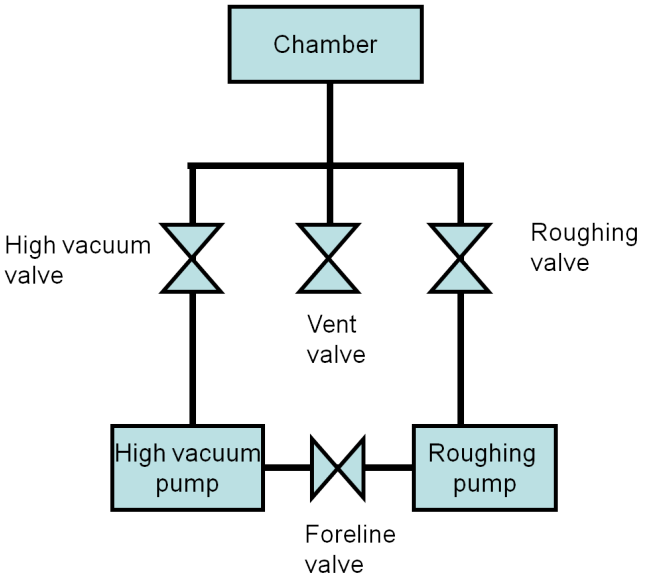

FIGURE 2.10: Schematic vacuum pump system of the CVC AST 601 Sputter System.

Thermal and E-beam evaporation

Thin films can be deposited by heating the source material, causing evaporation and deposition [3]. In a high vacuum environment, typically down to $\sim 5\times10^{-7}$ torr, the vapourized atoms/molecules are likely to strike the substrates/chamber walls without any collisions with other gas molecules. The rate of mass lost from the source per unit

area per unit time, R_{loss}, can be estimated from the Langmuir-Knudsen relation [3]

$$R_{loss} = 4.43 \times 10^{-4}(M/T)^{1/2}p_e \tag{2.3}$$

where M is the gram-molecular mass, T is the temperature in K, and p_e is the vapour pressure in Pa.

Evaporation has been widely utilized for depositing metallic films due to several characteristics, including high deposition rate, low energy of the impinging metal atoms onto the substrate (∼0.1 eV), high-purity deposition, and less unintentional substrate heating (only caused by the heat of atom condensation and heat radiation from the source). However, evaporation suffers from some limitations compared with sputtering deposition, e.g. accurately controlling the alloy compositions.

To achieve maximum uniformity during evaporation, the substrates are normally mounted onto a mechanical rotation fixture inside the chamber and the entire fixture rotates around the vertical axis of the chamber during deposition, resulting in thickness uniformity across a substrate and also from substrate-to-substrate.

E-beam evaporation is one commonly adopted evaporation technique. For e-beam evaporation, a stream of electrons is accelerated to high kinetic energy (5-30 keV), which is directed at the source material to transform the kinetic energy to thermal energy and to melt a small portion of the evaporant material. This eliminates the problem of reaction or dissolution between the crucible and source material, allowing highly pure film deposition.

For e-beam deposition, the surface of the evaporation source may be oxidized when loading and unloading the substrates. These surface contaminants will evaporate when the source is initially heated. To prevent such contamination, a shutter between the source and substrates is normally used and the shutter is only opened after initial evaporation.

Shown in figure 2.11(a) is the EDWARDS AUTO 306 system for e-beam evaporation, used mainly for depositing Ni and Au to form the current spreading layer of micro-LEDs in this work. The schematic diagram of the e-beam chamber is also shown in figure 2.11(b). For this system, a mechanical roughing pump and a diffusion pump for fine pumping are used to achieve a high vacuum environment in the chamber. Four different metal targets can be chosen for multiple layers deposition. An evaporation rate monitor

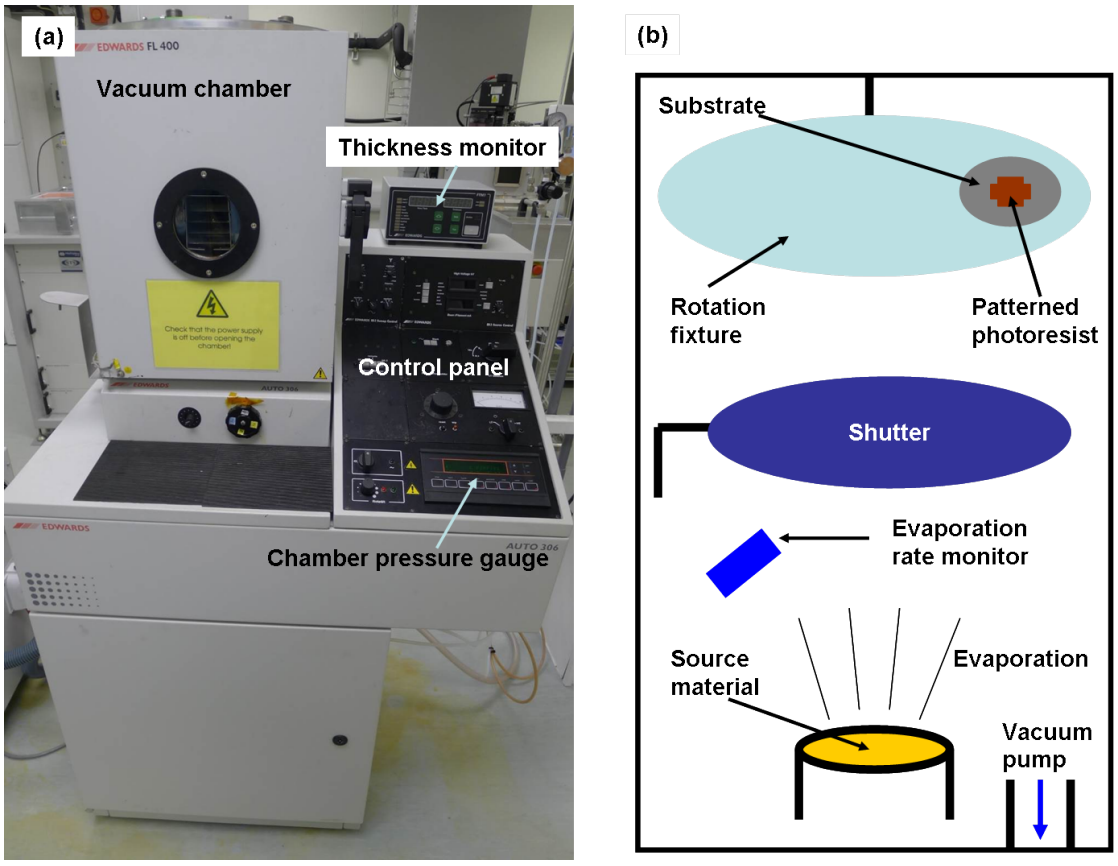

FIGURE 2.11: (a) Photograph of EDWARDS AUTO 306 system for e-beam evaporation. (b) Schematic diagram of the evaporation process in the e-beam chamber.

inside the chamber enables direct reading of metal deposition rate and deposited film thickness.

2.1.7 Rapid thermal annealing

RTA is an important process to form the p-contact and ameliorate the sidewall surface defects of GaN-based LEDs. The equipment used in this work is a Jetfirst RTA System from the JIPELEC company, as shown in figure 2.12(a). The annealing conditions, including gases, temperature and time, can be accurately controlled. Figure 2.12(b) shows the schematic diagram of the RTA chamber for annealing a sample. For a typical RTA process, the sample can be loaded into the quartz chamber inside the RTA chamber. The gas type and flow can be controlled, while vacuum annealing is also optional. In the control panel, multiple steps are usually set to achieve the required temperature for a determined period. Two thermocouples in the centre and on the edge of the carrier wafer are used to evaluate the temperature difference from the wafer centre to the edge.

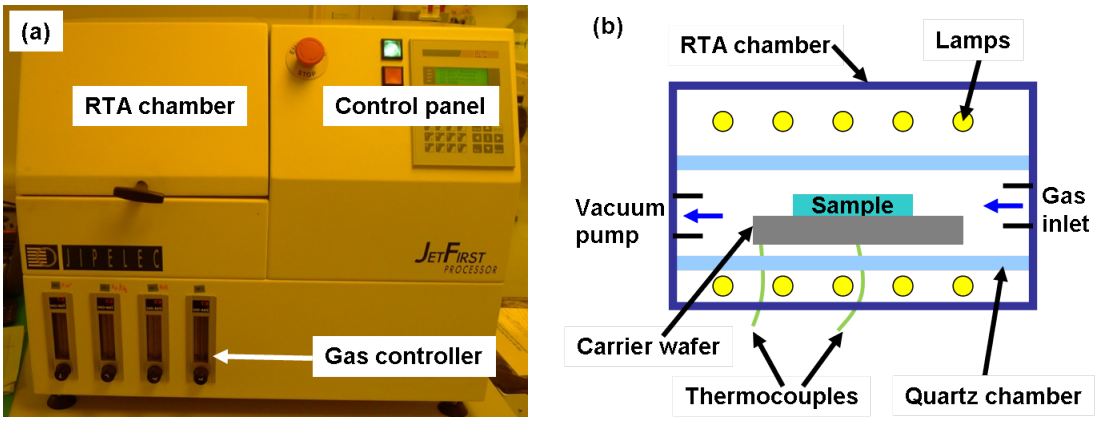

FIGURE 2.12: (a) Photograph of Jetfirst RTA System from JIPELEC company. (b) Schematic diagram of the RTA process in the RTA chamber.

The typical RTA conditions for *p*-type Ni/Au contact of GaN-based LEDs are 2-3 mins annealing at 500 °C in purified air. The LED samples were heated to 500 °C by multiple steps, and in each step the samples were heated to a specified temperature within ~30 s. However, the cooling process is slow to prevent any sample breakage (thermal shock).

2.1.8 Sapphire lift off

For GaN-based LEDs grown on sapphire substrates, the LED performance is limited by the poor thermal conductivity of sapphire. To solve this problem, wafer bonding and LLO techniques have been developed to transfer the GaN layers onto other substrates [4, 5]. These techniques are also used to transfer the LED layers onto flexible substrates where appropriate [6]. In this section, the metal bonding and LLO techniques are described.

Metal bonding

Before using LLO to lift off the sapphire substrates, the samples need to be bonded onto another hard substrate to sustain the local mechanical stress induced during the LLO process (due to the high local temperature caused by the laser spot). Thus, metal bonding in vacuum conditions has been used to bond the GaN-based LEDs onto foreign substrates, e.g. Si substrates. The vacuum bonding equipment in this work and the schematic diagram of the bonding process in the vacuum bonding chamber are shown in figure 2.13(a) and (b), respectively. A typical metal bonding includes three layers, e.g. LED, metal and Si substrate layers. The bonding was performed in low-vacuum condition in the vacuum bonding chamber. In the control panel, multi-steps bonding can be set to accurately control the bonding pressure, temperature and time of each step.

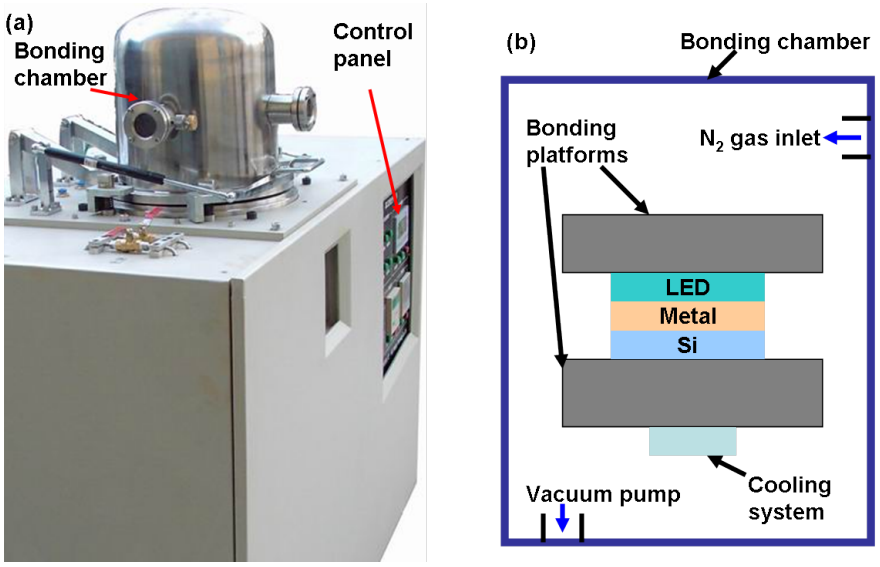

FIGURE 2.13: (a) Photograph of vacuum bonding equipment used in this work. From http://www.hqcbj.com. (b) Schematic diagram of the bonding process in the vacuum bonding chamber.

During the cooling step, a slow vacuum cooling or a quick N_2 gas cooling can be chosen. The details of the bonding conditions will be shown in the related chapter.

LLO

LLO has been widely used to separate GaN layers from their sapphire substrates [4, 5]. A short-wavelength laser, e.g. 355 nm in this work, is used to irradiate from the bottom side of the sapphire. Due to the different bandgap energies of GaN (~3.4 eV) and sapphire (8.7 to 9.4 eV [7]), the laser emission goes through the sapphire substrates and is absorbed by the GaN at GaN/sapphire interface, causing decomposition of the GaN into nitrogen (N_2) and gallium (Ga) metal. The decomposition process can be expressed by the following equation:

$$2\mathrm{GaN} \rightarrow 2\mathrm{Ga}(m) + \mathrm{N}_2(g). \tag{2.4}$$

Micro-area LLO equipment (at Peking University) was used in this work, as shown in figure 2.14(a), which mainly consists of a frequency-tripled, nanosecond-pulse Nd:YAG laser, a LLO chamber for processing samples and a computer control interface. The LLO process in the chamber is shown in figure 2.14(b). To remove the sapphire substrate, a laser energy density of about 600 mJ/cm^2 is used to scan the sample surface line by line. The laser spot size is 80 μm×80 μm which minimizes the structural damage of samples

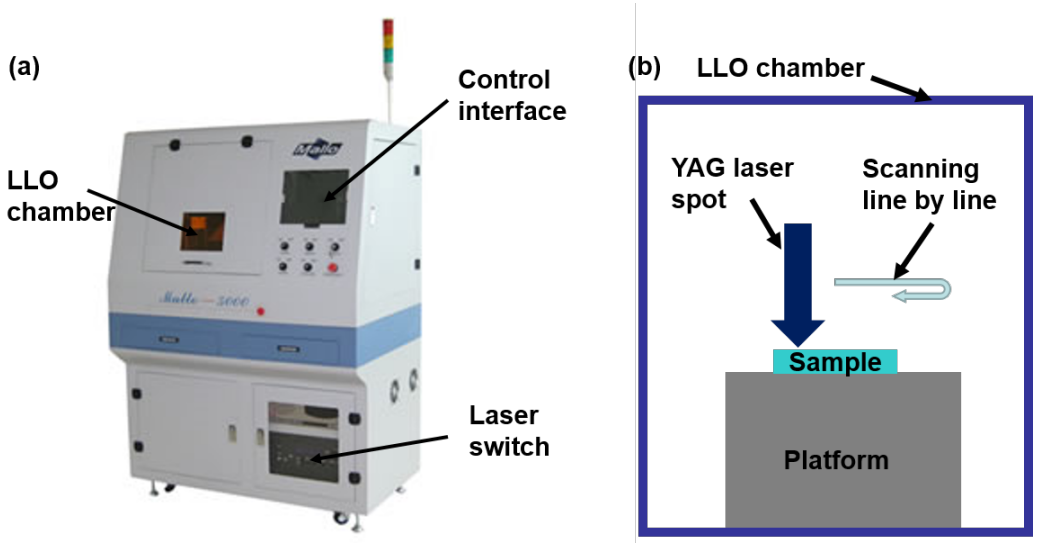

FIGURE 2.14: (a) Photo of micro-area LLO equipment used in this work. From http://www.sinonitride.com. (b) Schematic diagram of the LLO process in the LLO chamber.

[8]. Afterward, the sample is heated at ~80 °C to melt the Ga metal. Then, the sapphire substrate can be easily removed.

2.2 LED characterization techniques

In this work, the fabricated LEDs have been fully characterized to demonstrate their electrical and optical performance and applications. In this section, the techniques to measure the PL spectra and the setup to characterize LED modulation characteristics are described.

2.2.1 Micro-PL

In order to conveniently investigate the luminescence characteristics of LED wafers, a micro-PL setup was built to obtain PL spectra for micro-scale areas. Figure 2.15 shows the schematic micro-PL setup, which mainly consists of a laser diode emitting at 374 nm for optically pumping the structures, a 60× objective lens for focusing the laser beam on the sample, neutral density filters to control the power of the laser beam, a CCD camera for monitoring and aligning the focused laser beam, a lens for guiding the PL emission into the spectrometer, and a filter for filtering the light from the laser diode. A power

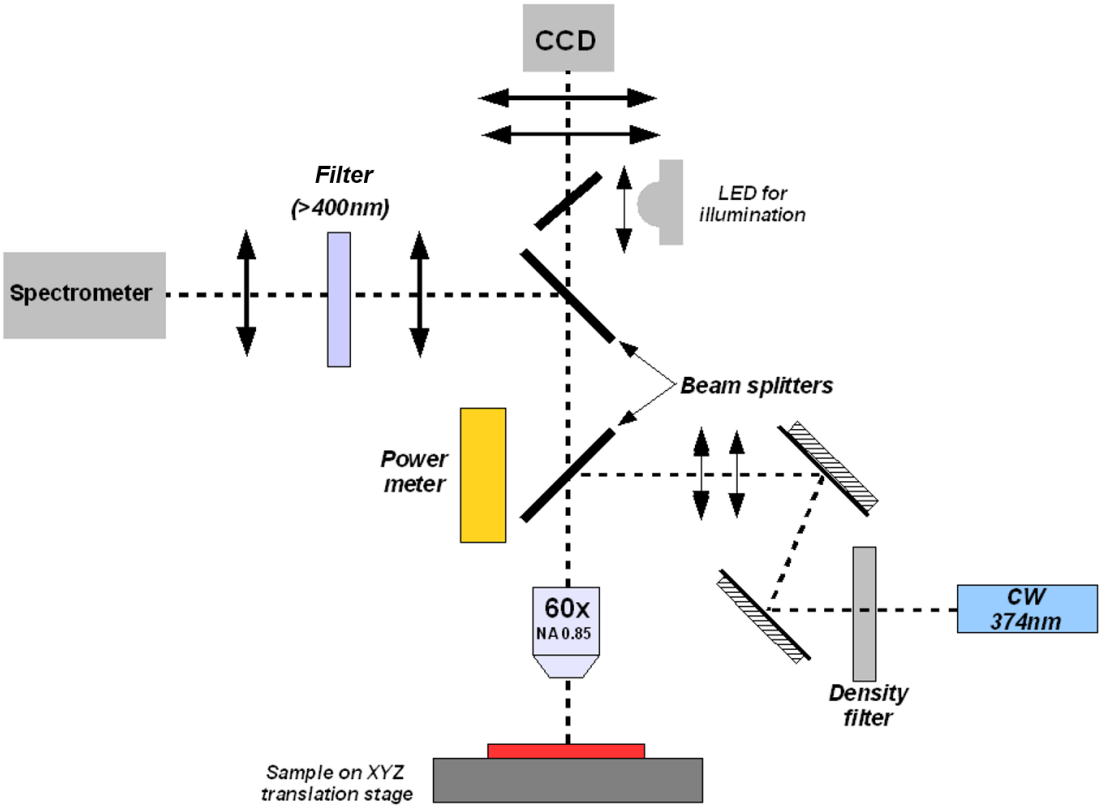

FIGURE 2.15: Schematic micro-PL setup to measure the emission spectra of LEDs. Courtesy of Dr. Benoit Guilhabert.

meter can be used to measure the laser power exciting the sample. In this work, the PL setup is mainly used to test the PL spectra of micro-LEDs with different sizes.

2.2.2 Modulation bandwidth characterization

The micro-LEDs have been successfully applied in VLC [9]. In this work, the VLC capability of micro-LEDs on different substrates has been evaluated by measuring their modulation bandwidth and eye diagrams. The modulation bandwidth of LED partly determines the data transmission speed, and can be also used to evaluate the LED carrier recombination dynamics. The data transmission speed can be evaluated by eye diagrams. This section describes the principle and setup to obtain modulation bandwidth and eye diagrams of LEDs.

The light output power of AC-modulated LEDs depends on the frequency of the alternating current (AC) signal, which defines the frequency response of the LEDs. The bandwidth is the frequency when the LED response reduces to half of its low frequency

response. The bandwidth is also called as -3dB frequency, since the power transmitted at this frequency is reduced by 3 dB compared with its low-frequency value. The frequency response, $P(\omega)$, and the bandwidth, f_{3dB}, are defined by the following equations [10–12]:

$$P(\omega) = \frac{1}{\sqrt{1+(\omega\tau)^2}}, \tag{2.5}$$

and

$$f_{3dB} = \frac{\sqrt{3}}{2\pi\tau}, \tag{2.6}$$

where τ is either the differential carrier lifetime or $R_{series}C_D$ time constant of the LEDs with R_{series} and C_D representing the series resistance and capacitance, respectively.

Figure 2.16 shows the schematic setup to measure the frequency response of an LED device. During the measurement, the LED was electrically biased by a DC power supply, and AC modulated by a network analyser (Agilent Technologies 8753ES Option 011). The AC signal is a chirped sine wave of fixed amplitude, and is combined with DC signal by a three-terminal bias-tee. The light emission of the micro-LED is collected by lenses and delivered to a 1.4 GHz bandwidth photodiode. For initial characterization, the distance between the micro-LED and photodiode is short (~10 cm), i.e., these are back-to-back measurements. The output of the photodiode is sent to the input port of the network analyser. Thus, the amplitude of the optical signal into the photodiode is transferred into an electrical signal, and recorded by the network analyser as a function of frequency. The photocurrent from the photodiode is proportional to the light output

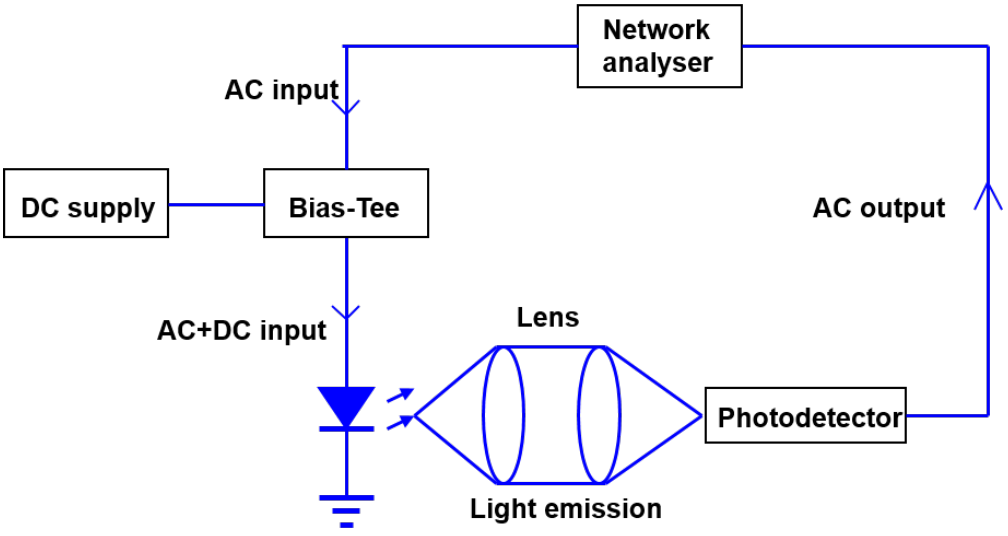

FIGURE 2.16: Schematic setup to measure the frequency response of a LED device.

power collected from the LED, while the network analyser measures the electrical power from the photodiode. In this case, the measured electrical power by network analyser is proportional to the square of the light output power of LEDs, and as such the optical -3dB point of LED is equivalent to -6 dB point of the measured electrical power by network analyser.

To evaluate the optical data transmission of LEDs, datastream transmission tests have been carried out which use pseudo-random binary sequences combining with a DC voltage, a non-return to zero (NRZ) data signal with a standard pattern length of 2^7-1 bits and a peak-to-peak voltage swing of 0 to 2 V. The pattern length of 2^7-1 bits is often used to test Ethernet communication systems as it provides a good approximation to actual Ethernet. Thus, to test the VLC capability of LEDs, pattern length of 2^7-1 bits was used. For the NRZ signal, 0 and 1 logic levels can be represented by the low and high voltage levels, respectively. Furthermore, an eye diagram can be constructed by sampling the received signal and overlaying the obtained data. The eye diagram provides visual information of the noise and jitter, and an open eye diagram indicates that the data transmission can be error-free. In addition, regarding the data transmission distance, in the project "ultra-parallel visible light communications" led by the Institute of Photonics, we have achieved >1 Gbit/s free-space transmission up to 10 m and 4 Gbit/s transmission over 10 m plastic optical fibre (POF) using blue micro-LEDs. However, for POF communication, the data transmission is limited by the micro-LED spectral width, absorption of POF, and multimodal dispersion in POF. Such dispersion influences the communication by broadening the output pulse compared with the input pulse [13].

2.3 Summary

The fabrication and characterization techniques of micro-LEDs have been discussed in this chapter, mainly concerning the principles and the equipment used in this work. More application details of these techniques in LEDs on different substrates will be provided in each chapter.

References

[1] S. M. Sze. *Semiconductor devices: physics and technology.* John Wiley & Sons, 2008.

[2] H. Conrads and M. Schmidt. Plasma generation and plasma sources. *Plasma Sources Science and Technology*, 9(4):441, 2000.

[3] S. Wolf and R. N. Tauber. *Silicon processing for the VLSI era, volume 1: process technology.* Lattice Press, Sunset Beach, CA, 2000.

[4] W. S. Wong, T. Sands, N. W. Cheung, M. Kneissl, D. P. Bour, P. Mei, L. T. Romano, and N. M. Johnson. Fabrication of thin-film InGaN light-emitting diode membranes by laser lift-off. *Applied Physics Letters*, 75(10):1360–1362, 1999.

[5] Y. Sun, S. Trieu, T. Yu, Z. Chen, S. Qi, P. Tian, J. Deng, X. Jin, and G. Zhang. GaN-based LEDs with a high light extraction composite surface structure fabricated by a modified YAG laser lift-off technology and the patterned sapphire substrates. *Semiconductor Science and Technology*, 26(8):085008, 2011.

[6] T. I. Kim, Y. H. Jung, J. Song, D. Kim, Y. Li, H. S. Kim, I. S. Song, J. J. Wierer, H. A. Pao, Y. Huang, and J. A. Rogers. High-efficiency, microscale GaN light-emitting diodes and their thermal properties on unusual substrates. *Small*, 8(11):1643–9, 2012.

[7] Y.-N. Xu and W. Y. Ching. Self-consistent band structures, charge distributions, and optical-absorption spectra in MgO, α-Al_2O_3, and $MgAl_2O_4$. *Physical Review B*, 43(5):4461, 1991.

[8] Y. Sun, T. Yu, H. Zhao, X. Shan, X. Zhang, Z. Chen, X. Kang, D. Yu, and G. Zhang. Microanalyses of the reverse-bias leakage current increase in the laser lift off GaN-based light emitting diodes. *Journal of Applied Physics*, 106(1):013101, 2009.

[9] J. J. D. McKendry, R. P. Green, A. E. Kelly, Z. Gong, B. Guilhabert, D. Massoubre, E. Gu, and M. D. Dawson. High-speed visible light communications using individual pixels in a micro light-emitting diode array. *IEEE Photonics Technology Letters*, 22(18):1346–1348, 2010.

[10] E. F. Schubert. *Light emitting diodes*. Second edition, Cambridge University Press, 2006.

[11] J. J. D. McKendry, D. Massoubre, S. Zhang, B. R. Rae, R. P. Green, E. Gu, R. K. Henderson, A. E. Kelly, and M. D. Dawson. Visible-light communications using a CMOS-controlled micro-light-emitting-diode array. *Journal of Lightwave Technology*, 30(1):61–67, 2012.

[12] R. P. Green, J. J. D. McKendry, D. Massoubre, E. Gu, M. D. Dawson, and A. E. Kelly. Modulation bandwidth studies of recombination processes in blue and green InGaN quantum well micro-light-emitting diodes. *Applied Physics Letters*, 102(9):091103, 2013.

[13] O. Ziemann, J. Krauser, P. E. Zamzow, and W. Daum. *POF handbook*. Second edition, Springer, 2008.

Chapter 3

Size-dependent efficiency and efficiency droop of blue micro-LEDs

This chapter describes the size effect on the efficiency and efficiency droop of micro-LEDs ranging from 6 μm to 105 μm in diameter. The main results of this chapter have been published in *Appl. Phys. Lett.* **101**, 231110 (2012). The previous efficiency research of micro-LEDs is first introduced, including the effects of current spreading, sidewall defects, strain relaxation and whispering gallery (WG) modes. Then device fabrication and characterization are described. The results show that smaller micro-LEDs have a higher efficiency at high current densities, which is realized by improved current spreading. Owing to the higher ratio of sidewall perimeter to mesa area of the smaller micro-LEDs, lower efficiency was observed at low current densities, which is attributed to the increased Shockley-Read-Hall (SRH) non-radiative recombination through sidewall defects caused by dry etching. It is also demonstrated that such sidewall defects can be partially recovered by increased thermal annealing time and thereby that the efficiency can be improved at low injection current density. The efficiency characteristics of these micro-LEDs have also been simulated, and the simulation and experimental trends agree well. The size dependent efficiency and efficiency droop research will help the further LED design with higher efficiency and alleviated efficiency droop.

3.1 Overview of micro-LED efficiency research

InGaN LEDs commonly suffer from a reduction in external quantum efficiency (η_{EQE}) at a high injection current density, named efficiency droop [1]. Several mechanisms (Chapter 1) have been proposed to explain the efficiency droop effect, such as Auger recombination [2, 3], carrier delocalization [4], defect recombination which is strongly dependent on current density [5], poor hole injection and electron leakage [6]. Among these mechanisms, Auger recombination and electron leakage are proposed as the most probable droop mechanisms at high injection current density. However, to date, the origin of efficiency droop is still not fully understood.

Regarding chip design to alleviate the droop effect, current crowding, which may cause high local non-radiative recombination due to local high current density, can increase the efficiency droop at high current densities [7–9]. Thus, optimized chip design with uniform current spreading provides the opportunity to reduce efficiency droop [10]. It was demonstrated recently that micro-LEDs possess excellent current spreading characteristics compared with commonly used broad-area LEDs [11]. It was also reported that the micro-LEDs can sustain a very high injection current density (>10 kA/cm^2) [11] and that the improved efficiency of micro-LEDs could be due to uniform current spreading [11, 12], strain relaxation [13], enhanced light extraction efficiency [14, 15], but meanwhile might be reduced by sidewall defects [16]. Based on these results, it is expected that a systemic study on size-dependent LED efficiency and efficiency droop will provide insight into the mechanisms of droop, and that the micro-LED approach may offer the potential to improve overall LED efficiency and efficiency droop. In recent studies on the size-dependent LED efficiency and efficiency droop, smaller LEDs (∼25 μm) have shown higher efficiency than larger LEDs at a same input power density, 160 mW/mm^2, owing to the improved heat dissipation [12], and smaller LEDs show less temperature-dependent droop at same current and are thus higher temperature-tolerant [16]. However, a systematic investigation on size-dependent LED efficiency and efficiency droop from a low injection current density around several A/cm^2 to a high injection current density of more than 1 kA/cm^2 and detailed analysis of the underlying droop mechanisms have not been reported.

In this section, an overview of previous efficiency research regarding the special characteristics of micro-LEDs is given, especially in regard to the current spreading and sidewall

defects effect.

3.1.1 Improved current spreading of micro-LEDs

The theoretical and experimental investigation of current spreading on conventional LEDs will also apply in micro-LEDs. Thus, the previous research of current spreading effect on conventional LEDs is summarized, and LED fabrication using micro-LEDs to improve current spreading is introduced.

Effect of current spreading on conventional LEDs

The conventional GaN-based LEDs are grown on insulating sapphire substrates and mesa structures with lateral current injection are commonly used. The schematic structure of a typical GaN-based LED with lateral current path is shown in figure 3.1. Through analysis by Kirchhoff's current law, the current density distribution as a function of x can be obtained, where x is the distance from the mesa edge [17]. At forward bias with operation current densities larger than tens of A/cm^2, the current density distribution can be expressed as

$$J(x) = J(0)\, exp(-x/L_s), \tag{3.1}$$

$$L_s = \sqrt{(\rho_c + \rho_p t_p)\, t_n/\rho_n}, \tag{3.2}$$

where $J(0)$ denotes the current density on the mesa edge, and ρ_c, ρ_p, ρ_n, t_p, t_n are resistivities of p-contact, the p and n-type layers, and thicknesses of p and n-type layers,

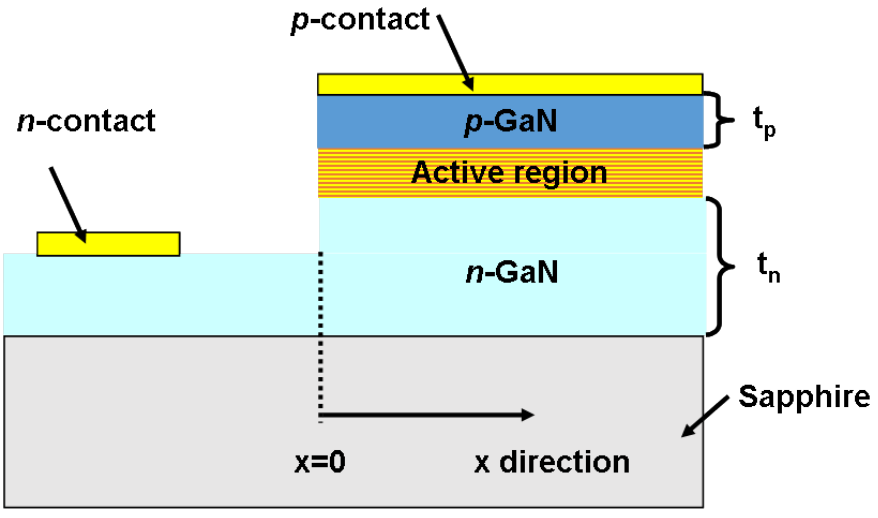

FIGURE 3.1: Schematic GaN-based LED structure with lateral current path. Reproduced from [17].

respectively. L_s denotes the current spreading length, defined as the length at which the current density is reduced to 1/e of the current density at the mesa edge.

From equation 3.2, it is evident that the resistivity of the n-type buffer layer should be as small as possible to the minimize current crowding effect, while a large p-type resistance helps to achieve uniform current spreading. For the LED device with large contact size, the current crowding effect becomes more severe, and thus novel contact geometries such as interdigitated structures have been used.

Figure 3.2(a) shows typical 1×1 mm^2 blue LEDs on sapphire substrates with an interdigitated p-contact [7]. To qualitatively estimate the current crowding effect on electrical

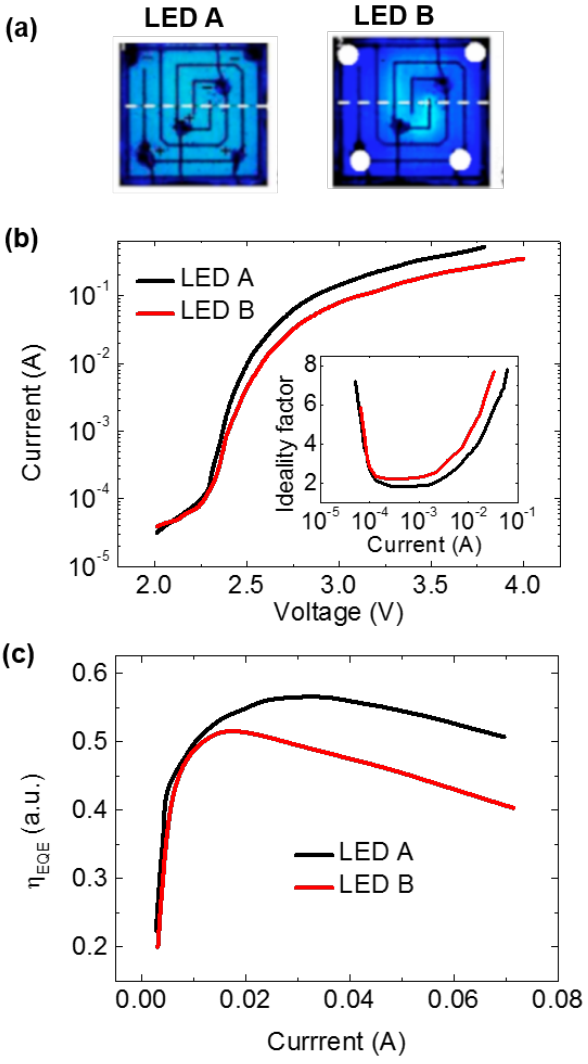

FIGURE 3.2: (a) Spatial distribution of light output power of LED A with six bonding wires and LED B with two bonding wires. (b)Experimental I-V curves of LED A and LED B. Inset: the ideality factor versus current characteristics. (c)η_{EQE} versus current characteristics. Reproduced from data in [7].

and optical properties, two LEDs, i.e. LED A and LED B were designed and fabricated. For LED A, six contact wires were bonded on three p-contact and three n-contact pads. For LED B only two contact wires were used in the center of the chip, creating a current crowding geometry. As shown in figure 3.2(b), the I-V and the ideality factor characteristics are affected by current crowding at current larger than $\sim 10^{-4}$ A. In addition, η_{EQE} versus current characteristics of these two devices were also obtained. In figure 3.2(c), the behaviour of both LEDs is similar only in the low current domain, consistent with the I-V behaviour. However, LED A greatly outperforms LED B at high current larger than 15 mA, and LED B reaches its peak η_{EQE} at $\sim$35 mA compared to $\sim$15 mA for LED B. The current crowding effect of LED B enhances the local overheating and local non-radiative recombination, causing the lower efficiency at high current.

Numerical modelling has also been employed to simulate the current crowding effect on efficiency droop. It is found that the devices with low uniformity of current spreading suffer from higher efficiency droop which agrees with experimental results well [8], and the temperature dependence of efficiency droop can be explained by the current crowding effect as well [9]. The current crowding becomes more serious at higher current and lower temperature, contributing significantly to the droop effect. According to the current crowding model in equation 3.1 and 3.2, increasing resistivity of p-type current spreading layer, increasing thickness of n-GaN layer and decreasing sheet resistance of the n-GaN layer have been used to simulate LED efficiency, and reduced droop effect has been found [10]. Thus, to alleviate the efficiency droop effect, designing a LED chip with uniform current spreading is critically important.

Improved current spreading effect by employing micro-LEDs

The excellent current spreading and thermal dissipation ability of micro-LEDs have been demonstrated by several groups [11, 12, 16]. The smaller micro-LEDs can sustain a much higher current density and can achieve a higher power density. Thus, LED devices based on micro-LEDs technology have been fabricated to achieve high light output power [18–20].

Gong et al. carried out a systematic study of size-dependent light output power, spectral shift and self heating of micro-LEDs with different sizes [11]. As shown in figure 3.3(a) and the inset of figure 3.3(a), smaller LEDs can deliver higher light output power density despite the lower absolute light output power and are able to sustain much higher

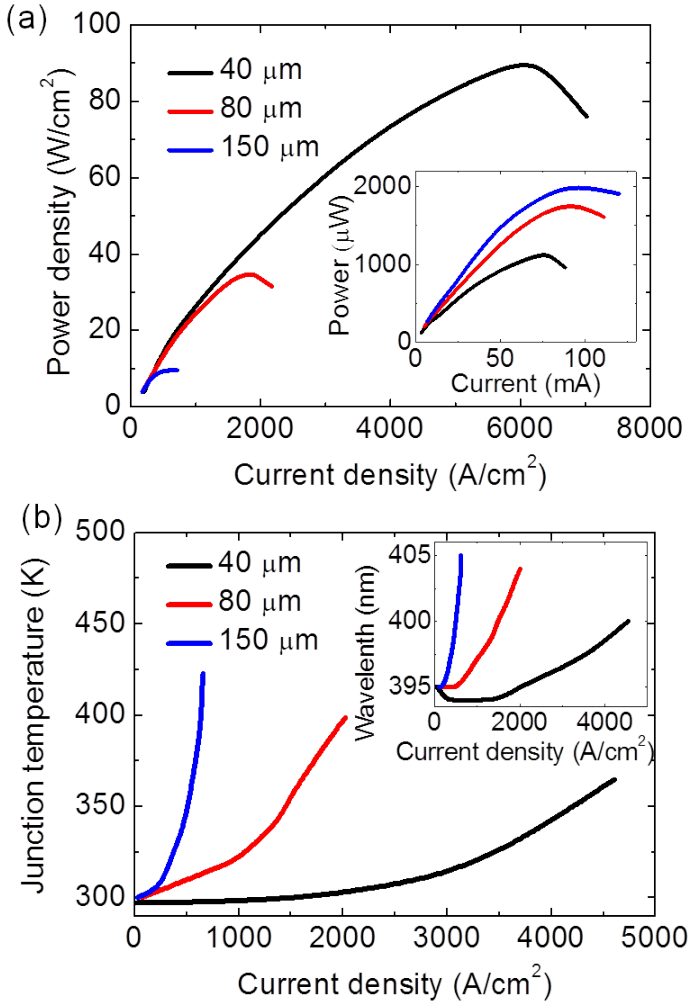

FIGURE 3.3: (a) Power density versus current density (inset: light output power versus current) and (b) junction temperature versus current density (inset: EL peak shift versus current density) for micro-LEDs with different sizes. Reproduced from data in [11].

current densities. The underlying mechanisms were investigated by measuring the junction temperature (figure 3.3(b)), demonstrating much less self heating effect for smaller micro-LEDs. The junction temperature was obtained through comparing the EL spectra peak under direct current (DC) (inset of figure 3.3(b)) and pulsed current [21].

Ploch et al. reported the use of the ultraviolet (UV) micro-LED arrays, consisting of interconnected micro-LEDs, to achieve more uniform current injection, reduced series resistance and improved heat dissipation [18]. As shown in figure 3.4, UV LEDs on sapphire substrates were fabricated with different design geometries by keeping the area of the p-contact fixed at 0.01 mm^2 for comparison. The different geometries are square contact, interdigitated finger contact with a finger width of 20 μm, and micro-LED arrays

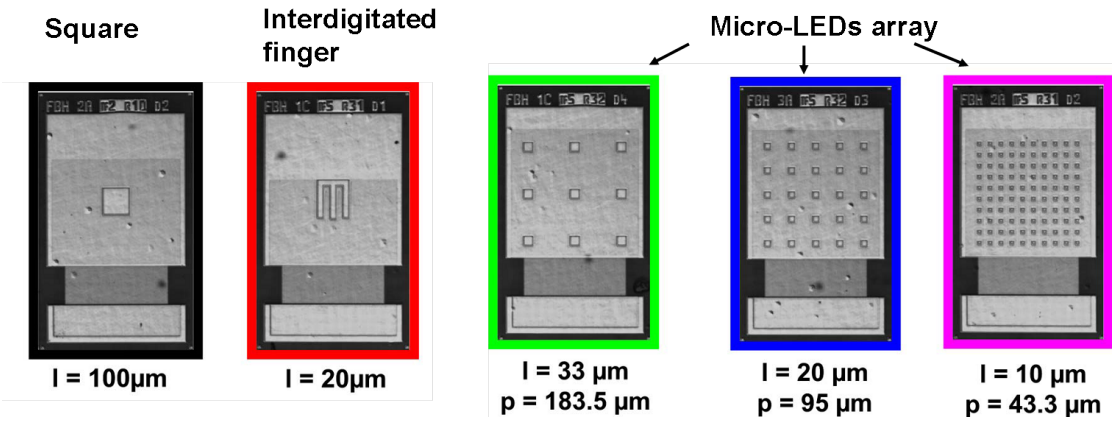

FIGURE 3.4: Optical microscope images of UV LEDs with different design geometries. l is the length of the pixel or finger width and p is the pitch of the array. Adapted from [18].

with pixel sizes of 10, 20, and 33 μm and pitch of 43.3, 95, and 183.5 μm, respectively. A decrease of series resistance, increase of saturation current, and increase of maximum light output power was found for micro-LED arrays with smaller micro-LED sizes. With the help of experiments and simulations, twofold decrease in the thermal resistance of device was found with the use of micro-LED arrays. The thermal resistance linearly decreases with the size of individual micro-LED, indicating that the improved heat dissipation is mainly due to the division of the heat source from one large LED area into smaller pixels and thus the generated heat can be dissipated efficiently [18]. Similarly, a group from University of South Carolina also reported that deep UV LEDs employing micro-LEDs array with small pixel sizes can sustain a high DC current [20], and they have demonstrated a deep UV micro-LED lamp with a light output power ~20 mW at 220 mA [19].

3.1.2 Sidewall defects effect of micro-LEDs

The small size of micro-LEDs provides more uniform current spreading. However, these micro-LEDs suffer from sidewall defects damage due to large relative sidewall area. The sidewall defects are usually caused by plasma damage during inductively coupled plasma (ICP) etching, which may degrade I-V and efficiency of the micro-LEDs. The sidewall defect effects of LEDs with different micro-size structures has been investigated by several groups [22, 23].

To investigate the sidewall defects effect, an array of microholes with a diameter of 1 or 3 μm and spacing of 2-10 μm were created on a 300×300 μm^2 blue LED surface as shown in figure 3.5(a) [22]. The holes were etched by ICP etching through the multiple quantum well (MQW) region down to the n-GaN layer. The effect of plasma damage on the optical characteristics can be seen at a low injection current. In figure 3.5(b), the light output power versus current curve of a LED with 3 μm microhole array is compared with that of standard LEDs. Plasma-induced sidewall defects act as nonradiative recombination centres and may significantly reduce the radiative recombination and light output power at low injection current. These sidewall defects can be recovered by annealing and chemical treatment as shown in this study.

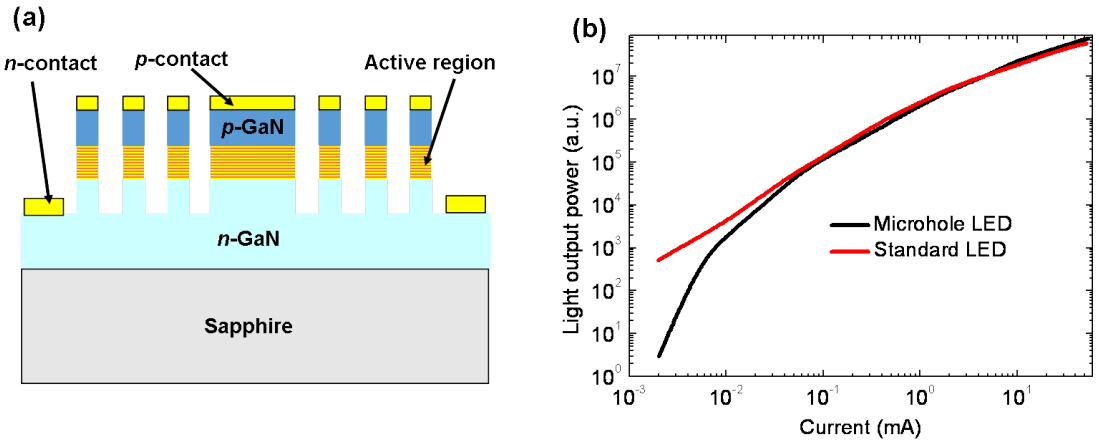

FIGURE 3.5: (a)Schematic structure of GaN-based LEDs with a microhole array incorporated in the MQWs. (b)Light output power versus current characteristics of blue LEDs with and without a microhole array. Reproduced from data in [22].

The size effect on the sidewall defect recombination of micro-LEDs has been investigated quantitatively by our group [23]. Through measuring the modulation bandwidth and using a carrier recombination model, the SRH recombination coefficient A was extracted by an interpolation method. In figure 3.6, the A coefficients are given as a function of micro-LEDs diameter for blue and green wavelengths. The values of the A coefficients are in the range of $\sim 10^8$ s^{-1}. For both wavelengths, a decreasing trend of A coefficients with larger micro-LEDs can be found, which is attributed to the strong sidewall defect recombination.

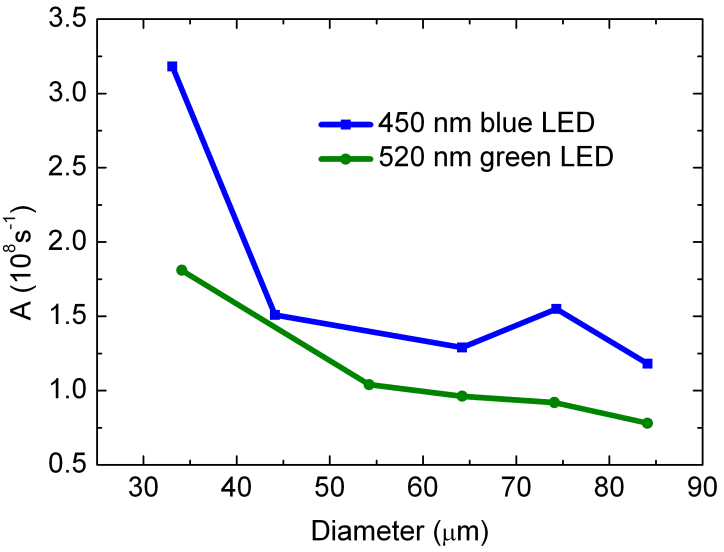

FIGURE 3.6: The A coefficients of micro-LEDs as a function of micro-LED diameter for blue and green wavelengths, deduced from bandwidth measurement. Reproduced from data in [23].

3.1.3 Strain relaxation of micro-LEDs

Strain relaxation may lead to higher efficiency of micro-LEDs. Strain relaxation of microdisks etched from an InGaN MQWs wafer was initially investigated by Dai et al. [13]. As shown in figure 3.7, photoluminescence (PL) spectra for the microdisks of 6 μm diameter and the InGaN MQW wafer were excited by a laser at a temperature of 10 K. Compared with the original MQWs, a blueshift of the PL peak wavelength, enhancement of the PL intensity and narrowing of the PL linewidth were observed in the microdisks. These characteristics were explained by the reduction of the piezoelectric field due to strain relaxation in the microdisks. Contrary to this observation of strain relaxation, Choi et al. used Raman spectra to study the strain relaxation of micro-LEDs with different sizes and found no peak shift of Raman spectra, arguing no strain relaxation effect for micro-LEDs ranging from 4 to 20 μm in diameter [14]. These different observations probably come from the different device structure and processing steps, e.g. different mesa heights. Recently, Shen et al. found that strain relaxation in MQWs was significantly affected by etched mesa depth [24]. Micro-LEDs with a size of 30 μm in diameter and a large mesa height ($>1.3\mu$m) showed significant strain relief which affected the micro-LEDs efficiency.

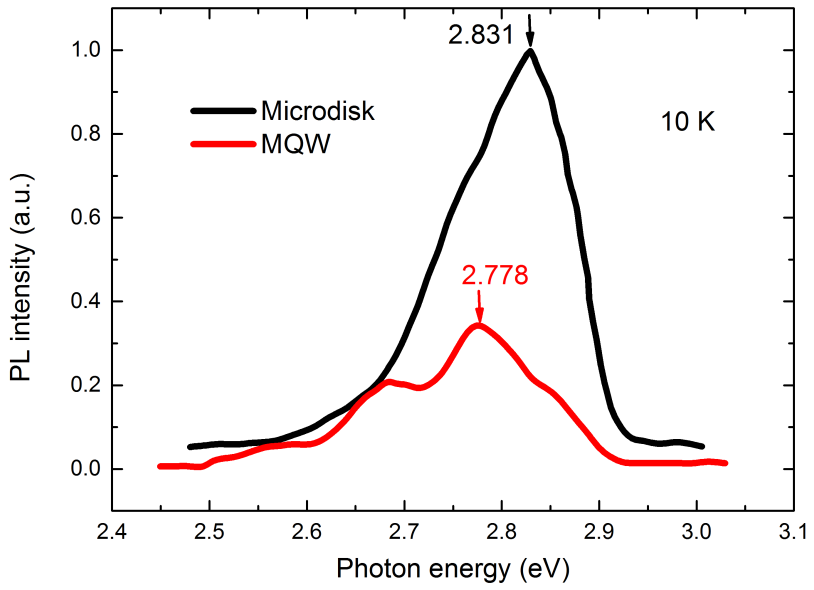

FIGURE 3.7: Low-temperature (10 K) PL spectra of an InGaN MQW wafer and a MQW microdisk sample (6 μm in diameter) under laser excitation. Reproduced from data in [13].

3.1.4 Whispering gallery modes of micro-LEDs

WG modes have been proposed to improve the light extraction efficiency (η_{EXE}) of micro-LEDs [14]. Under a static electron beam, strong light emission at the periphery of the micro-LEDs was found due to light scattering from the sidewalls. And the cathodoluminescence(CL) intensity of micro-LEDs was higher than that of broad-area LEDs. Whispering gallery modes thus play an important role on extracting more light from the sidewall of smaller LEDs. Most of the in-plane propagating light should be emitted through the sidewall in the in-plane direction, but part of the light can be extracted from the top surface due to light scattering on the etched sidewall.

3.2 Experiment

To study the efficiency and efficiency droop of micro-LEDs, InGaN micro-LEDs with different sizes ranging from 6 μm to 105 μm in diameter were fabricated from commercially available ~450 nm wafers grown on *c*-plane sapphire substrates. The LED structure had a conventional *p-i-n* configuration as shown in figure 3.8, with InGaN/GaN MQWs

and a *p*-AlGaN electron blocking layer. An ICP etch was used to define circular LED mesas with different sizes. Then Ti/Au (50 nm/200 nm) layers were deposited around the mesas as the *n*-contact. After that, a silicon dioxide (SiO_2) passivation layer was deposited by plasma-enhanced chemical vapour deposition and SiO_2 apertures on each mesa were then defined by HF-based wet etching. *P*-contacts were formed by Ni/Au (10 nm/25 nm) metal layer deposition, followed by thermal annealing for 2 minutes (denoted as sample A) and 3 minutes (denoted as sample B) at 500 °C in purified air to form emission apertures. The annealing step is essential to obtain ohmic *p*-contacts to the *p*-GaN, and similar contact properties are assumed for sample A and sample B with 2- and 3-minute annealing times. However, the longer anneal gives better recovery of sidewall etch damage as discussed later. Finally, Ti/Au (50 nm/200 nm) layers were deposited onto each pixel to form a *p*-track allowing the LED pixels to be addressed individually. The flip-chip micro-LEDs processing steps are shown in figure 3.8. The micro-LEDs were then attached to a carrier, allowing light to be extracted through the polished sapphire backside. An optical micrograph of the micro-LEDs device is shown

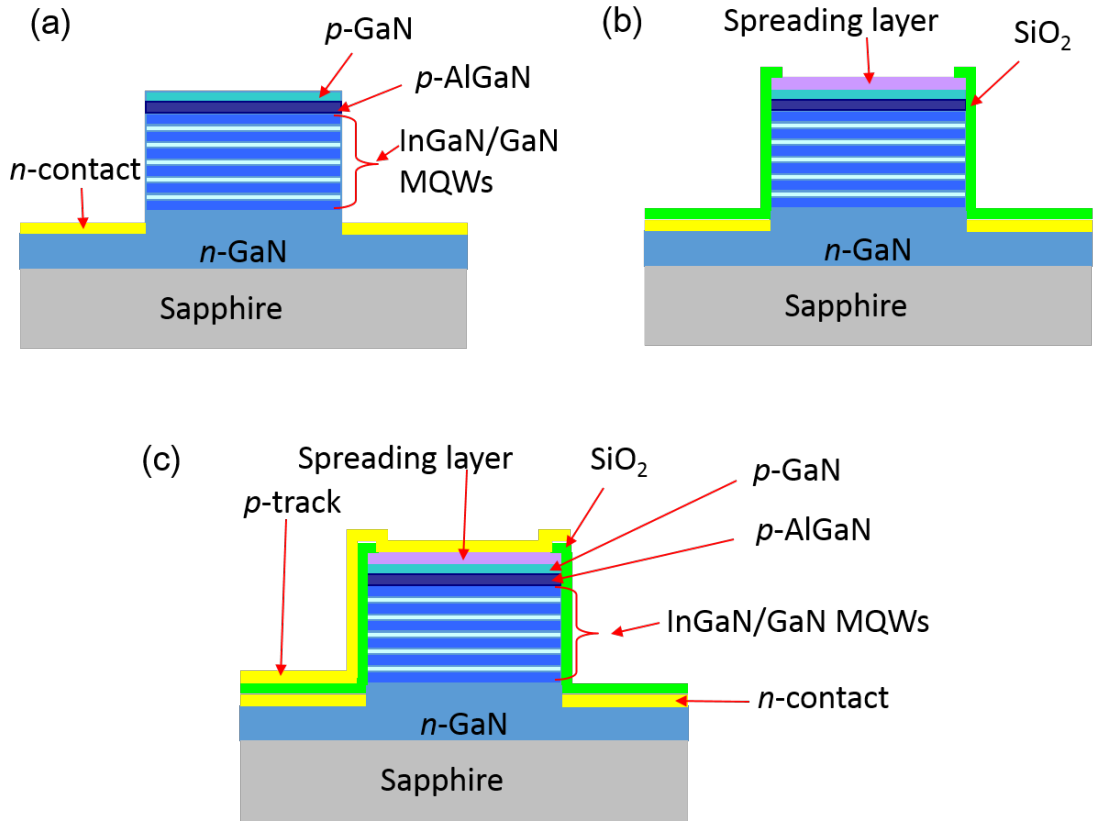

FIGURE 3.8: Schematic processing steps for fabricating micro-LEDs: (a) mesa etching and *n*-type contact deposition, (b) SiO_2 passivation layer deposition and Ni/Au contact formation, and (c) *p*-track deposition.

in figure 3.9.

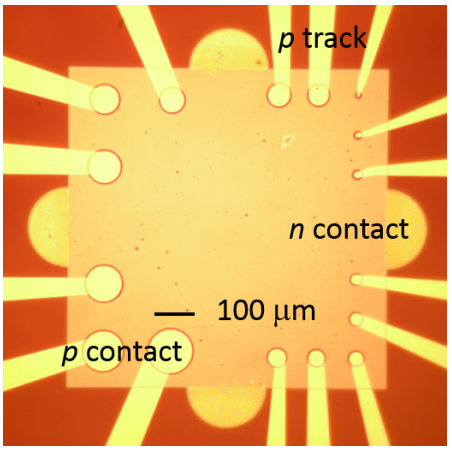

FIGURE 3.9: Optical micrograph of the micro-LEDs with diameters from 6 μm to 105 μm.

The current versus voltage (I-V) characteristics were measured by a probe station connected to an HP1415 network analyzer. The light output power of micro-LEDs was measured by a photomultiplier tube under pulse operation using a voltage source with an electrical pulse duration of 100 μs and a duty cycle of 1%, allowing thermal effects caused by device self-heating to be neglected. These measurements were calibrated by a Si photodetector to make sure the measured light output power from each respective micro-LED could be compared. Photoluminescence (PL) spectra were excited in the centre of the micro-LEDs after etching the LED mesas, by using a GaN laser with wavelength 374 nm and 2 μm diameter spot size (micro-PL). The power incident on the micro-LEDs was controlled by a set of neutral density filters and the excitation optical power for all the micro-LEDs was 5 μW.

3.3 Experimental results

As shown in figure 3.10(a), the injection current density versus voltage characteristics of four micro-LEDs for sample A show a strong size-dependent behaviour. The inset of figure 3.10(a) is to specify the surface leakage current which will be discussed later. It is seen that the injection current density of a 6 μm micro-LED reaches 4000 A/cm^2 at 5 V while that of a 105 μm micro-LED is only 600 A/cm^2 at 5 V. Kim et al. reported that the size-dependent injection current density was strongly related to the current spreading [25]. To estimate the size-dependent current crowding differences, the current

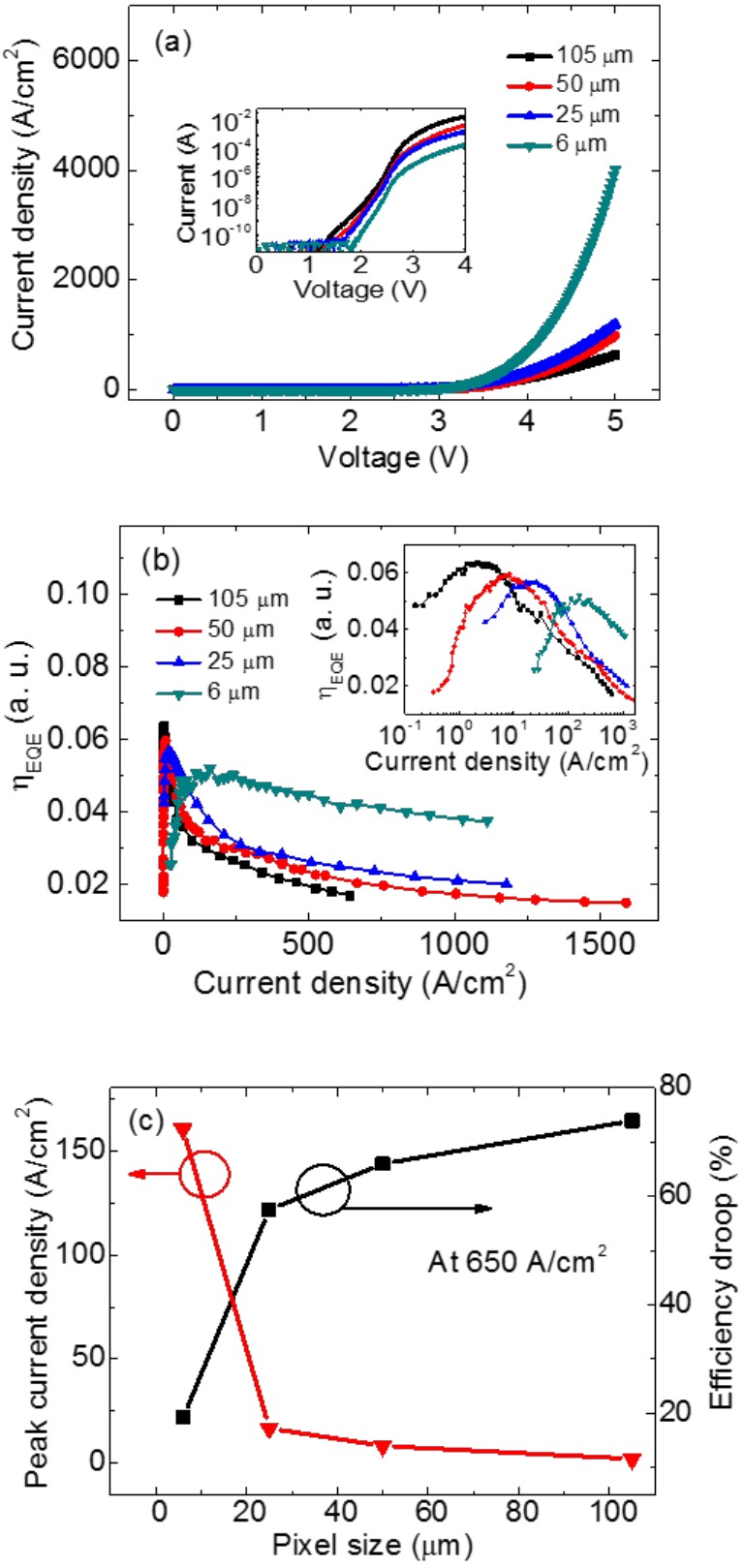

FIGURE 3.10: Size-dependent characteristics of (a) injection current density versus voltage (inset: log (current) versus voltage) and (b) η_{EQE} versus injection current density (inset: η_{EQE} versus $\log(J)$) for sample A. The thermal annealing time of sample A is 2 minutes. (c) η_{EQE} peak current density and efficiency droop at 650 A/cm^2 as a function of pixel size.

spreading length, L_s, defined as the length at which the current density is reduced to 1/e of the current density at the mesa edge, is used to define the current crowding in our micro-LEDs. For our LEDs with reported p-type contact resistivity ρ_c=0.005 Ω cm^2 [26], at injection current density larger than tens of A/cm^2, the current density distribution and L_s can be expressed by equation 3.1 and 3.2, where x denotes the distance from the mesa edge to the centre for micro-LEDs. By using the parameters ρ_p=4.0 Ω cm, ρ_n=0.03 Ω cm, and layer thicknesses t_p=0.15 μm and t_n=3 μm, the current spreading length is calculated to be 71 μm and the ratio of current density in the mesa centre to the current density $J(0)$ at the mesa edge is estimated to be 0.48 and 0.96 for micro-LEDs with diameters 105 μm and 6 μm, respectively. In addition, it has been reported that that the current crowding effect becomes more significant at higher injection current density [10]. Thus, smaller micro-LEDs favour a more uniform current spreading which results in the improved electrical characteristics. As current crowding could strongly affect efficiency especially at very high current density, through local Auger recombination, electron leakage, overheating, etc., we expect that uniform current spreading for smaller micro-LEDs will be an advantage to achieve higher efficiency at a high injection current density. This efficiency enhancement was confirmed and will be discussed as follows.

Through measuring the light output power of sample A, the η_{EQE} values of the micro-LEDs were calculated and are shown in figure 3.10(b); figure 3.10(c) shows the changes of the η_{EQE} peak current density and efficiency droop as a function of LED diameter. Here, η_{EQE} peak current density is the current density at which η_{EQE} reaches the maximum. As shown in the inset of figure 3.10(b), the η_{EQE} peaks at a low current density and then drops with increasing current density for all the micro-LEDs. The relative efficiencies of smaller micro-LEDs are lower at low current densities, but are higher at high current densities. The efficiency enhancement at high current densities is attributed to better current spreading within the smaller micro-LEDs. From figure 3.10(c), when the LED diameter decreases from 105 μm to 6 μm, the η_{EQE} peak current density increases from 2 A/cm^2 to 160 A/cm^2 and the efficiency droop, defined as $(\eta_{EQE}(peak) - \eta_{EQE}(J))/\eta_{EQE}(peak)$ where current density J is 650 A/cm^2, decreases from 75% to 18%. Considering that all the micro-LEDs studied in this work use the same material and device structure, the micro-LED size should be the key factor for the different efficiency and efficiency droop characteristics.

The uniform current spreading could enhance the smaller micro-LEDs efficiency at high

injection current density but the 6 μm micro-LED shows a much larger efficiency enhancement, indicating that another mechanism affects the η_{EQE} of 6 μm micro-LED besides the current crowding effect. Based on our previous work [14], the η_{EXE} of the small micro-LEDs less than 12 μm may be enhanced by sidewall extraction attributable to internal reflection or presence of resonant cavity modes. This can explain the greatly enhanced η_{EQE} of the 6 μm micro-LED at high current densities compared to its larger counterparts. The η_{EXE} of micro-LEDs with sizes larger than 12 μm are not affected by resonant cavity modes as shown in previous studies [14].

PL spectra of the InGaN micro-LED mesas with different sizes were also measured to evaluate the strain relaxation effect on micro-LED efficiency. In figure 3.11, dominant emission peaks around ~2.78 eV correspond to the recombination in the MQWs, and the PL peaks at ~2.94 eV represent Mg-related transition in *p*-GaN as no EL peak at ~2.94 eV can be observed [27]. It is found that the MQW emission peak shows no observable energy shift, which means that piezoelectric fields in MQWs have negligible change for micro-LEDs with different sizes in our samples and thus the effect of strain relaxation on micro-LED efficiency can be neglected.

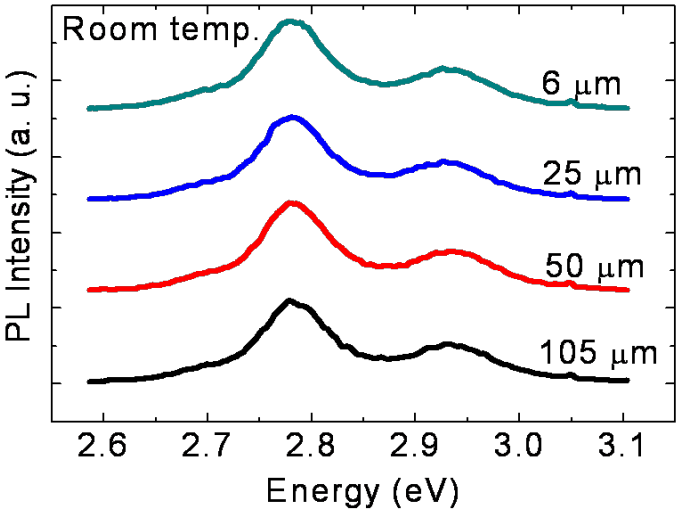

FIGURE 3.11: PL spectra of micro-LEDs with different sizes with MQWs emission peak at ~2.78 eV and Mg-related emission peak at ~2.94 eV.

As shown in figure 3.10(b), at low current densities the smaller micro-LEDs have a lower η_{EQE}, which may be due to the defect-related non-radiative recombination [16]. The ratio of sidewall perimeter to mesa area for 6 μm micro-LED is 17.5 times of that of 105 μm micro-LED which indicates the η_{EQE} of smaller micro-LED at low current density should be more sensitive to the sidewall defects. Therefore we would expect to see an

increase in non-radiative SRH recombination. The internal quantum efficiency (η_{IQE}) of GaN-based LEDs can be expressed (see Chapter 1) by a commonly used simple model [1]

$$\eta_{IQE} = \frac{\eta_{INJ} \cdot Bn^2}{An + Bn^2 + Cn^3}, \tag{3.3}$$

where η_{INJ} represents the injection current efficiency and n represents the carrier concentration. Under low forward bias voltages (V<1.5 V) and a reverse bias V=-5 V, both samples A (as shown in the inset in figure 3.10(a)) and sample B have a very low current less than 10^{-10} A which indicates that the sidewall leakage current of all the micro-LEDs can be neglected [28]. To analyze the defect effect at low current density the electron leakage can also be neglected and thus η_{INJ} can be taken as 1 [1]. The peak efficiency is reached when $d\eta_{IQE}/dn$=0, and therefore the carrier concentration at peak-efficiency point is obtained as n=A/C via equation 3.3. If the defect-related coefficient A, i.e. SRH recombination increases, the η_{IQE} and η_{EQE} will decrease at low n and the η_{EQE} peak will shift to a higher value of n. At low current density, n can be estimated to be proportional to the current density when SRH recombination dominates. Thus, owing to the sidewall defect SRH recombination, it is expected that the smaller micro-LEDs with a high ratio of sidewall perimeter to mesa area will have a lower η_{EQE} at low current densities and their η_{EQE} peaks occur at a higher current density. Such characteristics are clearly observed in figure 3.10(b). To directly demonstrate the effect of sidewall defects, sample B with a thermal annealing time of 3 minutes was compared with sample A with a thermal annealing time of 2 minutes. The aim of increasing the annealing time was to further recover the sidewall defects caused by mesa etching [22], thereby reducing the A coefficient. The annealing time of sample B was chosen to be close to that of sample A to avoid any excessive difference in p-contact resistivity, although the effect of contact resistivity on the η_{EQE} is negligibly small at low injection current density [10]. Compared with the η_{EQE} characteristics of sample A shown in figure 3.10(b), the measured η_{EQE} of sample B (figure 3.12) at low current density has been improved for a smaller micro-LED, but the η_{EQE} of the micro-LED at high current densities does not change very much. As shown in the inset of figure 3.12, the η_{EQE} peak current densities tend to concentrate at a current density around 10 A/cm^2 and the efficiency droop is around 70% at 650 A/cm^2 for all the micro-LEDs. The injection current of a 6 μm micro-LED at a low current density less than 30 A/cm^2 is very small and could not be measured accurately. Thus, for this 6 μm micro-LED, only the η_{EQE} at larger current density is

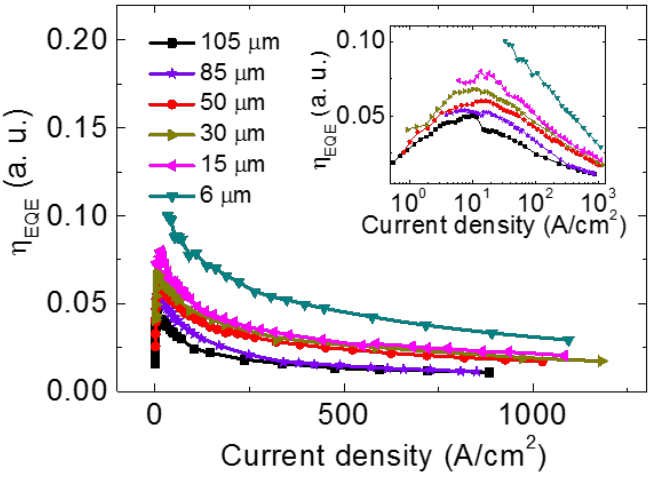

FIGURE 3.12: Size-dependent characteristics of η_{EQE} versus injection current density (inset: η_{EQE} versus $\log(J)$) for sample B. The thermal annealing time of sample B is 3 minutes.

shown. Nevertheless, compared with the 6 μm micro-LED in sample A (figure 3.10(b)), it is evident that the η_{EQE} peak current density of the 6 μm micro-LED in sample B has much decreased. These results show that the sidewall defects of all the micro-LEDs in sample B were further recovered compared to sample A. The reduced efficiency droop of smaller micro-LEDs of sample A is actually caused by the lower efficiency at low current densities due to the sidewall defects. The effective A coefficient increases when micro-LED size decreases, and for a certain LED size, this A coefficient decreases for the device with longer thermal annealing time. Therefore, achieving enhanced recovery of etch-induced sidewall defects has a large effect on the efficiency of smaller micro-LEDs at lower current density, but has much less effect for the larger micro-LEDs.

3.4 Simulation results

The efficiency characteristics of the micro-LEDs were simulated by an advanced device simulation software $APSYS^{TM}$ to further investigate the effect of current spreading and sidewall defects based on the characteristics of sample A.

3.4.1 Physical model of $APSYS^{TM}$

The self-consistent *APSYS* simulation programme is capable of carrying out two-dimensional simulations of carrier transport, calculating the QW effect and heat flux. The carrier transport model includes drift and diffusion of electrons and holes in devices. In the calculation, the built-in polarization induced by spontaneous and piezoelectric polarization is considered at hetero-interfaces of nitride-related devices. In the QWs, self-consistent Poisson and Schrödinger equations are recomputed at every bias point for the states of QW levels and carrier distributions [29–31].

The spontaneous emission spectrum in the active region of InGaN/GaN LEDs can be expressed by

$$r_{sp}(E) = \frac{q^2 h}{2m_0^2 \varepsilon E} D(E)\rho_{red}(E)\left|M\right|^2 f_c^n(E)(1 - f_v^m(E)), \tag{3.4}$$

where q is the free electron charge, h is the Planck constant, $|M|^2$ is the momentum matrix element in the strained QWs, $f_c^n(E)$ and $f_v^m(E)$ are the Fermi functions for the conduction-band states and the valence band states respectively, $D(E)$ is the optical mode density, and $\rho_{red}(E)$ is the reduced density of states in each subband. The indices n and m denote the electron states in the conduction band and the heavy-hole (light-hole) subband states in the valence band. The momentum matrix element is computed from the integration of the envelope functions obtained from the $k \cdot p$ calculation; ε is the strain tensor in the InGaN/GaN QWs.

A Lorentzian lineshape function is used in the expression of the spontaneous emission spectrum to account for the broadening by intraband scattering, which is given by

$$R_{sp} = \frac{1}{\pi} \sum_{i,j} \int r_{sp}(E) \frac{\Gamma}{(E_{ij} - E)^2 + \Gamma^2} dE, \tag{3.5}$$

where $\Gamma = \hbar/\tau$, which represents the broadening due to intraband scattering relaxation time τ, and E_{ij} is the transition energy from the i_{th} conduction band to the j_{th} valence band.

The internal quantum efficiency η_{IQE} of a LED is defined as

$$\eta_{IQE} = \frac{q}{J} \int R_{sp}(V_{active}) dV_{active}, \tag{3.6}$$

where J is the total current density in the device and V_{active} is the volume of the active region.

The physical model of carrier transport is the traditional drift-diffusion model for semiconductor. The specific equation can be expressed as

$$\vec{J}_n(\vec{r}) = q\mu_n n(r)\vec{F}(\vec{r}) + qD_n \nabla n(r), \tag{3.7}$$

$$\vec{J}_p(\vec{r}) = q\mu_p p(r)\vec{F}(\vec{r}) - qD_p \nabla p(r), \tag{3.8}$$

where $n(r)$ and $p(r)$ are the electron and hole concentrations, $\vec{J}_n(\vec{r})$ and $\vec{J}_p(\vec{r})$ are the current densities of electrons and holes, $\vec{F}(\vec{r})$ is the electrostatic field, μ_n and μ_p are the mobilities of electrons and holes. The diffusion constants D_n and D_p are replaced by mobilities using the Einstein relation, $D = \mu k_B T/q$. The equations used to describe the semiconductor device behaviour are current continuity equations for electrons and holes,

$$\frac{1}{q}\nabla \cdot \vec{J}_n(\vec{r}) - R_n(r) + G_n(r) = \frac{\partial n(r)}{\partial t}, \tag{3.9}$$

$$\frac{1}{q}\nabla \cdot \vec{J}_p(\vec{r}) + R_p(r) - G_p(r) = -\frac{\partial p(r)}{\partial t}, \tag{3.10}$$

where $G_n(r)$ and $R_n(r)$ are the generation rates and recombination rates for electrons, and $G_p(r)$ and $R_p(r)$ are the generation rates and recombination rates for holes, respectively.

The Auger recombination rate is given by

$$R_{Aug}(r) = [C_n n(r) + C_p p(r)][n(r)p(r) - n_0(r)p_0(r)] \tag{3.11}$$

where C_n and C_p are Auger coefficients, and $n_0(r)$ and $p_0(r)$ are the equilibrium electron and hole concentration.

The mobility of electrons and holes is expressed as a function of carrier density n

$$\mu(n) = \mu_{min} + \frac{\mu_{max} - \mu_{min}}{1 + (n/N_{ref})^{\alpha}}, \tag{3.12}$$

where μ_{min}, μ_{max}, N_{ref}, and α are fitting parameters according to the experimental mobility measurements.

3.4.2 Simulated micro-LED efficiency

The effects of current crowding and sidewall defects on the size-dependent efficiency and efficiency droop of micro-LEDs are simulated by using the *APSYS* programme. In this simulation, the LED structure on a 100 μm sapphire substrate is constituted by a 3 μm n-GaN layer (doping: 5×10^{18} cm^{-3}), five $In_{0.15}Ga_{0.85}N$ (3 nm)/GaN (10 nm) MQWs, a p-type 20 nm $Al_{0.07}Ga_{0.93}N$ (doping: 3×10^{17} cm^{-3}) and a 150 nm p-type GaN layer (doping: 1.2×10^{18} cm^{-3}). Considering the sidewall defects SRH recombination as shown in sample A and the variation of current density within micro-LEDs, a 2D model was established for the simulation. The SRH recombination lifetime (τ_{SRH}), which directly governs the SRH recombination, is set as 8 ns, 7 ns and 3 ns for 105 μm, 50 μm and 30 μm micro-LEDs, respectively, based on previous fits to frequency response data from similar micro-LEDs as shown in figure 3.6 [23]. η_{IQE} simulation is done for relatively large micro-LEDs $\geq$30 μm which have similar η_{EXE} rather than the 6 μm micro-LED, and thus the simulated η_{IQE} characteristics of the micro-LEDs are comparable with the measured η_{EQE} shown in figure 3.10(b). As the current crowding is more significant at higher injection current densities, to show the advantages of smaller micro-LEDs at extremely high injection current density the η_{IQE} values of micro-LEDs were calculated at injection current densities up to 10 kA/cm^2. It is known that experimentally the large micro-LEDs with sizes 105 μm cannot sustain 10 kA/cm^2 but 6 μm micro-LEDs can sustain such a high current density [11], so the simulation up to 10 kA/cm^2 is to theoretically demonstrate the possible carrier recombination mechanisms at extremely high current densities, especially in case that the current crowding effect will become more serious at a higher current density [10].

As shown in figure 3.13(a), the simulated η_{IQE} characteristics of micro-LEDs have the same variation trend as the experimental results shown in figure 3.10(b), i.e. the smaller micro-LEDs have a lower efficiency at low injection current density but a higher efficiency at high injection current density compared with larger micro-LEDs. Figure 3.13(b) and (c) show calculated carrier concentration distributions within an individual QW at injection current densities of 1 kA/cm^2 and 10 kA/cm^2, respectively. Here the selected QW is that next to the p-GaN layer, and this QW contains the highest hole concentration in our simulations, consistent with experimental results from others [32]. At 1 kA/cm^2 (figure 3.13(b)), the overall hole concentration is over two orders of magnitude lower than

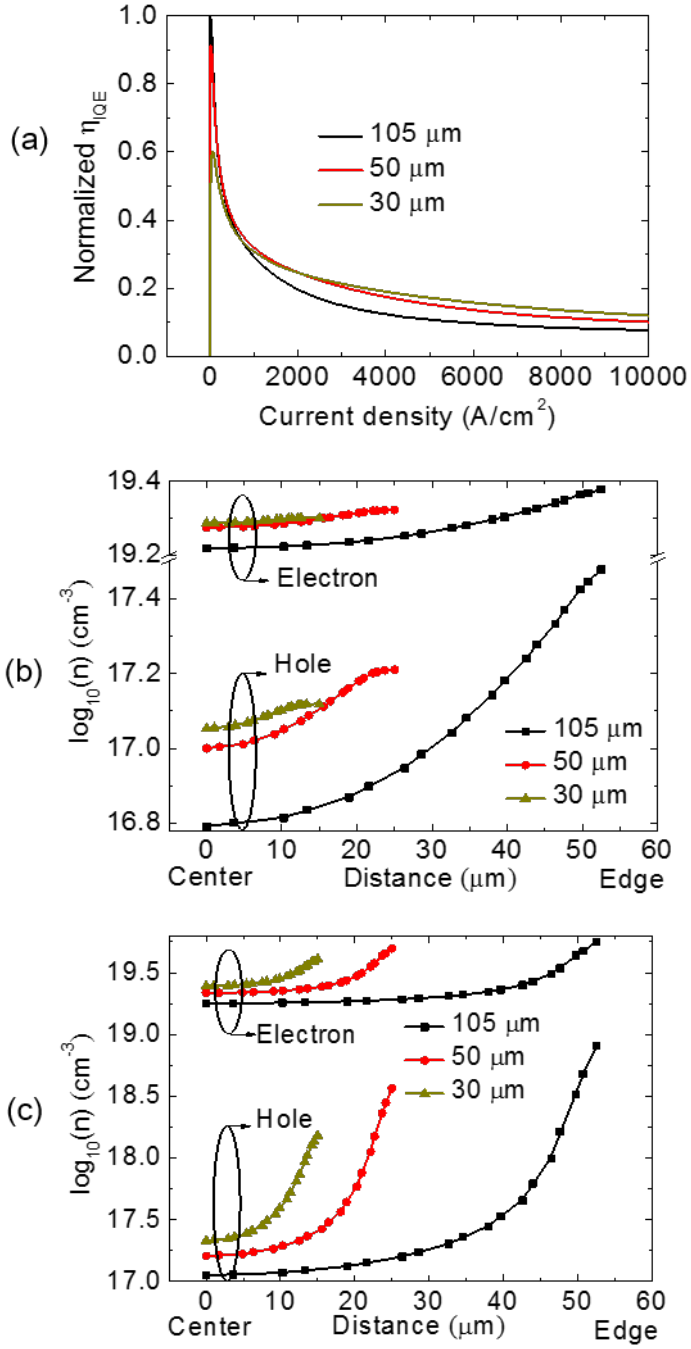

FIGURE 3.13: (a) Simulated size-dependent characteristics of η_{IQE} versus injection current density, and distributions of electron concentration and hole concentration along the in-plane direction of a quantum well (QW) from mesa centre to mesa edge for micro-LEDs with different sizes at injection current densities (b)1 kA/cm^2 and (c)10 kA/cm^2. Here, the selected QW is nearest to the *p*-GaN layer.

the electron concentration, indicating electron leakage probably exists in all micro-LEDs. It is found that the differences between the electron concentration on the edge and in the centre for a 105 μm micro-LED and a 30 μm micro-LED are 7.3×10^{18} cm^{-3} and 6.1×10^{17} cm^{-3}, respectively, while the differences between the hole concentration on the edge and in the center for 105 μm micro-LED and 30 μm micro-LED are 2.4×10^{17} cm^{-3} and 1.8×10^{16} cm^{-3}, respectively. Thus, the electron leakage is highest at the edge and lowest in the centre for the 105 μm micro-LED, but is relatively uniform for the 30 μm micro-LED. Moreover, when injection current density increases gradually to 10 kA/cm^2, the carrier concentration distribution becomes more and more nonuniform especially for the 105 μm micro-LED as shown in figure 3.13(c). The nonuniformity of the in-plane hole and electron concentration distribution confirms a significant current crowding in larger micro-LEDs especially at a high injection current. Relatively high local carrier concentration on the micro-LED edge enhances Auger recombination as well as other non-radiative recombinations, causing local overheating and then catastrophic device degradation. The small 30 μm micro-LED demonstrates much more uniform in-plane hole and electron concentration distributions, which explains why the smaller micro-LEDs can sustain a higher injection current density. In conclusion, these simulations of in-plane carrier concentrations in the active regions of micro-LEDs give insight into how current crowding can simultaneously enhance local non-radiative recombination, heating and electron leakage, all leading to relatively lower efficiency in larger LEDs at high injection current density.

3.5 Summary

In summary, size-dependent efficiency and efficiency droop of micro-LEDs have been investigated. Our results show that at low injection current densities, the efficiency of smaller micro-LEDs reduces significantly via the non-radiative recombination induced by sidewall defects. At higher injection current densities, the efficiency of smaller micro-LEDs becomes higher and the current crowding effect dominates. The sidewall defects can be partially recovered by increasing the thermal annealing time so as to improve the efficiency at low injection current density. At high injection current density, higher LEDs efficiency can be achieved with smaller LED sizes or more uniform current spreading. These results provide not only the insight into the mechanisms of efficiency and efficiency

droop but also propose new avenues to improve LED efficiency and alleviate the efficiency droop problem.

References

[1] J. Piprek. Efficiency droop in nitride-based light-emitting diodes. *Physica Status Solidi (a)*, 207(10):2217–2225, 2010.

[2] Y. C. Shen, G. O. Mueller, S. Watanabe, N. F. Gardner, A. Munkholm, and M. R. Krames. Auger recombination in InGaN measured by photoluminescence. *Applied Physics Letters*, 91(14):141101, 2007.

[3] J. Iveland, L. Martinelli, J. Peretti, J. S. Speck, and C. Weisbuch. Direct measurement of Auger electrons emitted from a semiconductor light-emitting diode under electrical injection: identification of the dominant mechanism for efficiency droop. *Physical Review Letters*, 110 (17):177406, 2013.

[4] S. F. Chichibu, A. Uedono, T. Onuma, B. A. Haskell, A. Chakraborty, T. Koyama, P. T. Fini, S. Keller, S. P. Denbaars, J. S. Speck, U. K. Mishra, S. Nakamura, S. Yamaguchi, S. Kamiyama, H. Amano, I. Akasaki, J. Han, and T. Sota. Origin of defect-insensitive emission probability in In-containing (Al, In, Ga) N alloy semiconductors. *Nature Materials*, 5(10):810–816, 2006.

[5] J. Hader, J. V. Moloney, and S. W. Koch. Density-activated defect recombination as a possible explanation for the efficiency droop in GaN-based diodes. *Applied Physics Letters*, 96(22):221106, 2010.

[6] J. Cho, E. F. Schubert, and J. K. Kim. Efficiency droop in light-emitting diodes: challenges and countermeasures. *Laser & Photonics Reviews*, 7(3):408–421, 2013.

[7] V. K. Malyutenko, S. S. Bolgov, and A. D. Podoltsev. Current crowding effect on the ideality factor and efficiency droop in blue lateral InGaN/GaN light emitting diodes. *Applied Physics Letters*, 97(25):251110, 2010.

[8] Y. Y. Kudryk and A. V. Zinovchuk. Efficiency droop in InGaN/GaN multiple quantum well light-emitting diodes with nonuniform current spreading. *Semiconductor Science and Technology*, 26(9):095007, 2011.

[9] Y. Y. Kudryk, A. K. Tkachenko, and A. V. Zinovchuk. Temperature-dependent efficiency droop in InGaN-based light-emitting diodes induced by current crowding. *Semiconductor Science and Technology*, 27(5):055013, 2012.

[10] H.-Y. Ryu and J.-I. Shim. Effect of current spreading on the efficiency droop of InGaN light-emitting diodes. *Optics Express*, 19(4):2886–2894, 2011.

[11] Z. Gong, S. Jin, Y. Chen, J. McKendry, D. Massoubre, I. M. Watson, E. Gu, and M. D. Dawson. Size-dependent light output, spectral shift, and self-heating of 400 nm InGaN light-emitting diodes. *Journal of Applied Physics*, 107(1):013103, 2010.

[12] T. I. Kim, Y. H. Jung, J. Song, D. Kim, Y. Li, H. S. Kim, I. S. Song, J. J. Wierer, H. A. Pao, Y. Huang, and J. A. Rogers. High-efficiency, microscale GaN light-emitting diodes and their thermal properties on unusual substrates. *Small*, 8(11):1643–9, 2012.

[13] L. Dai, B. Zhang, J. Y. Lin, and H. X. Jiang. Comparison of optical transitions in InGaN quantum well structures and microdisks. *Journal of Applied Physics*, 89(9):4951–4954, 2001.

[14] H. W. Choi, C. W. Jeon, M. D. Dawson, P. R. Edwards, R. W. Martin, and S. Tripathy. Mechanism of enhanced light output efficiency in InGaN-based microlight emitting diodes. *Journal of Applied Physics*, 93(10):5978–5982, 2003.

[15] S. X. Jin, J. Li, J. Y. Lin, and H. X. Jiang. InGaN/GaN quantum well interconnected microdisk light emitting diodes. *Applied Physics Letters*, 77(20):3236–3238, 2000.

[16] D. S. Meyaard, Q. Shan, J. Cho, E. F. Schubert, S.-H. Han, M.-H. Kim, C. Sone, S. J. Oh, and J. K. Kim. Temperature dependent efficiency droop in GaInN light-emitting diodes with different current densities. *Applied Physics Letters*, 100(8):081106, 2012.

[17] X. Guo and E. F. Schubert. Current crowding in GaN/InGaN light emitting diodes on insulating substrates. *Journal of Applied Physics*, 90(8):4191–4195, 2001.

[18] N. L. Ploch, H. Rodriguez, C. Stölmacker, M. Hoppe, M. Lapeyrade, J. Stellmach, F. Mehnke, T. Wernicke, A. Knauer, V. Kueller, M. Weyers, S. Einfeldt, and M. Kneissl. Effective thermal management in ultraviolet light-emitting diodes with micro-LED arrays. *IEEE Transactions on Electron Devices*, 60(2):782–786, 2013.

[19] S. Hwang, M. Islam, B. Zhang, M. Lachab, J. Dion, A. Heidari, H. Nazir, V. Adivarahan, and A. Khan. A hybrid micro-pixel based deep ultraviolet light-emitting diode lamp. *Applied Physics Express*, 4(1):012102, 2011.

[20] V. Adivarahan, S. Wu, W. H. Sun, V. Mandavilli, M. S. Shatalov, G. Simin, J. W. Yang, H. P. Maruska, and M. A. Khan. High-power deep ultraviolet light-emitting diodes based on a micro-pixel design. *Applied Physics Letters*, 85(10):1838–1840, 2004.

[21] J. Cho, C. Sone, Y. Park, and E. Yoon. Measuring the junction temperature of III-nitride light emitting diodes using electro-luminescence shift. *Physica Status Solidi (a)*, 202(9): 1869–1873, 2005.

[22] Y. Yang and X. A. Cao. Removing plasma-induced sidewall damage in GaN-based light-emitting diodes by annealing and wet chemical treatments. *Journal of Vacuum Science & Technology B: Microelectronics and Nanometer Structures*, 27(6):2337–2341, 2009.

[23] R. P. Green, J. J. D. McKendry, D. Massoubre, E. Gu, M. D. Dawson, and A. E. Kelly. Modulation bandwidth studies of recombination processes in blue and green InGaN quantum well micro-light-emitting diodes. *Applied Physics Letters*, 102(9):091103, 2013.

[24] C. Shen, T. K. Ng, C. H. Kang, and B. S. Ooi. Mesa-height dependent quantum efficiency characteristics of InGaN micro-LEDs. *Asia Communications and Photonics Conference*, pages AW3K–3, 2013.

[25] H. Kim, J. Cho, J. W. Lee, S. Yoon, H. Kim, C. Sone, Y. Park, and T.-Y. Seong. Measurements of current spreading length and design of GaN-based light emitting diodes. *Applied Physics Letters*, 90(6):063510, 2007.

[26] Z. Gong, H. X. Zhang, E. Gu, C. Griffin, M. D. Dawson, V. Poher, G. Kennedy, P. M. W. French, and M. A. A. Neil. Matrix-addressable micropixellated InGaN light-emitting diodes with uniform emission and increased light output. *IEEE Transactions on Electron Devices*, 54(10):2650–2658, 2007.

[27] U. Kaufmann, M. Kunzer, M. Maier, H. Obloh, A. Ramakrishnan, B. Santic, and P. Schlotter. Nature of the 2.8 eV photoluminescence band in Mg doped GaN. *Applied Physics Letters*, 72(11):1326–1328, 1998.

[28] L. Hirsch and A.-S. Barriere. Electrical characterization of InGaN/GaN light emitting diodes grown by molecular beam epitaxy. *Journal of Applied Physics*, 94(8):5014–5020, 2003.

[29] J.-R. Chen, Y.-C. Wu, S.-C. Ling, T.-S. Ko, T.-C. Lu, H.-C. Kuo, Y.-K. Kuo, and S.-C. Wang. Investigation of wavelength-dependent efficiency droop in InGaN light-emitting diodes. *Applied Physics B*, 98(4):779–789, 2010.

[30] Z.-M. Li, K. M. Dzurko, A. Delage, and S. P. McAlister. A self-consistent two-dimensional model of quantum-well semiconductor lasers: optimization of a GRIN-SCH SQW laser structure. *IEEE Journal of Quantum Electronics*, 28(4):792–803, 1992.

[31] Z.-M. Li, M. Dion, Y. Zou, J. Wang, M. Davies, and S. P. McAlister. An approximate k· p theory for optical gain of strained InGaAsP quantum-well lasers. *IEEE Journal of Quantum Electronics*, 30(2):538–546, 1994.

[32] A. David, M. J. Grundmann, J. F. Kaeding, N. F. Gardner, T. G. Mihopoulos, and M. R. Krames. Carrier distribution in (0001) InGaN/ GaN multiple quantum well light-emitting diodes. *Applied Physics Letters*, 92(5):053502, 2008.

Chapter 4

Temperature-dependent efficiency droop of blue InGaN micro-LEDs

The wide applications of LEDs require stable LED efficiency in an environment with large temperature variation. However, the efficiency of GaN-based LED changes significantly with temperatures and a consensus on the related mechanisms has not yet been achieved. In addition, the temperature-dependent efficiency droop research can provide clues to the mechanisms of efficiency droop at high current density. The first section in this chapter introduces the previous research on temperature-dependent efficiency droop. In the following sections, the experimental results and analysis of temperature-dependent carrier recombination of blue micro-LEDs are presented. First, the temperature-dependent external quantum efficiency (η_{EQE}) and bandwidth of a blue micro-LED with a diameter of 40 μm are obtained from 300 K to 500 K. To analyse the carrier recombination, we assume no electron leakage and constant light extraction efficiency at all current densities and temperatures. Then, bandwidth/differential lifetime is employed to calculate the carrier concentration (n) in the quantum wells (QWs). The defect-related Shockley-Read-Hall (SRH) recombination coefficient A, radiative recombination coefficient B, Auger recombination coefficient C, and light extraction efficiency (η_{EXE}) are fitted through an ABC model. The ABC model has been discussed by equation 1.14 in Chapter 1. Then, the temperature-dependent n, A, B and C are extracted to clarify the carrier recombination dynamics. These results show that the defect recombination coefficient roughly increases with increasing temperature; the radiative and Auger recombination coefficients decrease with increasing temperature. In addition, at a higher injection carrier concentration, the

temperature dependence of radiative and Auger recombination coefficients is weaker due to the phase space filling effect.

4.1 Overview of temperature-dependent efficiency droop

In some LED applications, such as automotive headlights, the ambient temperatures can be about 90 °C and thus a study of temperature dependence of LED efficiency is necessary. At low current densities, a huge reduction of η_{EQE} peaks by about 30% has been found from 300 K to 450 K [1]. At a fixed high current density, several groups have reported that the η_{EQE} first increases and then decreases with increasing temperature [2–8]. Such η_{EQE} variation largely depends on the LED design [2, 3, 5, 6].

Different mechanisms have been proposed to explain the temperature dependence of efficiency droop, which is correlated with the current-dependent efficiency droop. The mechanisms of droop at high current densities are mainly attributed to the decrease of radiative recombination, and the increases of Auger recombination, electron leakage, and carrier delocalization [9]. This section gives an overview of temperature-dependent efficiency droop research.

4.1.1 Temperature-dependent carrier recombination

Temperature-dependent carrier recombination has been investigated experimentally. The variation of carrier recombination coefficients with temperature is generally estimated by fitting the temperature-dependent internal quantum efficiency (η_{IQE}) curves by an ABC model without considering the electron leakage. One experimental result showed that the Auger recombination coefficient strongly depended on temperature in the range less than 200 K and varied slightly with temperature at temperature larger than 200 K [7]. Another paper found that, based on a simple ABC model, the fitted Auger recombination coefficient strongly decreased with increasing temperature [10]. Recently, Galler et al. found the B coefficients roughly followed $B(T) \propto T^{-1}$ and $C(T)$ increased monotonically with increasing temperatures [11]. These studies all assumed that B and C coefficients are constants for different current densities, but showed different coefficient variation trends with temperature.

Regarding the theoretical calculation of the temperature dependence of radiative and Auger recombination coefficients, it has been reported that the radiative recombination coefficient decreases and the Auger coefficient increases with increasing temperature based on the indirect Auger transition in InGaN material [12–14]. However, for direct Auger recombination, the Auger loss can decrease with temperature in certain cases, e.g. QWs with weak carrier confinement as shown in reference [15]. Up to now, a consensus is lacking on the temperature dependence of the Auger recombination coefficients.

4.1.2 Temperature-dependent electron leakage

Strong electron leakage has been claimed at very low temperatures [2, 5]. Figure 4.1(a) shows the temperature-dependent η_{IQE} of a blue LED with a size of 350×430 μm^2 from 50 K to 300 K. The maximum η_{IQE} at 50 K was defined to be 100%. As temperature is lowered from 300 K to 200 K, the η_{IQE} curves shift slightly to higher values with similar current-dependent efficiency droop. However, from 200 K to 50 K, the shape of η_{IQE} curves changes with pronounced current-dependent efficiency droop. To explain this phenomenon, the electroluminescence (EL) spectra at 10 mA were measured as shown in figure 4.1(b). A side peak around 400 nm grows when reducing temperature from 150 K to 50 K, which originates from the Mg acceptor related transition in p-GaN. At low temperature, the hole transport becomes difficult and the number of holes transported to QWs become smaller, reducing the radiative recombination rate. Recently, Meyaard et al. developed an electron drift model to explain electron leakage [4]. They found a voltage relation of the onset of high injection and the onset of the efficiency droop, correlated by the equation $V_{\text{(high injection onset)}}+\Delta V \approx V_{\text{(droop onset)}}$ at different temperatures. The high injection condition is achieved when the transition of I-V characteristics changes from the exponential to the linear regime. The excess voltage ΔV is determined to be 0.3 V. The resulting electric field sweeps electrons out of the active region and results in electron leakage. Assuming no Auger recombination, the temperature-dependent electron leakage has been calculated [16]. However, given the reported large Auger coefficient [6, 12], the contribution of electron leakage to efficiency droop under different temperatures needs to be further investigated.

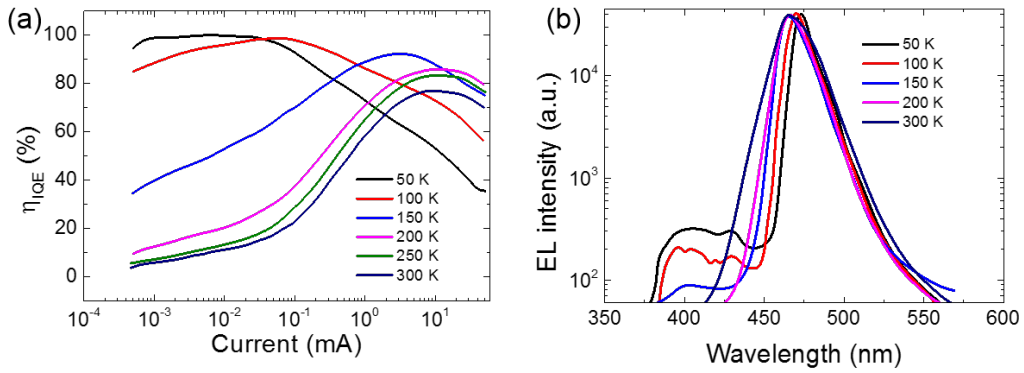

FIGURE 4.1: (a)η_{IQE} versus current and (b)EL spectra at 10 mA for a blue LED under different temperatures. Reproduced from data in [5].

4.1.3 This work

InGaN LEDs suffer from efficiency droop at high current density which is a large barrier for their wide applications in general lighting. Besides, the LEDs may operate at varied temperatures instead of room temperature, and the efficiency of LEDs also varies with different ambient temperatures. Thus, the mechanisms of efficiency droop at high current densities and at different temperatures have been widely investigated but are still under debate. Auger recombination contributes significantly to efficiency droop based on experimental measurements and theoretical analyses [12, 14, 17, 18]. However, a consensus on how the Auger coefficient changes with temperature has not been achieved. In addition, theoretical work has indicated that the temperature dependence of B and C coefficients varies at different current densities [15], however, up to now, the corresponding experimental work has not been reported. In this study, by using micro-LEDs, we further investigated the temperature-dependent Auger coefficient, as well as the defect and radiative recombination coefficients. The temperature dependence of radiative and Auger recombination coefficients at different injection carrier concentrations is also analysed.

4.2 Experimental details

Device fabrication

Individually addressable top-emission micro-LEDs on sapphire substrates with emission wavelength ~445 nm were fabricated from a commercial LED wafer. The commercial

wafer consists of an n-GaN layer, InGaN/GaN multiple quantum wells (MQWs), an AlGaN layer and a p-GaN layer. To fabricate the micro-LED device, Ni/Au layers were first deposited on the p-GaN surface. Then, reactive ion etching and inductively coupled plasma etching were employed to etch the Ni/Au and p-GaN down to n-GaN, respectively, to form the micro-LED mesas. To achieve good ohmic contact and current spreading, the Ni/Au on top of the mesa was rapidly annealed in a purified air condition. A SiO_2 layer was further deposited and patterned as the isolation layer between p- and n-pads, after which Ti/Au layers were deposited and p- and n-pads were fabricated. Figure 4.2(a) and (b) show the schematic structure and microscopic image of the micro-LEDs, respectively. Micro-LEDs with different sizes, e.g. 40 μm and 100 μm in diameter, have been fabricated as shown in figure 4.2(b).

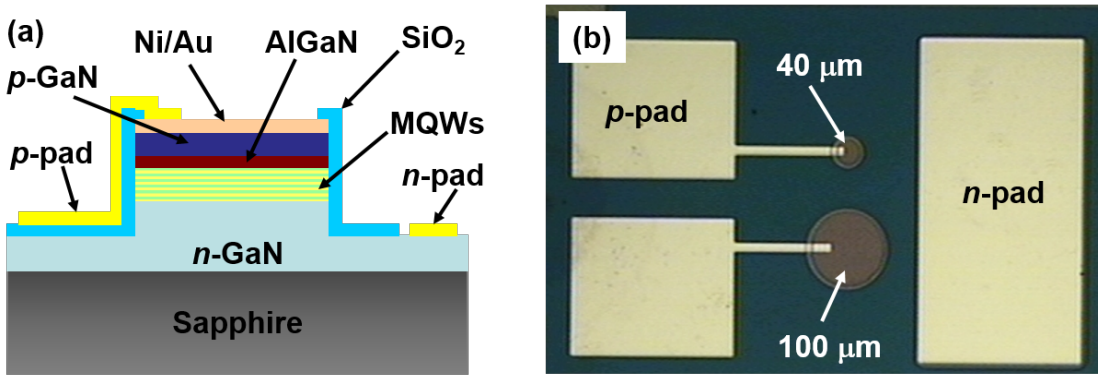

FIGURE 4.2: (a)Schematic structure and (b)microscopic image of the fabricated micro-LEDs. The 40 μm micro-LED is used in this work.

Self heating effect estimation

The micro-LED with a size of 40 μm in diameter was chosen in this work to minimize the self heating effect, benefiting strongly on the temperature-dependent efficiency droop study. As the micro-LEDs have superior current spreading and heat dissipation properties, they can be operated under a high direct current (DC) with little self heating effect [19–21]. It has been found that the current spreading could be also affected by temperature, leading to strong effect on efficiency droop [22]. As the current spreading in micro-LEDs is more uniform than in broad-area LEDs, it is expected that the increase of ambient temperature has much smaller influence on the current spreading in micro-LEDs.

A previous study on micro-LEDs of comparable design shows the junction temperature of a 40 μm micro-LED differs insignificantly from the ambient temperature even under

high DC injection. To estimate the self heating effect of the micro-LED in this work, the light output power of the 40 μm LED was measured under pulsed current (pulse width: 25 μs; pulse period: 525 μs) and DC operations, respectively. Figure 4.3 shows that the two curves of light output power agree with each other very well until the current density $\sim$4 kA/cm^2 ($\sim$50 mA), after which a significant difference between them can be found. Also, for a 40 μm micro-LED from reference [19], the junction temperature shows little change until current density 2800 A/cm^2 ($\sim$35 mA). Thus, in this work, all the data were measured up to DC 35 mA and the self heating effect can be assumed negligible.

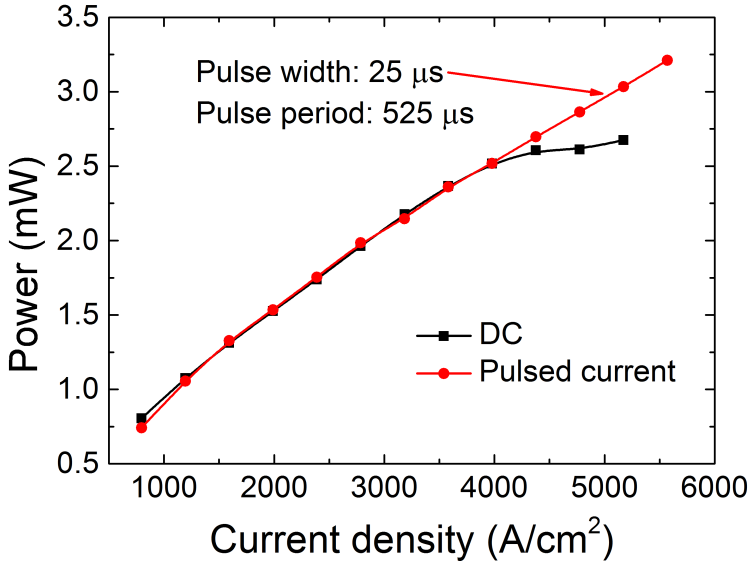

FIGURE 4.3: Light output power of a 40 μm micro-LED under pulsed current (pulse width: 25 μs; pulse period: 525 μs) and DC to estimate the self heating effect. The micro-LED was measured in an integrating sphere at room temperature.

Measurements of temperature-dependent bandwidth and light output power

To carry out the temperature-dependent measurements, the ambient temperature of the micro-LED was controlled by placing the device on a hotplate and the device temperature was calibrated by adhering a type-E thermocouple on the device. To measure the optical -3 dB modulation bandwidth, the micro-LED was DC biased by a power supply and modulated with a small fixed amplitude (RF power: -6 dBm) from an HP8753ES network analyser using a bias-tee. Then the light emission from the micro-LED was measured using a 1.4 GHz bandwidth photoreceiver, and the frequency response was recorded by the network analyser. A Si detector was used to measure the light output power and the light output powers under different temperatures were recorded. The relative η_{EQE}

was then calculated by the measured light output power using equation 1.6 in Chapter 1. The light output powers shown in figure 4.3 were measured in an integrating sphere, and were used to calibrate the light output power measured by the Si detector and then evaluate the η_{EXE} at room temperature ($\sim$ 300 K).

4.3 Temperature-dependent η_{EQE} and bandwidth

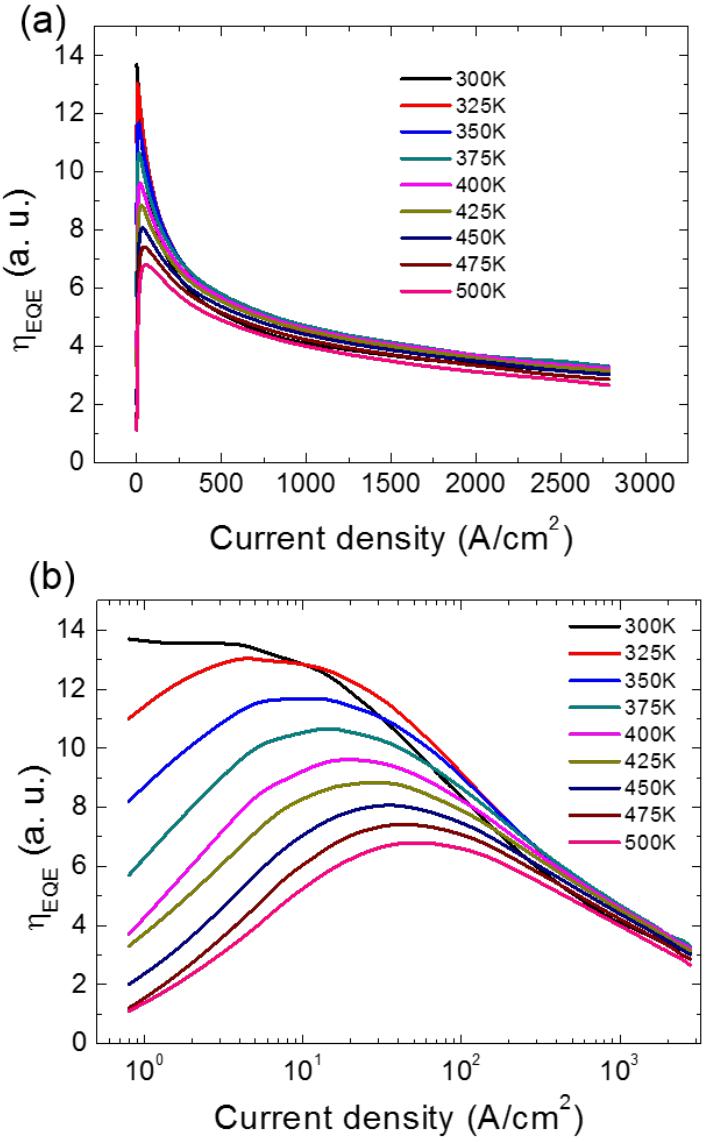

FIGURE 4.4: η_{EQE} versus current density from temperature 300 K to 500 K with 25 K increment in (a)linear scale and (b)semi-log scale.

Figure 4.4(a) and (b) show the temperature-dependent η_{EQE} versus current density characteristics for a 40 μm micro-LED in linear scale and semi-log scale, respectively.

For these measurements, the device temperature was increased from 300 K to 500 K with a 25 K increment. It can be seen that with increasing temperature, the η_{EQE} peak shifts towards higher current densities and the peak η_{EQE} decreases. At low current densities less than 10 A/cm^2, the η_{EQE} keeps dropping with increasing temperature, indicating the increase of defect-related SRH recombination with temperature [16]. At high current densities, the droop is complicated. For example, at 1000 A/cm^2, a close inspection of the data shows that the η_{EQE} increases from 300 K to 375 K and decreases from 375 K to 500 K. The mechanisms of the temperature-dependent η_{EQE} (η_{IQE}) can be explained by an ABC model in the next section.

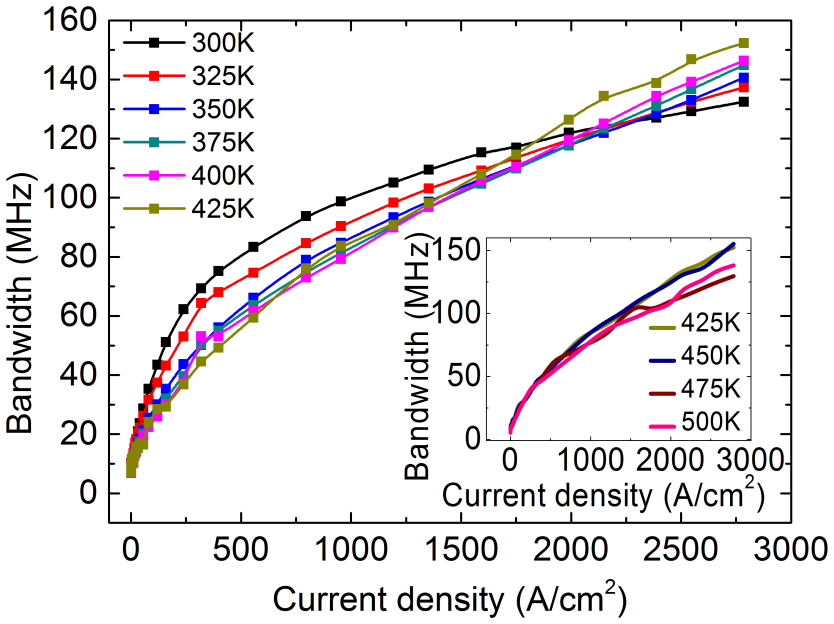

FIGURE 4.5: Bandwidth versus current from temperature 300 K to 425 K to show the trend with temperature. Inset: bandwidth versus current from temperature 425 K to 500 K.

To calculate the carrier concentration in the QWs, bandwidths of micro-LED at different temperatures and different injection current densities were measured and are shown in figure 4.5. In this figure, the bandwidth from 300 K to 425 K demonstrates a clear trend. For example, with increasing temperature, at an injection current density of 500 A/cm^2, the bandwidth decreases, and at an injection current density of 2500 A/cm^2, the bandwidth increases. Comparatively, at high temperatures from 425 K to 500 K, the bandwidth trend shows relatively large fluctuation, as shown in the inset of figure 4.5. The fluctuation probably comes from the noise of the frequency response and then

the fluctuation of the extracted -3dB bandwidth at high temperatures. It should be noted that three groups of data have been obtained for 40 μm micro-LEDs to confirm the temperature-dependent trend of η_{EQE} and bandwidth.

4.4 Methods of fitting carrier recombination

The carrier concentration n can be determined by the equation [11, 23]

$$n = \frac{1}{qV_{active}} \int_0^I \eta_{INJ}(I^{'})\tau(I^{'})dI^{'}, \tag{4.1}$$

where q is the electron charge, V_{active} is the effective volume of active region, I is the current, η_{INJ} is the carrier injection efficiency, and τ is the differential lifetime which can be calculated from the -3dB bandwidth, i.e. $f_{3dB} = \sqrt{3}/2\pi\tau$. It has been reported that the effective volume V_{active} of the active region is reduced due to the inhomogeneous carrier distribution, which comes from carrier localization, strong polarization field within MQWs, insufficient hole transport to the MQWs, and the current crowding effect [24]. Given that the QW next to the p-GaN has the most carrier concentration and recombination, it is commonly accepted to just use one QW volume for efficiency droop study [25–29]. In this work, one QW with thickness 2.8 nm is assumed as the effective active region and this assumption will not affect the temperature-dependent trend of the ABC coefficients. In addition, carrier injection efficiency is assumed as 1 for all temperatures. The electron leakage has little effect at low current densities (roughly before the η_{EQE} peak), but can affect ABC fitting at high current densities (roughly after the η_{EQE} peak) [9, 26]. The latter determined temperature-dependent trend of carrier recombination coefficients is consistent in the whole current density range, so we consider the effect of electron leakage on our results can be neglected.

The η_{EQE} of the micro-LED is expressed by equation

$$\eta_{EQE} = \eta_{EXE} \cdot \eta_{IQE} = \eta_{EXE} \cdot \frac{Bn^2}{An + Bn^2 + Cn^3}, \tag{4.2}$$

where η_{EXE} is the light extraction efficiency. η_{EXE} is assumed as a constant at all current densities and temperatures in this work, and is determined at 300 K. Assuming

the ABC model in equation 4.2 can fully interpret the η_{IQE} curves, the following fitting method will give a fitted η_{EXE}.

In equation 4.2, the B and C coefficients are constants only at low current densities [30–32]. The reason is that the carrier distribution at low current density is approximately described by Maxwell-Boltzmann statistics and at high current density Fermi-Dirac carrier distribution will influence the carrier recombination [30–32]. In addition, radiative recombination requires momentum conservation, and Auger recombination also need conservation of momentum and energy [13]. As a result, with increase of current density, the radiative recombination dependence on n changes from quadratic to linear, and the Auger recombination dependence on n is reduced from cubic to quadratic or even less, the so-called phase space filling effect [30–32]. The B and C coefficients can be roughly expressed by

$$B = \frac{B_0}{1 + n/N^*} \tag{4.3}$$

and

$$C = \frac{C_0}{1 + n/N^*}, \tag{4.4}$$

respectively. Here, N^* is the phase spacing filling parameter, and B_0 and C_0 represent the B and C at very low n, respectively [32]. These parameters could be fitted from the carrier recombination rate. The total carrier recombination rate is expressed as

$$R_{recom} = I/qV_{active}, \tag{4.5}$$

which is the sum of radiative recombination rate

$$R_r = R_{recom}\eta_{IQE} \tag{4.6}$$

and non-radiative recombination rate

$$R_{nr} = R_{recom}(1 - \eta_{IQE}). \tag{4.7}$$

Then, from

$$\frac{R_{nr}}{n} = A + Cn^2, \tag{4.8}$$

A coefficient is obtained at low n (e.g. 1×10^{18} cm^{-3}); from

$$\frac{R_r}{n^2} = B, \tag{4.9}$$

B coefficient is calculated; through

$$\frac{R_{nr}}{n^3} = A/n^2 + C, \tag{4.10}$$

C coefficient can be estimated at a high n (e.g. 2×10^{20} cm^{-3}). After fitting these relations, the recombination coefficients A, B_0, C_0, and phase space filling parameter N^* can be obtained. Finally, using these parameters to fit the η_{EQE} curves obtained from the experimental measurements, the η_{EXE} can be achieved.

The typical fitting results of R_{nr}/n, R_r/n^2, R_{nr}/n^3, and η_{IQE} at 400 K are shown in figure 4.6(a)-(d), respectively. An η_{EXE} value of ∼18% is obtained to fit the η_{IQE}, which is in the correct range of the theoretical η_{EXE} for top-emission micro-LEDs [23, 33]. The obtained coefficient of determination, R^2, indicates that excellent fittings to the experimental data are given. The fitted parameters at 400 K are A=2.00×10^{7} s^{-1}, B_0=4.21×10^{-12} cm^{3}s^{-1}, C_0=1.98×10^{-31} cm^{6}s^{-1}, and N^*=4.39×10^{18} cm^{-3}. We consider that the actual η_{EXE} may deviate slightly from the fitted value. In this case, it is meaningful to estimate the effects on A, B and C caused by the η_{EXE} variation. For example, assuming a large η_{EXE} variation range from 14% to 22% at 400 K, the percentage changes of A, B and C are in the range from -6% to 3%, from 30% to -17% (at n=1×10^{20} cm^{-3}) and from -7% to 4% (at n=1×10^{20} cm^{-3}), respectively. The η_{EXE} variation causes small changes of A and C coefficients, but a relatively large variation of B coefficient [23]. However, it is found that the temperature-dependent trend of A, B and C coefficients will not be affected, so an η_{EXE} value of ∼18% is considered valid in this work. Using the η_{EXE} value of ∼18%, fittings of R_{nr}/n, R_r/n^2, and R_{nr}/n^3 have been done at other temperatures for the comparison of temperature-dependent carrier recombination in next section.

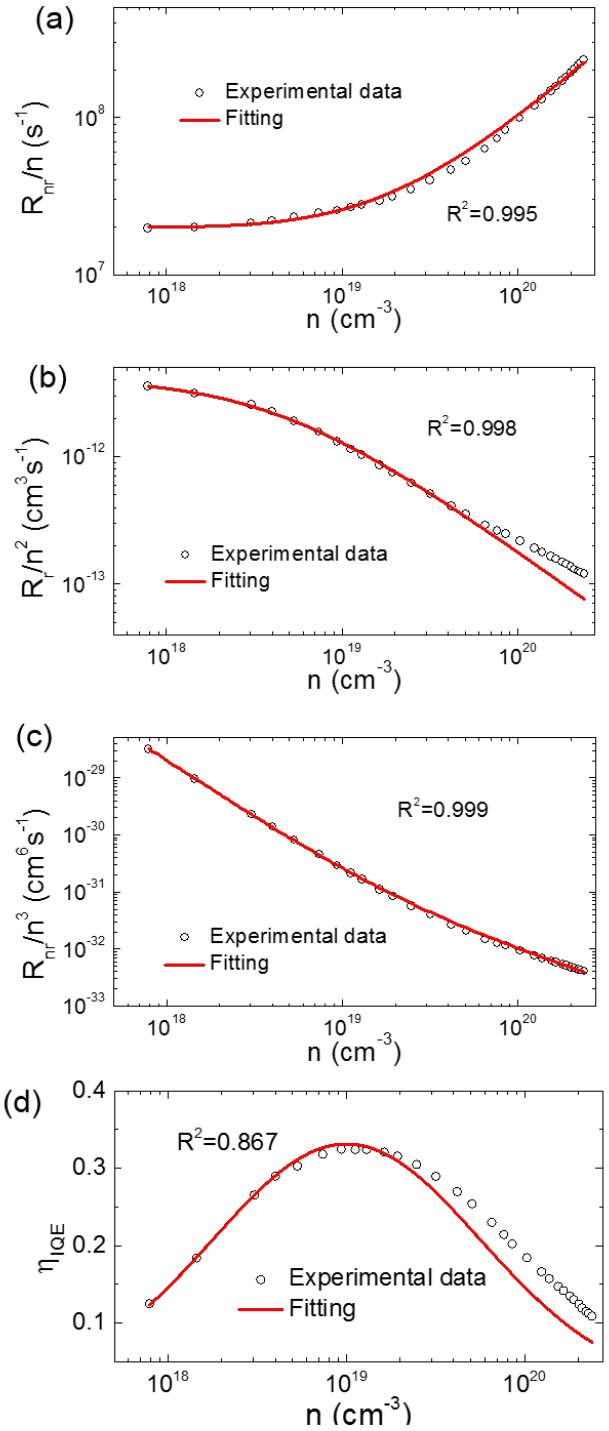

FIGURE 4.6: The fitting and experimental curves of (a)R_{nr}/n, (b) R_r/n^2, (c)R_{nr}/n^3, and (d)η_{IQE} at 400 K. The obtained coefficient of determination, R^2, of each fitting is also given.

4.5 Temperature-dependent carrier recombination

From equation 4.1, the calculated carrier concentrations n at different temperatures are shown in figure 4.7. The n keeps increasing from 300 K to 500 K. This trend is dominated by the carrier generation and recombination, and is consistent with the reduced radiative and Auger recombination coefficients in the following discussions.

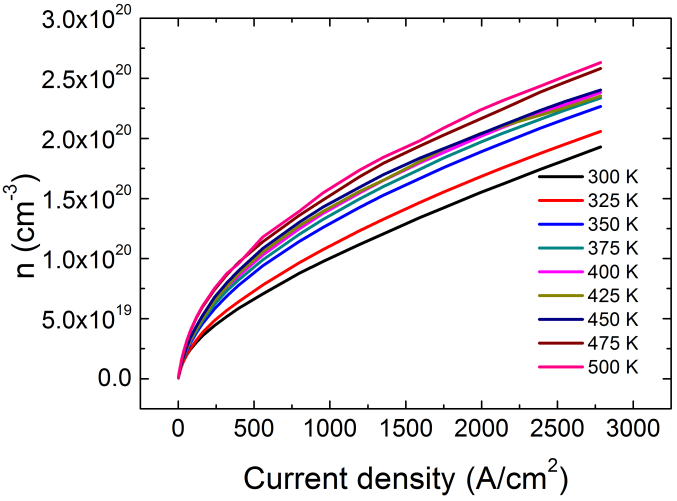

FIGURE 4.7: Carrier concentration n versus current density from temperature 300 K to 500 K.

Knowing the carrier concentration in QWs at different temperatures and the η_{EXE} value of ~18%, R_{nr}/n, R_r/n^2, and R_{nr}/n^3 are calculated from 300 K to 500 K as shown in figure 4.8(a), (b), and (c), respectively. The fitted values of recombination coefficients A, B_0, C_0, and phase space filling parameter N^* are shown in table 4.1. Generally, with increasing temperature, the A coefficient roughly increases, B and C coefficients decrease, and the parameter N^* increases. The mechanisms underlining the fitted parameters are discussed as follows.

From figure 4.8(a), at low carrier concentration, the SRH recombination coefficients show a rough increasing trend with increasing temperature. However, fluctuation still exists which may come from the fluctuation of obtained -3dB bandwidth at a very low current. The possible reasons are the relatively large modulation signal compared to the DC component, as well as the noises of optical frequency response.

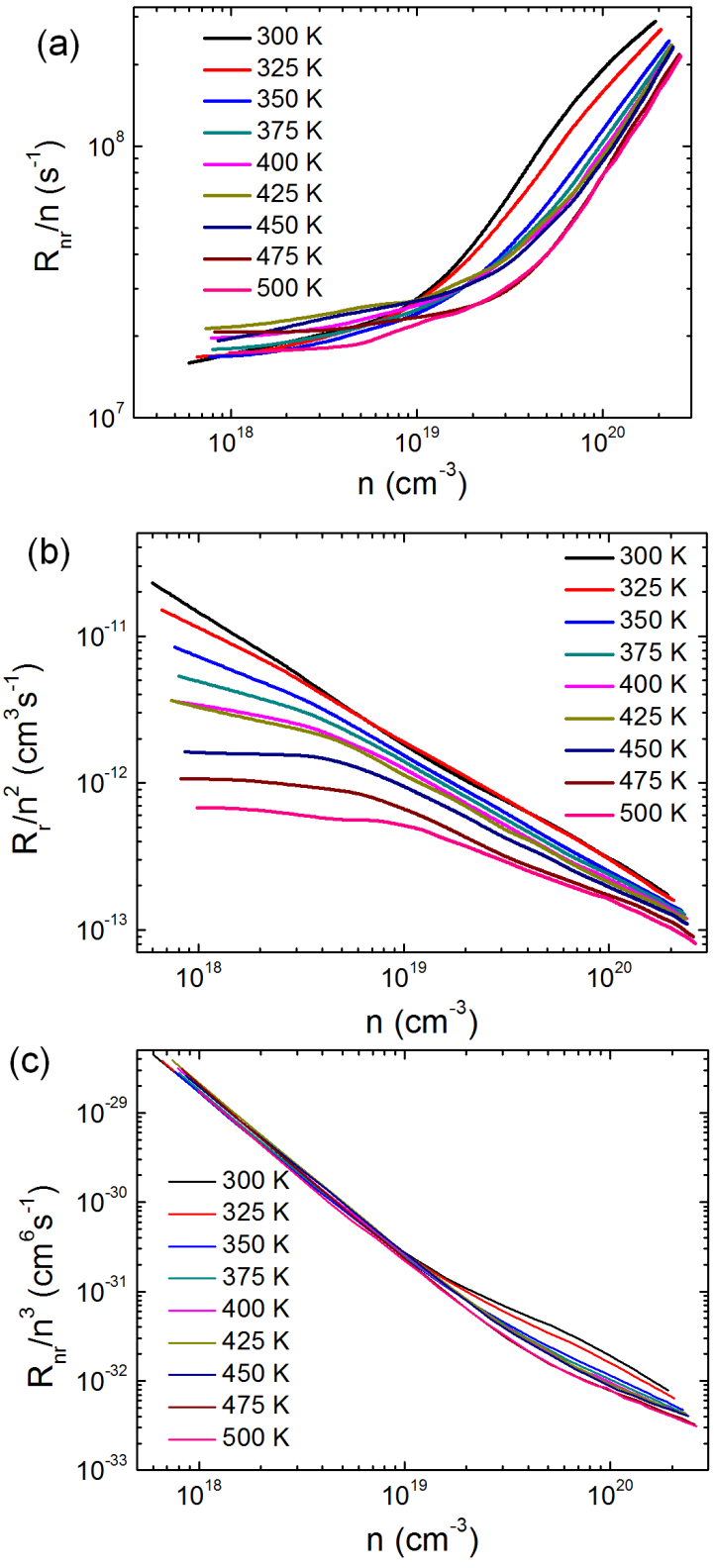

FIGURE 4.8: The experimental curves of (a)R_{nr}/n, (b) R_r/n^2, (c)R_{nr}/n^3 from temperature 300 K to 500 K.

TABLE 4.1: Comparison of fitted A, B_0, C_0, and N^* from temperature 300 K to 500 K.

T (K)	A (s^{-1})	B_0 (cm^3s^{-1})	C_0 (cm^6s^{-1})	N^* (cm^{-3})
300	1.67×10^{7}	1.04×10^{-10}	9.22×10^{-30}	1.68×10^{17}
325	1.70×10^{7}	3.07×10^{-11}	2.11×10^{-30}	6.17×10^{17}
350	1.69×10^{7}	1.30×10^{-11}	7.64×10^{-31}	1.32×10^{18}
375	1.81×10^{7}	6.81×10^{-12}	3.48×10^{-31}	2.65×10^{18}
400	2.00×10^{7}	4.21×10^{-12}	1.98×10^{-31}	4.39×10^{18}
425	2.16×10^{7}	4.15×10^{-12}	2.14×10^{-31}	4.00×10^{18}
450	2.00×10^{7}	1.87×10^{-12}	8.19×10^{-32}	1.06×10^{19}
475	2.07×10^{7}	1.16×10^{-12}	5.63×10^{-32}	1.37×10^{19}
500	1.75×10^{7}	6.88×10^{-13}	3.00×10^{-32}	2.68×10^{19}

It is proposed that the dependence of A coefficient on temperature can be approximately expressed by equation [16, 34]

$$A = \frac{1}{\tau_0[1 + cosh(\frac{E_T - E_{Fi}}{k_B T})]}, \tag{4.11}$$

where E_{Fi} is the intrinsic Fermi level, E_T is the defect trap energy, and τ_0 is a constant that depends on the concentration of traps and carrier capture rate. By using equation 4.11, the experimental data were fitted, as shown in figure 4.9. The fitting yields an $E_T - E_{Fi}$ value of ~0.03 eV, which is of the same order of magnitude as the published value [35].

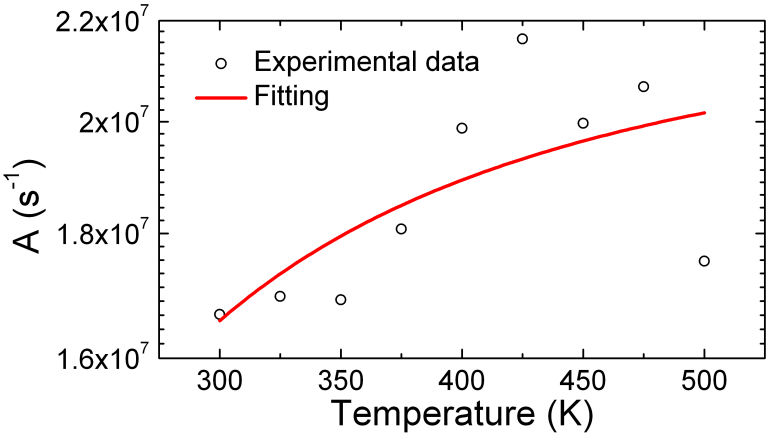

FIGURE 4.9: A coefficient variation with temperature, as fitted by equation 4.11.

In figure 4.8(b), the B coefficient (R_r/n^2) decreases with increasing temperature at all carrier concentrations, caused by the phase space filling effect. The phase space filling parameter N^* increases with increasing temperature as shown in table 4.1, which agrees

with the theoretical and experimental trend demonstrated in other work [13, 22, 31]. This means the phase space filling effect becomes significant at a higher injection level and at a higher temperature [22], because more carriers occupy the states in higher subbands at higher temperatures (the carrier number per d**k** interval in **k**-space decreases with increasing temperature) [15, 34]. The radiative recombination probability of an electron is proportional to the number of holes available at equal momentum, so the radiative recombination probability decreases with increasing temperature.

To show the temperature dependence of the B coefficient, figure 4.10(a) and (b) show B coefficient variation with temperature at n=2×10^{18} cm^{-3} and n=1×10^{20} cm^{-3}, respectively. A strong decrease of B with increasing temperature has been found at low carrier concentration n=2×10^{18} cm^{-3}, i.e. $B \propto T^{-4}$. However, at high carrier concentration n=1×10^{20} cm^{-3}, a weaker temperature dependence of $B \propto T^{-1}$ appears. This

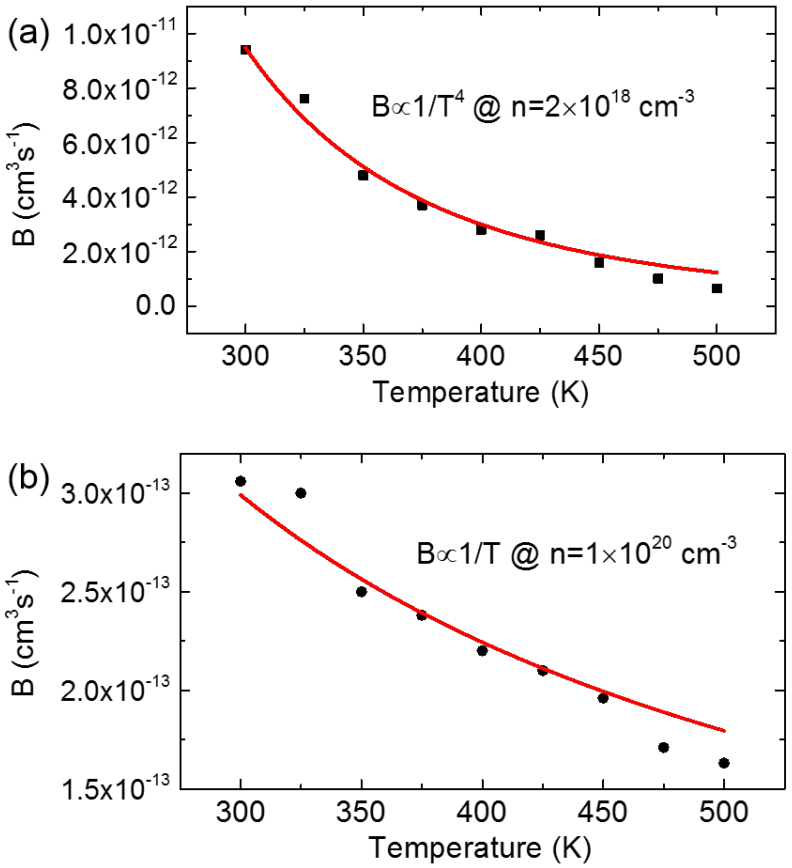

FIGURE 4.10: B coefficient variation with temperature (a)at n=2×10^{18} cm^{-3} ($B \propto T^{-4}$) and (b) at n=1×10^{20} cm^{-3} ($B \propto T^{-1}$). The red line is the fitting to the experimental data (black symbols).

phenomenon agrees with the theoretical calculation very well [15] and is explained as follows. At low injection carrier concentration (2×10^{18} cm^{-3}), a fraction of carriers, close to Fermi level and in the high energy tail of the occupation function, is strongly influenced by temperature; at high carrier concentration (1×10^{20} cm^{-3}), the carrier states close to the bandgap are filled, so most carriers are at energies below Fermi level, leading to less temperature dependence [15]. Other experimental and theoretical work reported weak dependence of B on T [11, 13], which agrees with the results at high current densities in this work.

The temperature-dependent C coefficient as shown in figure 4.11(a) were calculated from the values of C_0 and N^* in table 4.1. At all carrier concentrations, the C coefficient decreases with increasing temperature. In addition, similar to radiative recombination, a weaker dependence on temperature is also obtained at a higher carrier concentration, which is also related to the phase space filling effect. The C dependence on temperature at carrier concentration 1×10^{20} cm^{-3} is shown in figure 4.11(b), i.e. $C \propto T^{-2}$. The

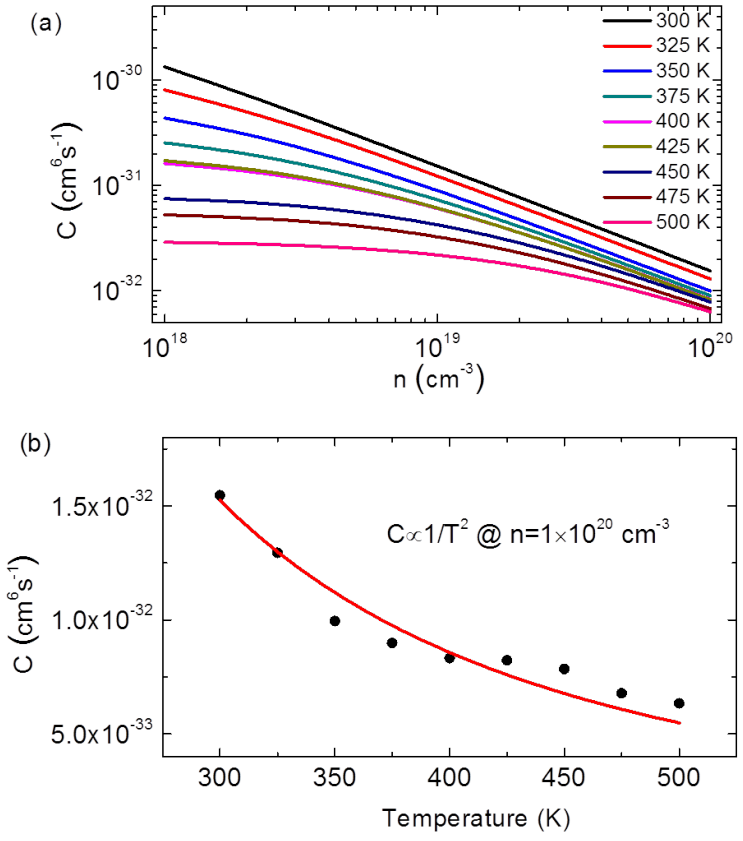

FIGURE 4.11: (a) Calculated C coefficient versus n at different temperatures. (b) C coefficient variation with temperature at n=1×10^{20} cm^{-3} ($C \propto T^{-2}$). The red line is the fitting to the calculated data (black symbols).

temperature dependence of C coefficient in this work is contrary with the most theoretical and experimental results shown in the literature [11, 12, 14]. However, some experimental fitting work indeed gives a strong decrease of C coefficient with increasing T, e.g. $C \propto T^{-3}$ [6], and for certain QW designs the theoretical Auger coefficient can decrease with temperature through a microscopic theory [15]. It has been theoretically analysed that two competing effects are mainly responsible for the temperature dependence of Auger coefficient: phase space filling effect and the bandgap change with temperature [15]. On one hand, at higher temperature, spill over of carriers to higher subbands and barrier states leads to a reduction of Auger coefficient. On the other hand, the bandgap decreases with increasing temperature, causing strong increase of Auger recombination. For the QW design where carrier spill over is dominant, the theoretical value of Auger coefficient decreases with increasing temperature [15]. Also, the dependence of Auger recombination on QW structures is reported by other groups [36, 37]. These mechanisms may explain the reduced Auger coefficient with increasing temperature observed in this work.

4.6 Summary

In summary, temperature-dependent efficiency droop for a micro-LED from 300 K to 500 K has been experimentally analysed through an ABC model. With increasing temperature, the carrier concentration in the QWs increases; the SRH-related defect recombination coefficient roughly increases; the radiative and Auger recombination coefficients decrease. It is also found that the temperature dependence of radiative and Auger recombination coefficients becomes weaker at higher carrier concentrations. The phase space filling effect contributes significantly to the variation of temperature-dependent radiative and Auger recombination coefficients.

This work analyses the temperature-dependent carrier recombination, providing the possible mechanisms which can help future LED design with more thermal stability. Given that the temperature dependence is strongly related to QW design [15], more experimental measurement and theoretical calculation of different QW structures are important to further investigate the temperature dependence of carrier recombinations in the future. Specifically, micro-LEDs can sustain much higher current densities, up to tens of kA/cm^2 [19], than commonly used broad-area LEDs, and thus have more thermal stability when operating at very high current densities in applications.

References

[1] D. S. Meyaard, Q. Shan, J. Cho, E. F. Schubert, S.-H. Han, M.-H. Kim, C. Sone, S. J. Oh, and J. K. Kim. Temperature dependent efficiency droop in GaInN light-emitting diodes with different current densities. *Applied Physics Letters*, 100(8):081106, 2012.

[2] H. Masui, T. Ive, M. C. Schmidt, N. N. Fellows, H. Sato, H. Asamizu, S. Nakamura, and S. P. DenBaars. Equivalent-circuit analysis for the electroluminescence-efficiency problem of InGaN/GaN light-emitting diodes. *Japanese Journal of Applied Physics*, 47(4R):2112, 2008.

[3] C. H. Wang, J. R. Chen, C. H. Chiu, H. C. Kuo, Y.-L. Li, T. C. Lu, and S. C. Wang. Temperature-dependent electroluminescence efficiency in blue InGaN–GaN light-emitting diodes with different well widths. *IEEE Photonics Technology Letters*, 22(4):236–238, 2010.

[4] D. S. Meyaard, G.-B. Lin, J. Cho, E. F. Schubert, H. Shim, S.-H. Han, M.-H. Kim, C. Sone, and Y. S. Kim. Identifying the cause of the efficiency droop in GaInN light-emitting diodes by correlating the onset of high injection with the onset of the efficiency droop. *Applied Physics Letters*, 102(25):251114, 2013.

[5] D.-S. Shin, D.-P. Han, J.-Y. Oh, and J.-I. Shim. Study of droop phenomena in InGaN-based blue and green light-emitting diodes by temperature-dependent electroluminescence. *Applied Physics Letters*, 100(15):153506, 2012.

[6] J. Hader, J. V. Moloney, and S. W. Koch. Temperature-dependence of the internal efficiency droop in GaN-based diodes. *Applied Physics Letters*, 99(18):181127, 2011.

[7] S. Y. Karpov. Effect of localized states on internal quantum efficiency of III-nitride LEDs. *Physica Status Solidi (RRL)-Rapid Research Letters*, 4(11):320–322, 2010.

[8] J. Wang, L. Wang, W. Zhao, Z. Hao, and Y. Luo. Understanding efficiency droop effect in InGaN/GaN multiple-quantum-well blue light-emitting diodes with different degree of carrier localization. *Applied Physics Letters*, 97(20):201112, 2010.

[9] J. Piprek. Efficiency droop in nitride-based light-emitting diodes. *Physica Status Solidi (a)*, 207(10):2217–2225, 2010.

[10] J. Hader, J. V. Moloney, and S. W. Koch. Density-activated defect recombination as a possible explanation for the efficiency droop in GaN-based diodes. *Applied Physics Letters*, 96(22):221106, 2010.

[11] B. Galler, P. Drechsel, R. Monnard, P. Rode, P. Stauss, S. Froehlich, W. Bergbauer, M. Binder, M. Sabathil, B. Hahn, and J. Wagner. Influence of indium content and temperature on Auger-like recombination in InGaN quantum wells grown on (111) silicon substrates. *Applied Physics Letters*, 101(13):131111, 2012.

[12] E. Kioupakis, P. Rinke, K. T. Delaney, and C. G. Van de Walle. Indirect Auger recombination as a cause of efficiency droop in nitride light-emitting diodes. *Applied Physics Letters*, 98(16):161107, 2011.

[13] E. Kioupakis, Q. Yan, D. Steiauf, and C. G. Van de Walle. Temperature and carrier-density dependence of Auger and radiative recombination in nitride optoelectronic devices. *New Journal of Physics*, 15(12):125006, 2013.

[14] F. Bertazzi, M. Goano, and E. Bellotti. Numerical analysis of indirect Auger transitions in InGaN. *Applied Physics Letters*, 101(1):011111, 2012.

[15] J. Hader, J. V. Moloney, and S. W. Koch. Temperature dependence of radiative and Auger losses in quantum wells. *IEEE Journal of Quantum Electronics*, 44(2):185–191, 2008.

[16] D. S. Meyaard, Q. Shan, Q. Dai, J. Cho, E. F. Schubert, M.-H. Kim, and C. Sone. On the temperature dependence of electron leakage from the active region of GaInN/GaN light-emitting diodes. *Applied Physics Letters*, 99(4):041112, 2011.

[17] J. Iveland, L. Martinelli, J. Peretti, J. S. Speck, and C. Weisbuch. Direct measurement of Auger electrons emitted from a semiconductor light-emitting diode under electrical injection: identification of the dominant mechanism for efficiency droop. *Physical Review Letters*, 110 (17):177406, 2013.

[18] M. Binder, A. Nirschl, R. Zeisel, T. Hager, H.-J. Lugauer, M. Sabathil, D. Bougeard, J. Wagner, and B. Galler. Identification of nnp and npp Auger recombination as significant contributor to the efficiency droop in (GaIn) N quantum wells by visualization of hot carriers in photoluminescence. *Applied Physics Letters*, 103(7):071108, 2013.

[19] Z. Gong, S. Jin, Y. Chen, J. McKendry, D. Massoubre, I. M. Watson, E. Gu, and M. D. Dawson. Size-dependent light output, spectral shift, and self-heating of 400 nm InGaN light-emitting diodes. *Journal of Applied Physics*, 107(1):013103, 2010.

[20] P. Tian, J. J. D. McKendry, Z. Gong, B. Guilhabert, I. M. Watson, E. Gu, Z. Chen, G. Zhang, and M. D. Dawson. Size-dependent efficiency and efficiency droop of blue InGaN micro-light emitting diodes. *Applied Physics Letters*, 101(23):231110, 2012.

[21] T. I. Kim, Y. H. Jung, J. Song, D. Kim, Y. Li, H. S. Kim, I. S. Song, J. J. Wierer, H. A. Pao, Y. Huang, and J. A. Rogers. High-efficiency, microscale GaN light-emitting diodes and their thermal properties on unusual substrates. *Small*, 8(11):1643–9, 2012.

[22] Y. Y. Kudryk, A. K. Tkachenko, and A. V. Zinovchuk. Temperature-dependent efficiency droop in InGaN-based light-emitting diodes induced by current crowding. *Semiconductor Science and Technology*, 27(5):055013, 2012.

[23] R. P. Green, J. J. D. McKendry, D. Massoubre, E. Gu, M. D. Dawson, and A. E. Kelly. Modulation bandwidth studies of recombination processes in blue and green InGaN quantum well micro-light-emitting diodes. *Applied Physics Letters*, 102(9):091103, 2013.

[24] H.-Y. Ryu, D.-S. Shin, and J.-I. Shim. Analysis of efficiency droop in nitride light-emitting diodes by the reduced effective volume of InGaN active material. *Applied Physics Letters*, 100(13):131109, 2012.

[25] A. David, M. J. Grundmann, J. F. Kaeding, N. F. Gardner, T. G. Mihopoulos, and M. R. Krames. Carrier distribution in (0001) InGaN/ GaN multiple quantum well light-emitting diodes. *Applied Physics Letters*, 92(5):053502, 2008.

[26] Q. Dai, Q. Shan, J. Cho, E. F. Schubert, M. H. Crawford, D. D. Koleske, M.-H. Kim, and Y. Park. On the symmetry of efficiency-versus-carrier-concentration curves in GaInN/GaN light-emitting diodes and relation to droop-causing mechanisms. *Applied Physics Letters*, 98(3):033506, 2011.

[27] J. H. Zhu, S. M. Zhang, H. Wang, D. G. Zhao, J. J. Zhu, Z. S. Liu, D. S. Jiang, Y. X. Qiu, and H. Yang. The investigation on carrier distribution in InGaN/GaN multiple quantum well layers. *Journal of Applied Physics*, 109(9):093117, 2011.

[28] Y.-K. Kuo, J.-Y. Chang, M.-C. Tsai, and S.-H. Yen. Advantages of blue InGaN multiple-quantum well light-emitting diodes with InGaN barriers. *Applied Physics Letters*, 95(1): 011116, 2009.

[29] A. David and M. J. Grundmann. Influence of polarization fields on carrier lifetime and recombination rates in InGaN-based light-emitting diodes. *Applied Physics Letters*, 97(3): 033501, 2010.

[30] V. A. Smagley, P. G. Eliseev, and M. Osinski. Comparison of models for calculation of optical gain in gallium nitride. *Photonics West'97*, pages 129–140, 1997.

[31] J. Hader, J. V. Moloney, and S. W. Koch. Supression of carrier recombination in semiconductor lasers by phase-space filling. *Applied Physics Letters*, 87(20):201112, 2005.

[32] A. David and M. J. Grundmann. Droop in InGaN light-emitting diodes: a differential carrier lifetime analysis. *Applied Physics Letters*, 96(10):103504, 2010.

[33] T.-X. Lee, K. Gao, W.-T. Chien, and C.-C. Sun. Light extraction analysis of GaN-based light-emitting diodes with surface texture and/or patterned substrate. *Optics Express*, 15 (11):6670–6676, 2007.

[34] E. F. Schubert. *Light emitting diodes*. Second edition, Cambridge University Press, 2006.

[35] H. P. T. Nguyen, M. Djavid, K. Cui, and Z. Mi. Temperature-dependent nonradiative recombination processes in GaN-based nanowire white-light-emitting diodes on silicon. *Nanotechnology*, 23(19):194012, 2012.

[36] R. Vaxenburg, E. Lifshitz, and Al. L. Efros. Suppression of Auger-stimulated efficiency droop in nitride-based light emitting diodes. *Applied Physics Letters*, 102(3):031120, 2013.

[37] Y.-R. Wu, R. Shivaraman, K.-C. Wang, and J. S. Speck. Analyzing the physical properties of InGaN multiple quantum well light emitting diodes from nano scale structure. *Applied Physics Letters*, 101(8):083505, 2012.

Chapter 5

Flexible GaN-based LEDs

Inorganic GaN-based LEDs provide many advantages over organic LEDs, including high carrier mobility and radiative recombination rates, as well as long-term stability and reliability. However, the commonly used rigid substrates for inorganic GaN-based LEDs, such as sapphire, limit their applications in deformable displays, for biomedicine, etc. Recently, flexible GaN-based LEDs have been demonstrated, which combine the flexibility of the soft substrates and high efficiency of GaN-based LEDs, and therefore facilitate the potential applications referred to above. The techniques to transfer the GaN-based LED layers onto flexible substrates include wet etching for LEDs grown on Si substrates [1], laser lift-off (LLO) for LEDs grown on sapphire substrates [2], and mechanical lift-off for LEDs grown on graphene substrates [3]. In this chapter, the fabrication technologies, characteristics and applications of flexible GaN-based LEDs will be firstly reviewed. Then, combining metal bonding/debonding and laser lift-off techniques, an advanced approach for fabricating flexible vertical GaN-based broad-area LEDs (flexible VLEDs) has been developed using only one transfer step. Bonded onto the flexible and highly thermally conductive AuSn substrates, the fabricated flexible VLEDs show uniform light emission even at a substrate bending radius as small as 3.5 mm. It is found that the strain induced by mechanical bending, and strain-induced defects, have strong effects on device performance. By comparing the calculated and measured spectral characteristics of the flexible VLEDs at different bending radii, the strain effects are evaluated quantitatively. It is demonstrated that the systematic blue shift of the electroluminescence (EL) peak with decreasing bending radius is caused by bending-induced strain, which alleviates the quantum-confined Stark (QCSE) effect in the multiple quantum wells (MQWs).

Furthermore, a flexible micro-LED array was fabricated to demonstrate the potential applications in micro-displays and visible light communication (VLC). The measurements show that a typical micro-LED pixel in such a flexible array can achieve a maximum bandwidth ∼40 MHz and a data transmission rate of 120 Mbit/s at 60 mA injection current.

5.1 Overview of flexible GaN-based LEDs

In this section, the fabrication techniques of flexible GaN-based LEDs will be reviewed. These LEDs were initially grown on sapphire, Si and graphene substrates. Then, the external mechanical bending effect on the characteristics of flexible LEDs and the applications of flexible LEDs in solid state lighting, displays and biosensors, etc., will be introduced.

5.1.1 Fabrication techniques

Flexible LEDs fabricated from LEDs grown on Si substrates

Figure 5.1 shows schematic processing steps for flexible GaN-based LEDs by using LEDs grown on Si substrates [1]. The LEDs consist of n-GaN, InGaN MQWs, and p-GaN layers. Using inductively coupled plasma-reactive ion etching (ICP-RIE), LED mesas were first fabricated and an n-contact was then formed. A p-type contact was formed by surface treatment, Ni/Au deposition, and rapid thermal annealing (RTA). Opaque Ti/Au contact pads were deposited for both contact electrodes and mask patterns for self-aligned passivation process. SiN, Ni and GaN LEDs pattern were created for KOH undercut etching, after which transfer printing of LEDs was employed to transfer the LED dies onto flexible polyurethane (PET) films. The transfer printing is an automated printer system which allows arbitrary spreading of LED arrays [4]. After back-side exposure for passivation and metallization of LED interconnection, the fabrication of flexible LEDs arrays was finished.

Flexible LEDs fabricated from LEDs grown on sapphire substrates

The GaN-based LEDs grown on Si substrates are less mature than the state-of-the-art LEDs grown on sapphire substrates, and as such show inferior performance. To

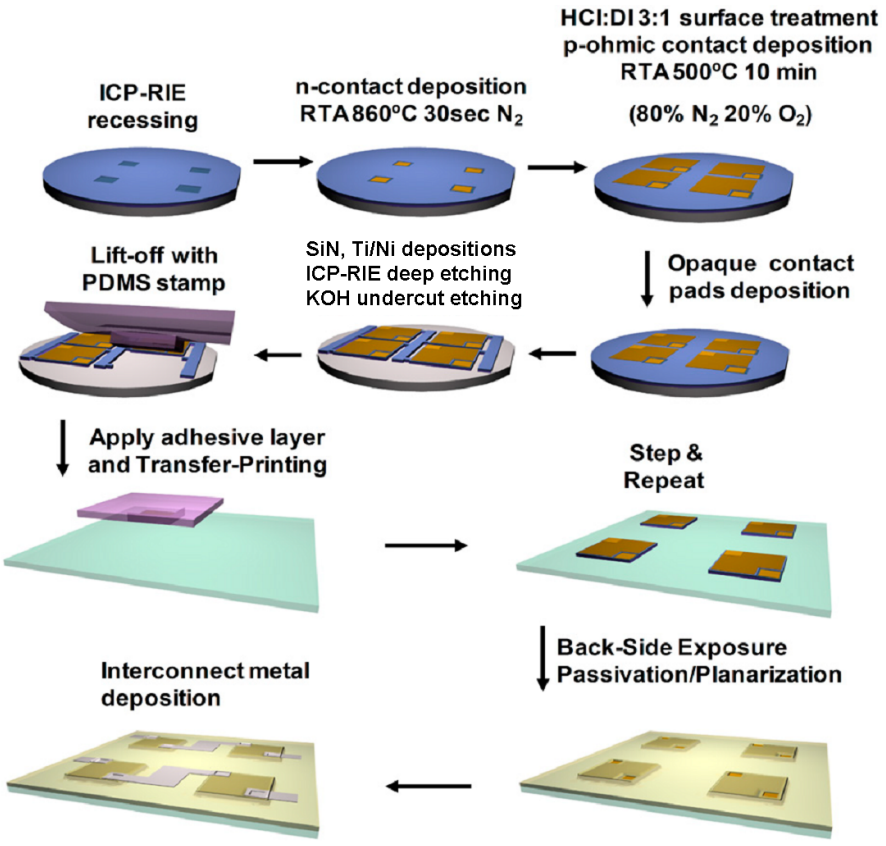

FIGURE 5.1: Schematic processing steps for flexible GaN-based LEDs using LEDs grown on Si substrates. Adapted from [1].

achieve high efficiency flexible LEDs, the technologies to transfer LED epitaxial layers from sapphire substrates to flexible foreign substrates have been developed [2]. First, the LED mesas on sapphire substrates were etched, and then current spreading layer, n-pad and p-pad were formed. After SiN passivation, the LEDs were bonded onto Si substrates through Pd/In bonding. KrF or YAG laser was then used to lift off the sapphire substrates. After LLO, metal undercut etching, transfer printing and metal interconnection were then processed to achieve flexible LEDs, similar to the fabrication steps as shown in figure 5.1.

Flexible LEDs fabricated from LEDs grown on graphene substrates

The above technologies including wet etching and LLO processes to remove the thin LED layers from the original growth substrates are complicated which may limit their applications. Thus, methods of growing GaN-based LEDs on graphene layers and then transferring the LEDs layers to other substrates were developed [3]. The graphene sheets consist of weakly bonded layers of carbon atoms, making it easier to transfer the LEDs. Firstly, high density zinc oxide (ZnO) nanowalls were grown on oxygen-plasma-treated

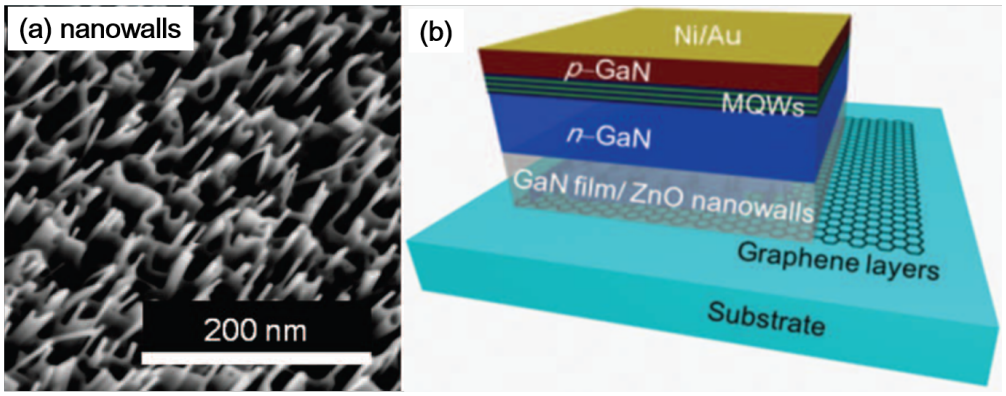

FIGURE 5.2: (a)SEM image of ZnO nanowall grown on graphene layers. (b) Schematic structure of the LEDs growth on the graphene substrates. Adapted from [3].

graphene layers as an intermediate layer for GaN growth as shown in figure 5.2(a). As ZnO and GaN have same crystal structure and small lattice mismatch, high-quality epitaxial GaN films can be grown on the nanowalls. The as-fabricated LED structures consist of n-GaN, InGaN/GaN MQWs, and p-GaN layers as shown in figure 5.2(b). After forming p-type contact and using graphene as n-contact, the thin-film LEDs on the graphene layers can be transferred mechanically from the graphene substrates onto foreign metal or plastic substrates to achieve the flexible LEDs.

5.1.2 Bending effect on the characteristics of flexible LEDs

The inorganic flexible LEDs, e.g. GaN or GaAs-based LEDs, are specially designed for applications under a bending state. However, due to the rigid characteristics of inorganic materials, bending-induced strain may cause emission wavelength shift and damage to as-fabricated flexible LEDs. Thus, the mechanical bending effect on the characteristics of flexible LEDs have been widely investigated.

The mechanical model to describe the flexible LED system has been developed by Park et al., which is initially applied for GaAs-based material analysis and can be used for GaN-based material as well [5]. As shown in figure 5.3 for a three-layers system, the strained system can be treated as a composite beam, and the distance between the neutral mechanical plane and the top surface can be expressed as

$$h_{neutral} = \sum_{i=1}^{N} \bar{E}_i h_i \left(\sum_{j=1}^{i} h_j - \frac{h_i}{2} \right) / \sum_{i=1}^{N} \bar{E}_i h_i, \tag{5.1}$$

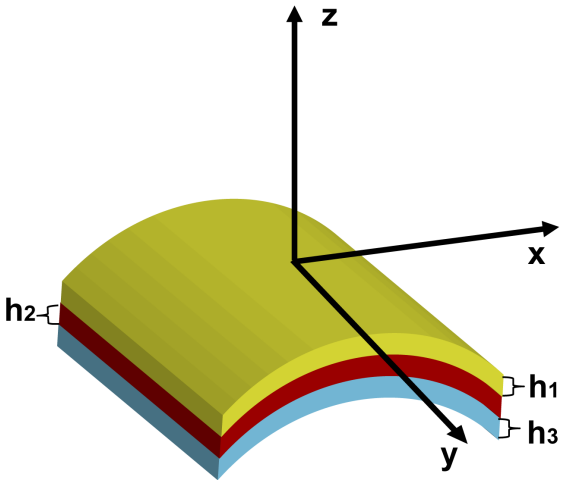

FIGURE 5.3: Schematic illustration of the three-layers strained system for analysis.

where N is the total number of layers including the LED and the packaging layers, h_i is the thickness of the i^{th} layer from the top layer, and the term $\bar{E}_i = E_i/(1-\nu_i^2)$ is determined by the Young′s modulus E_i and Poisson′s ratio ν_i of the i_{th} layer. In figure 5.3, the bending deformations correspond to in-plane uniaxial stress along the x direction, and the stresses in the y and z directions are assumed to be zero, i.e., σ_{yy}=σ_{zz}=0. The strain in the flexible LEDs is then given by

$$\varepsilon_{xx} = \gamma/R, \tag{5.2}$$

$$\varepsilon_{yy} = \varepsilon_{zz} = -\nu\varepsilon_{xx}, \tag{5.3}$$

where R is the bending radius and γ is the distance from the neutral mechanical plane to the MQWs. Using the calculated strain, the peak wavelength shifts of the EL spectra of GaAs-based LEDs were calculated which agree with the experimental results well, demonstrating the validity of the method [5]. In this work, this method was used to calculate the strain in the GaN-based LEDs, and the details of the related mechanical parameters will be shown later in Table 5.1.

Based on this model, placing the LEDs near the neutral mechanical plane can minimize the mechanically induced degradation at the interfaces of different layers [5]. One example is shown in figure 5.4(a), where the GaAs-based LED is in the middle of a polyurethane (NOA61) sheet with total thickness of ∼17 μm and the temporary PET sheet was peeled away as a final step. The flexible LEDs system can be bent to a bending radius of 0.7 mm with peak wavelength shift of ∼1 nm (figure 5.4(b)), much smaller

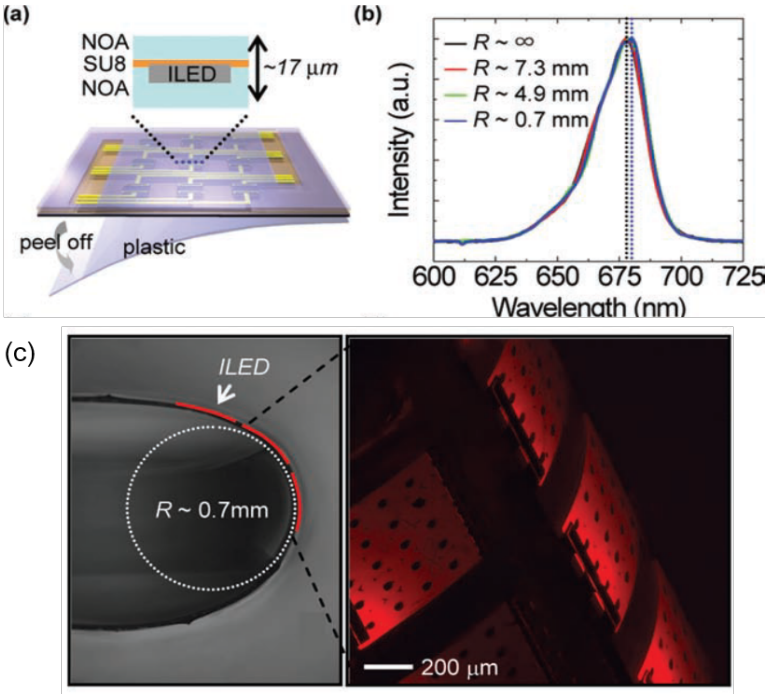

FIGURE 5.4: (a)Schematic illustration of placing the GaAs-based LEDs near the neutral mechanical plane. (b) The spectral emission shift of ∼1 nm at bending radii ranging from 0.7 mm to flat state. (c)Demonstration of flexible LEDs under bending radius 0.7 mm. From [5].

than that without neutral mechanical design. The demonstration of flexible LEDs under bending radius 0.7 mm is shown in figure 5.4(c).

Regarding GaN-based LEDs under external mechanical bending, Lee et al. reported little changes of EL spectra and current versus voltage (I-V) characteristics under bending radius 2.1 mm compared with the LED in its flat state [6]. Other groups found slight EL spectra and efficiency changes of LEDs after applying external mechanical stress [7, 8]. These observed difference may be due to the different mechanical designs of LED systems [5].

5.1.3 Applications

Flexible inorganic LEDs have been successfully used for e.g. micro-displays [4], solid state lighting [1] and biosensors [6].

Figure 5.5(a) shows a poly(dimethylsiloxane) (PDMS) module using flexible GaN-based LEDs for solid state lighting [1]. The module consists of a sheet of PDMS embossed with an array of wells filled with phosphor, which is laminated with an interconnected array

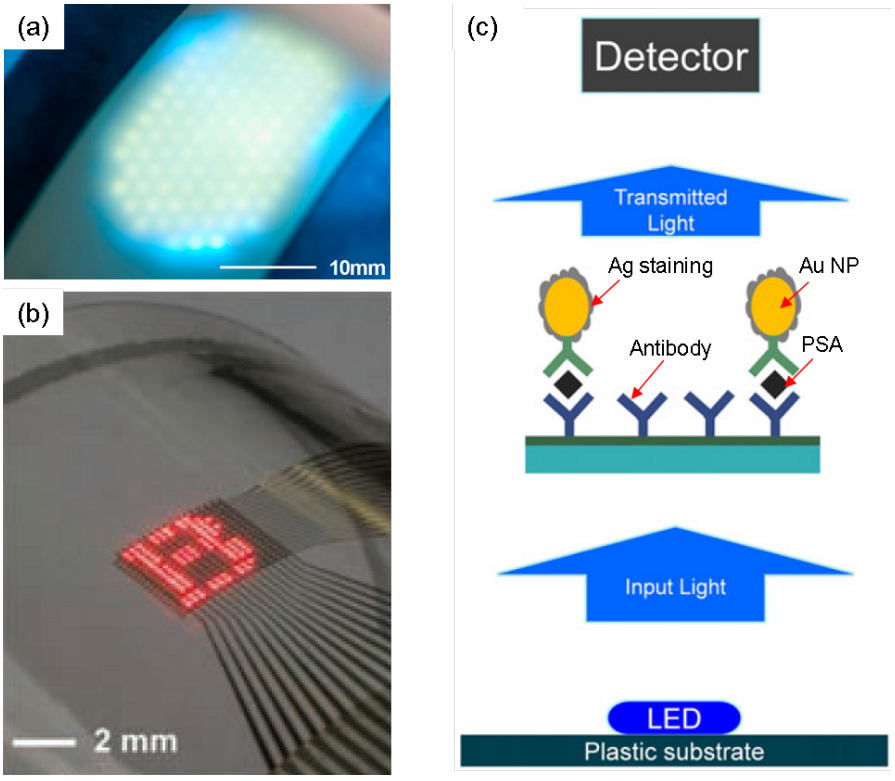

FIGURE 5.5: (a)A flexible white lighting module for solid state lighting using flexible GaN-based blue LEDs and phosphor. From [1]. (b)A flexible display incorporating a 16×16 array of GaAs-based LEDs on a cylindrical glass tube with radius ∼12 mm. The displayed pattern can be controlled by connected external interface. From [4]. (c) Schematic illustration of diseases diagnosis (e.g. PSA) by detecting the light emission intensity of GaN-based LEDs which is affected by the antigen-antibody reaction. Adapted from [6].

of LEDs which excite the phosphor to emit white light. In this module, a thin plastic diffuser film is laminated onto the LED array to achieve larger area emission. 100 LEDs with a size of 100×100 μm^2 were printed in a hexagonal array with LED spacing of 2 mm, providing an effective illuminated area more than 100 times larger than that of a traditional single LED die. Thus, using the same amount of material, this technology demonstrates strong optical and thermal benefits compared with traditional LEDs.

The LED pixels in a flexible LED array can also be individually controlled through column and row electrodes [4]. Figure 5.5(b) shows a pattern on a cylindrical glass tube with a radius of ∼12 mm, produced by a 16×16 array of GaAs-based LEDs. This micro-display technology is also suitable for flexible GaN-based LEDs.

Disease diagnosis, such as prostate-specific antigen (PSA), by using flexible GaN-based LEDs has been demonstrated [6]. In figure 5.5(c), PSA solution with various concentration were added onto the monoclonal anti (mab)-PSA coated plates. Through the

binding reaction and light blocking effects of Au nanoparticle (NP) and Ag staining, the integrated EL intensity from the flexible LEDs decreases with an increase of the PSA concentration. These results demonstrate that the flexible GaN-based LEDs can be used as LED biosensor and the bio-compatibility of flexible LEDs enables more future applications in biomedicine.

5.1.4 This work

To achieve higher LED efficiency at a high injection current, wider application and industrial production, several issues related to the fabrication and characteristics of flexible GaN-based LEDs still need to be addressed. Firstly, for fabricating high-efficiency flexible LEDs, GaN-based LED epistructures grown on sapphire substrates were commonly used [9, 10], and then a sequence of LLO and multiple subsequent steps were adopted to transfer GaN-based LED dies from a sapphire substrate onto a flexible substrate [2, 8, 11]. Each transfer step may cause damage to LED epitaxial layers, such as introducing new dislocations and/or other defects [12], which in turn may degrade the LEDs performance. Secondly, the commonly used flexible polymeric substrates, such as PET [5], do not have high thermal conductivity, and thus the transferred LED dies may degrade at a high injection current owing to ineffective heat dissipation, while the flexible substrates may themselves melt or experience thermal degradation [2]. Metal substrates offer advantages over polymers in terms of scope for permanent deformation. A third issue concerns the detailed effects of substrate bending on flexible LEDs. From previous studies of flexible GaN-based LED devices, the bending-induced strain can cause changes of EL spectra [6, 8]. Furthermore, bending to a small radius may induce substantial strains within LED layers and cause damages at the interface between LED dies and the flexible substrates, including microscopic defects, cracks or even debonding. Consequently, a systematic study of bending-induced strain effect is necessary to expand our understanding on the flexible LED devices, and to further optimize their design. Therefore, there are strong motivations from applications to achieve reliable and high performance flexible GaN-based LEDs, to simplify the transfer steps, to use substrates with higher thermal conductivity, and to better understand and optimize the performance of flexible LEDs under bending conditions.

In this work, by combining metal bonding and LLO techniques, an approach to achieve flexible VLEDs on a AuSn metal substrate with high thermal conductivity has been developed. Using this method, only one bonding and one separation step are needed to transfer the GaN-based LEDs from a sapphire substrate to a flexible metal substrate, representing a considerable simplification over the approaches such as wet-chemical underetching and transfer printing. The electrical and optical performances of these fabricated flexible VLEDs were studied as a function of substrate bending radius, including the systematic analyses of EL peak shifts induced by the strain in the MQWs of the devices. Based on these flexible VLEDs, flexible micro-LEDs were further fabricated for applications in flexible micro-displays and VLC.

5.2 Flexible VLEDs

5.2.1 Experiment

Figure 5.6 illustrates schematically the key processing steps for fabricating the flexible VLED arrays. The commercial LED wafers were grown by metal organic chemical vapor deposition on (0001) sapphire substrates. The LED epitaxial structure consists of a 2-μm-thick undoped GaN (u-GaN) layer, a 2-μm-thick Si-doped n-GaN layer, five periods of InGaN (3 nm)/GaN (10 nm) MQWs and a 0.1-μm-thick Mg-doped p-GaN layer. LED dies of 1 mm×1 mm were defined by photolithography and dry etch processes. Indium-tin-oxide (ITO) and Ti/Ag/Ti/Au layers were deposited in sequence on the mesas to form p-type ohmic contacts and reflective mirrors, respectively (figure 5.6(a)). To allow metal-to-metal bonding, thin Pd/Ti/Au layers to assist the bonding were deposited on a Si wafer to make a transfer substrate. By controlling the heating and cool down processes, the LED wafer was bonded onto the Si transfer substrate by a 50-μm-thick flexible AuSn (80:20 wt.%) layer within a vacuum furnace (figure 5.6(b)). Then, a frequency-tripled, nanosecond-pulse Nd:YAG laser with an energy density of about 600 mJ/cm^2 was used to irradiate from the sapphire backside to lift off the sapphire substrate. While the sapphire substrate was lifted off, due to the very different coefficients of thermal expansion of AuSn (15.9×10^{-6}/°C) and Si (2.6×10^{-6}/°C), the Si substrate was also separated simultaneously from the other side (figure 5.6(c)), forming flexible VLEDs with the AuSn layer retained as a flexible substrate (figure 5.6(d)). The optimization

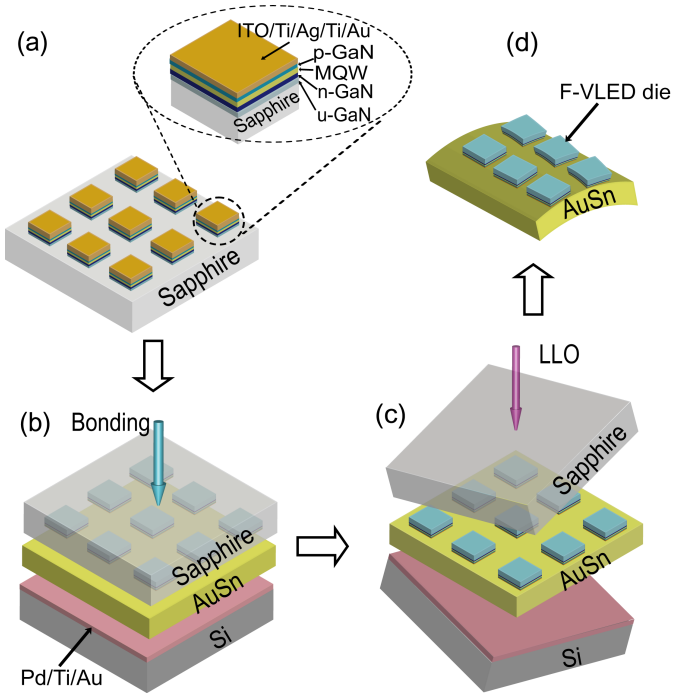

FIGURE 5.6: Schematic key processing steps for fabricating flexible VLEDs. (a) Etched LED dies on a sapphire substrate. (b) Samples at the wafer bonding stage. (c) Samples at the LLO processing stage. (d) As-fabricated flexible VLEDs under bending states.

of the metal bonding conditions and LLO parameters are critical for the fabrication of flexible VLEDs. Two-steps bonding was used, in which the temperature, pressure and dwell time could be controlled in each bonding step [13, 14]. In addition, control of cooling rate was introduced to adjust the bonding-induced stress [15]. A large residual stress at the AuSn/Si bonding interface can be induced through rapid cooling [15], which will enable the Si substrate simultaneous separation during the LLO process. The bonding conditions are as follows: to achieve this simultaneous separation, the dwell times of 3 mins at 280 °C and 4 mins at 340 °C were used in this work, followed by rapid cooling from 340 °C under nitrogen flow (versus vacuum). The *I-V* characteristics of the devices were measured by a probe station connected to an HP1415 network analyzer. The optical output power of the devices was measured by a Si photodetector brought into proximity with the devices. EL spectra were obtained by using a spectrometer (Ocean Optics USB4000 Spectrometer; ~0.3 nm resolution). All cycles of bending were within the elastic limit of the AuSn, and involved compression of a rectangular piece of the substrate from opposite sides with the edges fixed. The EL spectra were also simulated by an advanced device simulation programme $APSYS^{TM}$ [16–18].

5.2.2 Characteristics

Figures 5.7(a)-(c) show optical images of flexible VLEDs under three bending conditions, characterized by substrate bending radii of curvature, R, of ∞, 7.5 mm and 3.5 mm, respectively. The R values were estimated from the side view images. Insets in figures 5.7(a)-(c) show magnified optical images of the flexible VLEDs operating in the three different bending states after 10 bending cycles. The light emission is quite uniform under all bending radii, confirming that the flexible VLEDs can function well even at the most extreme bending condition studied. However, after 10 bending cycles, it was found that, for a few LED dies, non-uniform light emission within one LED die might appear after bending the device to 3.5 mm or smaller bending radii, which were probably caused by cracking between the flexible substrates and LED layers. The problems of cracking and non-uniform light emission can be solved by special mechanical designs, e.g. mounting the flexible VLEDs in the neutral mechanical plane [5]. To further investigate the performance of the flexible VLEDs under different bending conditions, *L-I* characteristics after 10 cycles of bending to different radii followed by elastic relaxation to the flat condition were measured and are shown in figure 5.7(d). The optical output powers of flexible VLEDs subject to the different bending conditions are almost identical

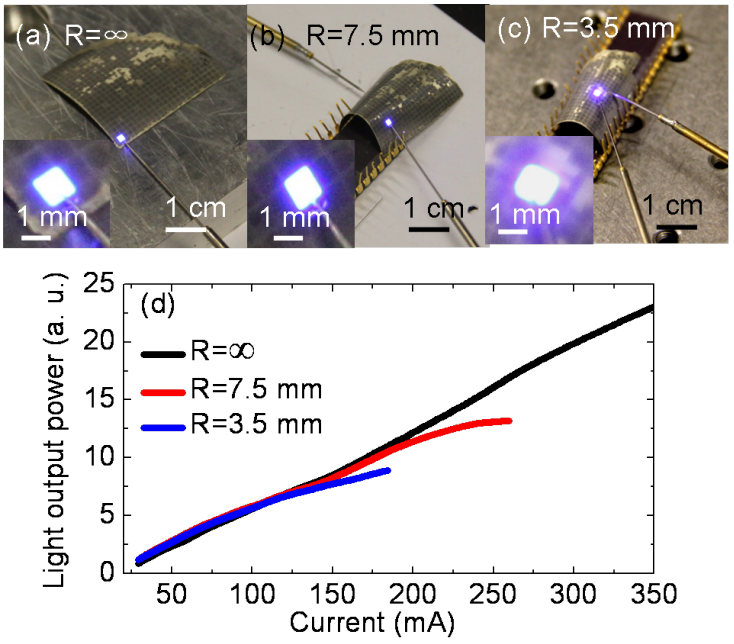

FIGURE 5.7: Optical images of flexible VLEDs with substrate bending radii of (a) ∞, (b) 7.5 mm, and (c) 3.5 mm. The insets in these figures show the enlarged images of the LED dies. (d) *L-I* characteristics as a function of bending radius after 10 bending cycles.

when the injection current is smaller than 150 mA. On further increase of the injection current, however, the flexible VLEDs subject to bending show power saturation (i.e. a thermal rollover effect), which is more pronounced for the smaller bending radius. No degradation of the AuSn substrate was observed during the flexible VLEDs operation under flexure and at high injection currents more than 150 mA. Therefore any contribution from the AuSn metal substrate to the degraded performance of the flexible VLEDs is excluded. The advantages of using the AuSn substrate are its high thermal conductivity of 57 $W{\cdot}m^{-1}{\cdot}\ K^{-1}$ which helps the heat dissipation of flexible VLEDs at high injection currents [2], and a large Young's modulus of 74 GPa in comparison with polymeric flexible substrates [19]. It is considered that the observed degradation of flexible VLED characteristics may be due to localized interfacial micro-defects produced by repeated bending, which in turn cause local current crowding [13, 14]. Such local current crowding at high injection currents will generate significant local heating, and thus reduce the overall light output.

To further analyze the effect of bending-induced strain on the flexible VLEDs and to explore the characteristics of flexible VLEDs under bending state, the EL spectra of flexible VLEDs were measured and calculated at an injection current of 20 mA. The experimental EL spectra are shown in figure 5.8, which shows the LED emission at infinite bending radius is centred at ~467 nm. Gaussian fittings of several EL spectra at

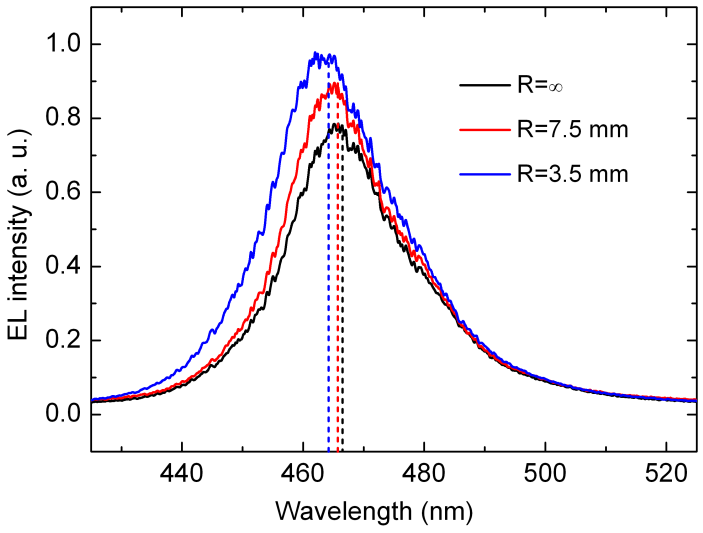

FIGURE 5.8: Experimentally measured EL spectra of flexible VLEDs at 20 mA with substrate bending radii of ∞, 7.5 mm and 3.5 mm, respectively.

each bending radius have been done and the average EL peak values are used to minimize the fitting errors. As the bending radius decreases to 7.5 mm and 3.5 mm, the emission wavelength peak shows blue shifts of ∼0.8 nm and ∼2.3 nm, respectively. It is considered that these small, but systematic shifts are due to the changed strain condition in the MQWs induced by the mechanical bending.

To interpret this behaviour in more detail, the strains and corresponding QCSE effect in the MQWs are analyzed. Using the model described by equations 5.1, 5.2 and 5.3, the strain in MQWs of flexible VLEDs under different bending radii can be estimated. The strain dependence of the emission wavelength can be evaluated approximately by considering the change of polarization field P_{ez} (interface-bound sheet charge density) in InGaN/GaN quantum wells using the equation $P_{ez} = e_{31}\varepsilon_{xx} + e_{32}\varepsilon_{yy} + e_{33}\varepsilon_{zz}$, where e_{31}, e_{32}, and e_{33} are the piezoelectric coefficients, and $e_{31} = e_{32}$ [20]. In the flat state ($R = \infty$), the built-in charge density induced by the spontaneous and piezoelectric polarization at the interfaces of the InGaN/GaN layers is calculated by the method developed by Fiorentini et al. [21]. Then, with the different interface-bound charge density under different bending radii, the physical properties of flexible VLEDs under different bending conditions are modeled using the commercial *APSYS* simulation programme. The mechanical parameters to evaluate the strain effect are listed in table 5.1, and the piezoelectric coefficients e_{31} and e_{33} are chosen to be -0.41 and 0.81, respectively [20]. The actual polarization field in the MQWs is usually calculated using an assumed carrier screening factor, caused by interface defects and/or mobile charges in the InGaN/GaN MQWs [22]. Using a screening factor 20% [22], simulated EL spectra show peak shifts of ∼0.86 nm at bending radius 7.5 mm and ∼2.27 nm at bending radius 3.5 mm, respectively, compared with EL peak under flat state. The agreement of experimental and calculated results confirms that the strain-induced reduction of QCSE in the InGaN/-GaN MQWs is the key factor contributing to the systemic blue shift of EL peak with decreasing bending radius.

TABLE 5.1: Mechanical parameters used to evaluate the strain effect on flexible VLEDs.

Material	Thickness (μm)	Young′s modulus E_i (GPa)	Poisson′s ratio ν_i
GaN [23, 24]	3.5	287	0.202
AuSn [19]	50	74	0.4

5.3 Flexible micro-LEDs

Due to the wide applications of micro-LEDs in various areas, e.g. micro-displays [25] and VLC [26, 27], flexible micro-LEDs were further fabricated based on the flexible VLED achieved.

5.3.1 Fabrication

Figure 5.9 illustrates the key processing steps for fabricating flexible micro-LEDs using the same flexible LED wafer with 1 mm × 1 mm patterns as shown in figure 5.7. Firstly, the wafer was bonded onto a Si substrate by dissolvable adhesive to facilitate photolithograph. Dry etching was used to etch a 4 × 4 flexible micro-LED array down to the AuSn substrate with a pixel size of 140 μm×140 μm. Then a SU8-2002 isolation layer for the p-pad and n-pad was spun and apertures on each LED mesa were then created by photolithography. After surface treatment with HF and diluted HCL:H_2O (1:1) solution, Ti/Al/Ti/Au layers were deposited on the mesas to form n-contact and to interconnect micro-LED pixels. In figure 5.9, electrodes connecting a 4×4 micro-LED array are shown. The design of individually addressing each micro-LED pixel can be also achieved for different applications. Finally, the flexible micro-LEDs device fabrication was completed by removing the temporary Si substrates through dissolving the adhesive.

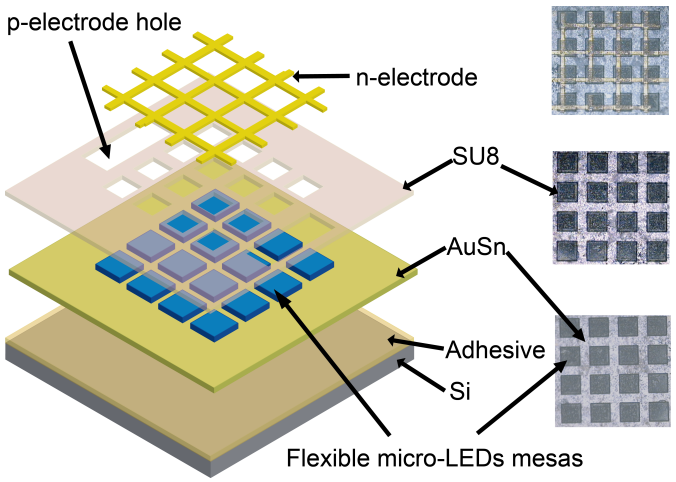

FIGURE 5.9: In the left frame are illustrations of processing steps for fabricating flexible micro-LEDs. In the right frame are the microphotographs of flexible micro-LEDs during fabrication. Bottom: etched the flexible micro-LEDs mesas. Middle: patterned SU8 as isolation layer for p-pad and n-pad. Top: deposited Ti/Al/Ti/Au to form n-contact and interconnected electrodes of flexible micro-LEDs array.

5.3.2 Characteristics

One typical *I-V* curve of one flexible micro-LED after ten bending cycles was measured under flat state, as shown in figure 5.10(a). And *L-I* curve of one flexible micro-LED under a bending radius 6 mm is shown in figure 5.10(b). The optical image of probing one flexible micro-LED pixel on a column with a radius 6 mm is shown in the inset of figure 5.10(b). The broad-area LEDs pattern can be seen clearly as a 4×4 flexible micro-LEDs array is defined within a broad-area LED pixel.

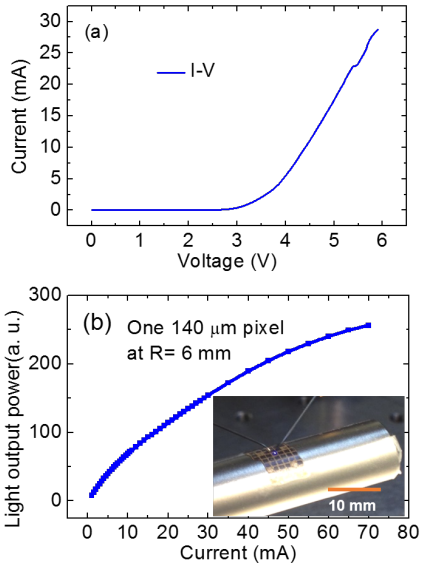

FIGURE 5.10: (a)*I-V* characteristics of one flexible micro-LED pixel after 10 bending cycles. (b)*L-I* characteristics of flexible micro-LED pixel under a bending radius 6 mm. Inset: optical image of probing a flexible micro-LED pixel on a column with a bending radius 6 mm.

5.3.3 Applications of flexible micro-LEDs

Flexible micro-displays

To demonstrate the application of flexible micro-LEDs in micro-displays, figure 5.11(a) shows an optical image of fabricated flexible micro-LED pixels under a bending radius of 12 mm. In figure 5.11(b) and (c), a line and an array of flexible micro-LED pixels are shown demonstrating the potential applications in flexible micro-displays. However, it is found that the pixel-to-pixel light emission is non-uniform and some pixels cannot be switched on. This is probably due to the deep mesa etching of each micro-LED pixel and the etched depth is around 6 μm including both epitaxial GaN layers and metal

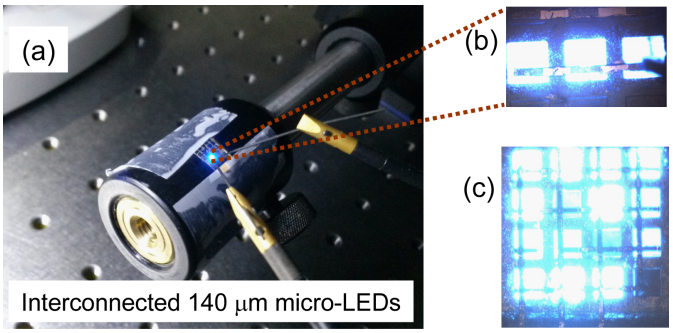

FIGURE 5.11: (a)Typical optical image of probing interconnected flexible micro-LED pixels on a column with bending radius 12 mm. Light emission of (b) a row and (c) a 4×4 array of flexible micro-LEDs. The pixel size is 140 μm.

contacts. Also, the rough LLO GaN surface on which the electrodes were grown, may induce additional resistance of electrodes interconnecting the micro-LED pixels or even the disconnection.

Visible light communication

In previous studies, it has been demonstrated that the micro-LEDs have performance advantages over broad-area LEDs in VLC [26, 27]. However, the characterization and application of flexible micro-LEDs in VLC has not been reported. To demonstrate the potential application of flexible micro-LEDs in VLC, the modulation bandwidth and eye diagrams were obtained. Figure 5.12(a) shows the setup for these measurement, in which one flexible micro-LED was probed on a column with bending radius 12 mm and the emission light was collected by a photodetector through optical lens. In figure 5.12(b), it was found the measured modulation bandwidth of a LED pixel gradually increases under ~20 mA, and saturates at ~ 40 MHz from ~20 mA to 52 mA. As the *n*-contact is not fully optimized, so the flexible micro-LEDs may have high series resistance, causing the bandwidth saturation due to resistance-capacitance limitation. However, the bandwidth saturation current density ~100 A/cm^2 of flexible micro-LEDs is much higher than the thermal saturation current density ~ 30 A/cm^2 of flexible broad-area VLEDs. As previous studies show that the modulation bandwidths of LEDs with different sizes are similar at the same current densities [27], the flexible micro-LEDs show significant advantages over flexible broad-area VLEDs in VLC application. Furthermore, to show the device can be actually used for data transmission, the eye diagrams of flexible micro-LEDs at a data transmission rate of 75 Mbit/s were taken at an injection current of 28 mA as shown in figure 5.12(c). Although the bandwidths at injection currents larger than ~20 mA are similar as shown in figure 5.12(b), a higher data transmission rate,

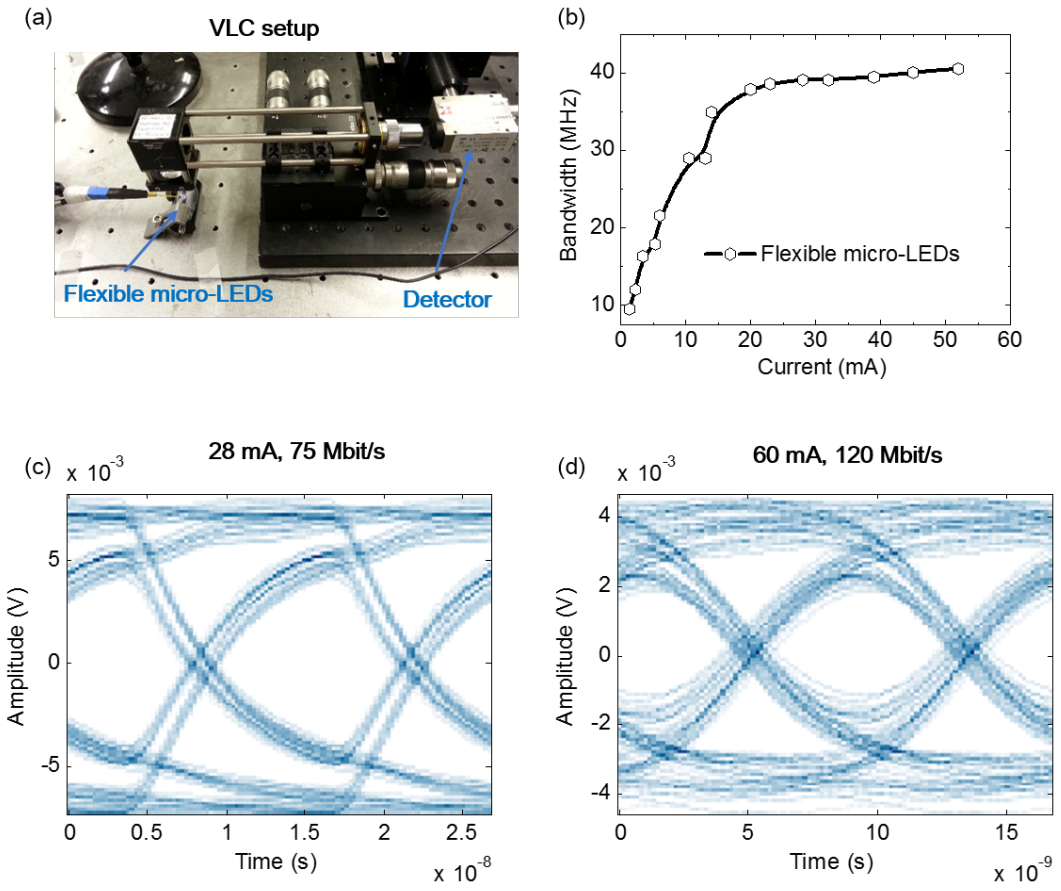

FIGURE 5.12: (a)The VLC setup for flexible micro-LEDs under bending radius 12 mm. (b)Measured modulation bandwidth of one typical flexible micro-LED pixel. The eye diagrams for data transmission speeds (c)75 Mbit/s at 28 mA and (d)120 Mbit/s at 60 mA.

such as 120 Mbit/s (figure 5.12(d)), can be only achieved at a higher injection current, e.g. 60 mA. These results demonstrate the potential application of flexible micro-LEDs in VLC, but also show the high modulation bandwidth and high light output power are both important for high-speed data transmission.

5.4 Summary

Using a novel combination of metal bonding/debonding and LLO techniques, flexible VLEDs were fabricated on flexible AuSn metal substrates with only one transfer step, thus demonstrating a much simplified and highly reliable fabrication method. Even under severe bending of the substrate the mechanically-induced strain causes little evident damage to the GaN-based LED layers and flexible AuSn substrates, but does induce defects at the bonding interface. Thus, the *L-I* characteristics degrade at high injection

current. Calculations confirm that the reduction in QCSE affecting the MQWs can explain the systematic blue shift of the EL peak with smaller bending radius. Based on the flexible broad-area LEDs, flexible micro-LEDs were fabricated for applications in micro-displays and VLC. Light emission of interconnected flexible micro-LED pixels demonstrates the potential application in micro-displays. The flexible micro-LEDs can achieve a maximum bandwidth ∼40 MHz and data transmission speed 120 Mbits/s at 60 mA, suitable for VLC.

References

[1] H.-S. Kim, E. Brueckner, J. Song, Y. Li, S. Kim, C. Lu, J. Sulkin, K. Choquette, Y. Huang, R. G. Nuzzo, and J. A. Rogers. Unusual strategies for using indium gallium nitride grown on silicon (111) for solid-state lighting. *Proceedings of the National Academy of Sciences*, 108(25):10072–10077, 2011.

[2] T. Kim, Y. H. Jung, J. Song, D. Kim, Y. Li, H. Kim, I.-S. Song, J. J. Wierer, H. A. Pao, Y. Huang, and J. A. Rogers. High-efficiency, microscale GaN light-emitting diodes and their thermal properties on unusual substrates. *Small*, 8(11):1643–1649, 2012.

[3] K. Chung, C.-H. Lee, and G.-C. Yi. Transferable GaN layers grown on ZnO-coated graphene layers for optoelectronic devices. *Science*, 330(6004):655–657, 2010.

[4] S.-I. Park, Y. Xiong, R.-H. Kim, P. Elvikis, M. Meitl, D.-H. Kim, J. Wu, J. Yoon, C.-J. Yu, Z. Liu, Y. Huang, K. Hwang, P. Ferreira, X. Li, K. Choquette, and J. A. Rogers. Printed assemblies of inorganic light-emitting diodes for deformable and semitransparent displays. *Science*, 325(5943):977–981, 2009.

[5] S.-I. Park, A.-P. Le, J. Wu, Y. Huang, X. Li, and J. A. Rogers. Light emission characteristics and mechanics of foldable inorganic light-emitting diodes. *Advanced Materials*, 22(28):3062–3066, 2010.

[6] S. Y. Lee, K.-I. Park, C. Huh, M. Koo, H. G. Yoo, S. Kim, C. S. Ah, G. Y. Sung, and K. J. Lee. Water-resistant flexible GaN LED on a liquid crystal polymer substrate for implantable biomedical applications. *Nano Energy*, 1(1):145–151, 2012.

[7] J. Xu, M. F. Schubert, D. Zhu, J. Cho, E. F. Schubert, H. Shim, and C. Sone. Effects of polarization-field tuning in GaInN light-emitting diodes. *Applied Physics Letters*, 99(4): 041105, 2011.

[8] H.-Y. Kuo, S.-J. Wang, P.-R. Wang, K.-M. Uang, T.-M. Chen, S.-L. Chen, W.-C. Lee, H.-K. Hsu, J.-C. Chou, and C.-H. Wu. Use of elastic conductive adhesive as the bonding agent for the fabrication of vertical structure GaN-based LEDs on flexible metal substrate. *IEEE Photonics Technology Letters*, 20(7):523–525, 2008.

[9] O. B. Shchekin, J. E. Epler, T. A. Trottier, T. Margalith, D. A. Steigerwald, M. O. Holcomb, P. S. Martin, and M. R. Krames. High performance thin-film flip-chip InGaN–GaN light-emitting diodes. *Applied Physics Letters*, 89(7):071109, 2006.

[10] Y. Sun, S. Trieu, T. Yu, Z. Chen, S. Qi, P. Tian, J. Deng, X. Jin, and G. Zhang. GaN-based LEDs with a high light extraction composite surface structure fabricated by a modified YAG laser lift-off technology and the patterned sapphire substrates. *Semiconductor Science and Technology*, 26(8):085008, 2011.

[11] Y. Jung, X. Wang, J. Kim, S. H. Kim, F. Ren, S. J. Pearton, and J. Kim. GaN-based light-emitting diodes on origami substrates. *Applied Physics Letters*, 100(23):231113, 2012.

[12] Y. Sun, T. Yu, H. Zhao, X. Shan, X. Zhang, Z. Chen, X. Kang, D. Yu, and G. Zhang. Microanalyses of the reverse-bias leakage current increase in the laser lift off GaN-based light emitting diodes. *Journal of Applied Physics*, 106(1):013101, 2009.

[13] J. W. R. Tew, X. Q. Shi, and S. Yuan. Au/Sn solder for face-down bonding of AlGaAs/GaAs ridge waveguide laser diodes. *Materials Letters*, 58(21):2695–2699, 2004.

[14] W. Pittroff, G. Erbert, G. Beister, F. Bugge, A. Klein, A. Knauer, J. Maege, P. Ressel, J. Sebastian, R. Staske, and G. Traenkle. Mounting of high power laser diodes on boron nitride heat sinks using an optimized Au/Sn metallurgy. *IEEE Transactions on Advanced Packaging*, 24(4):434–441, 2001.

[15] P. Tian, Z. Chen, Y. Sun, S. Qi, H. Zhang, J. Deng, F. Yu, T. Yu, X. Kang, Z. Qin, and G. Zhang. Phase distribution in eutectic AuSn layer changed by temperature ramping rate and its effect on the performance of GaN-based vertical structure LEDs. *Materials Science and Engineering: B*, 175(3):213–216, 2010.

[16] J.-R. Chen, Y.-C. Wu, S.-C. Ling, T.-S. Ko, T.-C. Lu, H.-C. Kuo, Y.-K. Kuo, and S.-C. Wang. Investigation of wavelength-dependent efficiency droop in InGaN light-emitting diodes. *Applied Physics B*, 98(4):779–789, 2010.

[17] Z.-M. Li, K. M. Dzurko, A. Delage, and S. P. McAlister. A self-consistent two-dimensional model of quantum-well semiconductor lasers: optimization of a GRIN-SCH SQW laser structure. *IEEE Journal of Quantum Electronics*, 28(4):792–803, 1992.

[18] Z.-M. Li, M. Dion, Y. Zou, J. Wang, M. Davies, and S. P. McAlister. An approximate k· p theory for optical gain of strained InGaAsP quantum-well lasers. *IEEE Journal of Quantum Electronics*, 30(2):538–546, 1994.

[19] R. R. Chromik, D. N. Wang, A. Shugar, L. Limata, M. R. Notis, and R. P. Vinci. Mechanical properties of intermetallic compounds in the Au-Sn system. *Journal of Materials Research*, 20(8):2161–2172, 2005.

[20] O. Ambacher, J. Majewski, C. Miskys, A. Link, M. Hermann, M. Eickhoff, M. Stutzmann, F. Bernardini, V. Fiorentini, V. Tilak, B. Schaff, and L. F. Eastman. Pyroelectric properties of Al (In) GaN/GaN hetero-and quantum well structures. *Journal of Physics: Condensed Matter*, 14(13):3399, 2002.

[21] V. Fiorentini, F. Bernardini, and O. Ambacher. Evidence for nonlinear macroscopic polarization in III–V nitride alloy heterostructures. *Applied Physics Letters*, 80(7):1204–1206, 2002.

[22] J. Piprek and S. Nakamura. Physics of high-power InGaN/GaN lasers. *IEEE Proceedings-Optoelectronics*, 149(4):145–151, 2002.

[23] M. D. Drory, J. W. Ager, T. Suski, I. Grzegory, and S. Porowski. Hardness and fracture toughness of bulk single crystal gallium nitride. *Applied Physics Letters*, 69(26):4044–4046, 1996.

[24] M. A. Moram, Z. H. Barber, and C. J. Humphreys. Accurate experimental determination of the Poisson′s ratio of GaN using high-resolution x-ray diffraction. *Journal of Applied Physics*, 102(2):023505, 2007.

[25] J. Day, J. Li, D. Y. C. Lie, C. Bradford, J. Y. Lin, and H. X. Jiang. III-Nitride full-scale high-resolution microdisplays. *Applied Physics Letters*, 99(3):031116, 2011.

[26] J. J. D. McKendry, R. P. Green, A. E. Kelly, Z. Gong, B. Guilhabert, D. Massoubre, E. Gu, and M. D. Dawson. High-speed visible light communications using individual pixels in a micro light-emitting diode array. *IEEE Photonics Technology Letters*, 22(18):1346–1348, 2010.

[27] J. J. D. McKendry, D. Massoubre, S. Zhang, B. R. Rae, R. P. Green, E. Gu, R. K. Henderson, A. E. Kelly, and M. D. Dawson. Visible-light communications using a CMOS-controlled micro-light-emitting-diode array. *Journal of Lightwave Technology*, 30(1):61–67, 2012.

Chapter 6

GaN-based micro-LEDs on Si substrates

This chapter describes the fabrication, characteristics, and applications of GaN-based micro-LEDs on Si substrates. The main contents of this work have been published in: *J. Appl. Phys.* **115**, 033112 (2014). First, the advantages and challenges of GaN-based LEDs grown on Si substrates are reviewed. Then, using a GaN-based LED epitaxial structure grown on Si, individually addressable 10×10 micro-LED arrays with a pixel diameter of 45 μm and peak emission at ∼470 nm have been demonstrated. The electrical and optical properties of these micro-LEDs were compared with those of broad-area LEDs fabricated from the same epistructure. It was shown that the micro-LEDs can sustain a much higher current density, up to 6.6 kA/cm^2, before thermal rollover. Also the fabricated micro-LEDs show good pixel-to-pixel uniformity, which demonstrates potential for low-cost micro-displays. Furthermore, these micro-LEDs demonstrate a high electrical-to-optical modulation bandwidth of up to ∼270 MHz and a data transmission rate up to 400 Mbit/s which make them suitable for visible light communication (VLC). The electrical-to-optical modulation bandwidth of these micro-LEDs increases rapidly with injection currents less than ∼6 mA, temporarily saturates at injection currents of ∼6 to ∼35 mA, and gradually increases again with injection currents from ∼35 mA to 110 mA. Our analyses show that carrier density dependent recombination processes are responsible for the bandwidth increase at low injection current, the resistance-capacitance product determines the modulation bandwidth in the saturation region, and self-heating,

which changes series resistance of micro-LEDs, may cause a further bandwidth increase at high current.

6.1 Introduction

6.1.1 Advantages of GaN-based LEDs on Si substrates

GaN-based LEDs have many advantages over traditional light sources including efficiency, lifetime and robustness, but are relatively more expensive due to the materials employed and manufacturing processes. GaN-based LEDs have been achieved on sapphire, 6 H-SiC and Si substrates. For comparison, the material parameters of GaN, AlN, sapphire, 6 H-SiC and Si are listed in table 6.1 [1]. GaN-based LEDs grown on sapphire substrates are commonly used but the relatively large lattice mismatch between GaN and sapphire substrates limits the LED efficiency and lifetime. This has led to the use of SiC substrates, which has a more closely lattice match to GaN. However, both sapphire and SiC are expensive and wafer sizes are small, so typically 2 or 4 inch wafers are produced on these substrates.

The biggest advantage of Si as a substrate for GaN-based LEDs is the availability of large-area substrates at relatively low cost compared with sapphire and SiC. LEDs grown on larger Si (6 or 8 inch) wafers have been achieved [1]. This cost advantage is likely to remain significant irrespective of advances in substrate processing technology. For example, energy costs for crystal growth of Si are lower in view of its lower melting temperature. Si is also a less hard material, and therefore easier to cut into wafers. Whatever the choice of substrate material, larger substrate sizes will reduce overall device manufacturing cost through more automatable and higher-yield processing steps. Table 6.2 shows the available LED wafer area per run in a commercial AXITRON 2800G4 HT reactor, where a 44% increase in throughput by using 6 inch wafers instead of 2 inch wafers can be clearly seen [1]. Additional advantages of Si include a wide choice of substrate removal routes in LED process flows, and efficient radiative coupling to the susceptors of epitaxial growth reactors, which becomes important for temperature uniformity in situations in which substrate curvature during growth cannot be fully avoided [1–6]. These characteristics are usually considered in the context of mass-market broad-area LEDs for solid state lighting (SSL). The low cost of large-area LED epitaxial

TABLE 6.1: Material parameters of GaN, AlN, sapphire, 6 H-SiC and Si [1]. Both calculated[a] and experimental[b] values are given for the melting point of GaN and AlN.

Material	GaN	AlN	Sapphire	6 H-SiC	Si
Lattice constant(Å)	a=3.189	a=3.112	a=4.759	a=3.081	a=5.431
Lattice constant(Å)	c=5.185	c=4.982	c=12.991	c=15.117	-
Thermal expansion coefficient a (10^{-6} K^{-1})	5.59	5.27	7.3	4.46	2.6
Thermal expansion coefficient c (10^{-6} K^{-1})	3.17	4.15	8.5	4.16	2.6
Thermal conductivity (W cm^{-1} K^{-1})	4.1	5.9	0.41	4.9	1.3
Melting point (K)	2791^a(>2000^b)	3487^a(∼3300^b)	2303	3102	1690

TABLE 6.2: Throughput increase of large wafer substrates by comparison of the usable wafer area in a commercial AIXTRON 2800G4 HT reactor [1].

Wafers size (inch)	2	4	6
Wafers number in reactor	42	11	6
Usable area (no edge exclusion) (mm^2)	~82500	~86400	~106000
Usable area (with 2 mm edge exclusion) (mm^2)	~69800	~79600	~100500
Throughput increase	-	14%	44 %

wafers on Si is also very relevant to those micro-LED products aimed at larger markets, while the large wafer sizes offer increased yields of large 2-dimensional or linear micro-LED arrays than are possible with 2-inch wafers.

6.1.2 Challenges and solutions of GaN-based LEDs on Si substrates

In growth using the preferred production technique of metal organic vapour phase epitaxy (MOVPE), the Si(111) orientation is most favoured for GaN-based LEDs growth. The advantages of growth on Si substrates have been discussed in last section, but the growth is still challenging due to several problems, especially the wafer cracking and high threading dislocation density. Some of these issues have been successfully addressed through optimized growth initiation and strain management layers [1–5]. The details are discussed as follows.

MOVPE growth

At the initial growth stage, it is challenging to remove the amorphous native oxide surface layer by *ex situ* chemical etching in a consistent manner. The solution is to heat the Si *in situ* in a hydrogen atmosphere to a temperature, e.g. 1350 °C [7], so the oxide layer becomes thermodynamically unstable and leaves the Si surface.

In addition, the Ga reacts with Si to form Ga-Si alloy if GaN is directly grown on Si substrates, causing significant roughened substrate and film. Buffer layers such as Al_2O_3 [8], SiC [9], ScN [10] have been used to prevent the reaction between GaN and Si. These materials have close lattice and/or thermal match to GaN, but most of them cannot currently be grown by MOVPE, which means additional deposition procedures outside the growth reactor are required. Currently, a popular method is to grow AlN buffer layer on Si. The AlN/Si interface largely determines the material quality of subsequently grown AlN and GaN layers [1]. Trimethylaluminum (TMA) pre-dose has been used to

prevent the SiN_x formation at the interface, but the the SiN_x is still present in many reports [1, 11]. A low-temperature AlN growth can decrease the kinetics of inter-diffusion and thereby the formation of a SiN_x interlayer [12].

Due to the much smaller thermal expansion coefficient of Si than that of GaN, the GaN films grown on Si also suffer from tensile stress, which causes wafer cracking and wafer bowing affecting the LED performance and the LED fabrication processes. Several methods have been proposed to address this issue, including the use of patterned substrates to limit the cracks [13], substrate engineering by using compliant substrates [14], and tensile stress compensation by introducing a low-temperature AlN nucleation layer and an AlGaN intermediate layer [1, 2]. The AlGaN intermediate layer is used for the LED material growth in this work. As show in figure 6.1(a), due to large in-plane lattice parameter mismatch between AlGaN and AlN, an AlGaN layer is under compressive strain when it is grown on relaxed AlN, causing convex bowing. However, during the cooling stage to room temperature, because of the different thermal expansion coefficients of AlGaN and Si substrates, tensile strain causes a concave bowing as shown in figure 6.1(b).

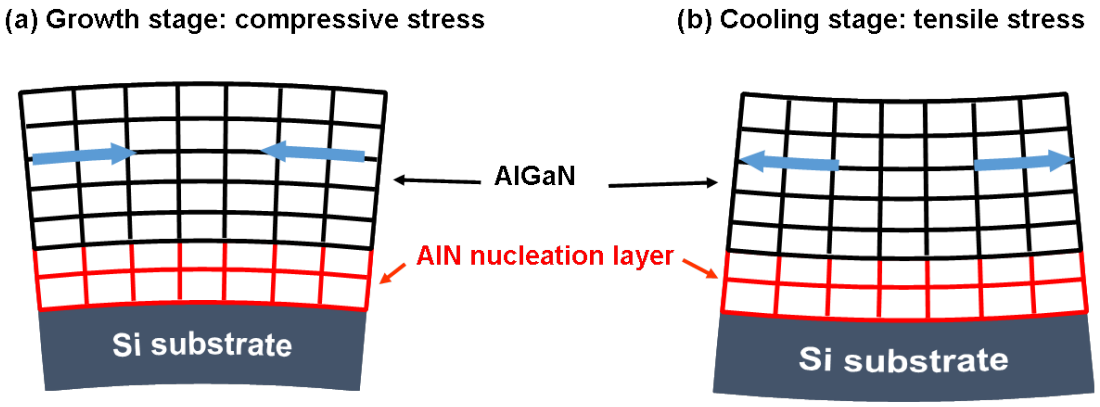

FIGURE 6.1: Schematic illustration of (a) the compressive strain caused by the lattice mismatch between AlGaN and AlN layer and (b) the tensile strain during cooling due to the thermal mismatch of AlGaN and Si substrates. Reproduced from [1].

Due to the large lattice mismatch of ~17% between GaN (0001) and Si (111), a high density of dislocations is also induced. Progress has been made in reducing density of threading dislocations in GaN epistructures grown on Si, although the overall structural quality of LEDs grown on Si substrate is still generally lower than the comparable structures on sapphire substrates. Epitaxial lateral overgrowth (ELOG) of GaN on Si (111) has been investigated to reduce the dislocation density [1]. The principle of ELOG is

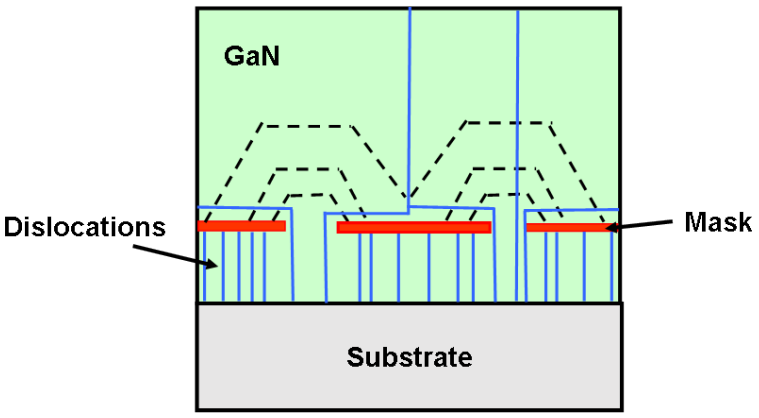

FIGURE 6.2: Schematic illustration of the principle of ELOG to reduce the dislocation density. Reproduced from [1].

illustrated in figure 6.2. A patterned mask layer, e.g. SiN_x, is deposited on a GaN layer. The regrowth of GaN causes the bending of dislocations underneath the mask to the window regions and increases the chance of dislocation annihilation. The mask also blocks the dislocations from propagating to the GaN above the mask regions. These effects can result in a much lower dislocation density. Inserting SiN_x interlayer into the GaN layer is the commonly used method to reduce the dislocation density [15]. The thin SiN_x layer serves as a mask containing random holes, so its dislocation reduction mechanism can be considered as nano-ELOG.

Chips processing after growth

Since Si substrates absorb the emitted light, for high brightness LEDs, vertical thin-film LEDs have been fabricated for LEDs grown on Si substrates by Osram [16]. In this technique, a *p*-contact and highly reflective *p*-contact mirror were formed. Then the wafer was bonded onto a Si carrier substrate and the original Si substrate for wafer growth was removed. Finally, surface roughening and *n*-contacting could be done. By combining such LEDs with a phosphor converter in a standard housing, white LEDs can be achieved which have an efficiency of 127 lm/W at 350 mA for 1 mm^2 chips.

6.1.3 GaN-on-Si micro-LEDs developed in this work

In recent years, it has been demonstrated that GaN-based micro-LEDs have a range of advanced applications, due to their special properties of micro-size, improved thermal management and the capability to sustain higher current densities, etc. [17–19] Micro-LED based high-functional devices and micro-systems such as displays [20], monolithic

arrays driven by alternating current (AC) mains voltage for solid-state lighting [21], sources offering fast modulation for VLC [22–24], direct LED writing [25], emitter arrays for optogenetics [26, 27], and optical tweezing systems [28], have been developed. All these micro-LEDs have utilized relatively mature GaN-based epistructures grown on sapphire substrates, most commonly 2-inch wafers with (0001) orientation. Parallel developments of micro-LED technology using GaN LED structure growth on Si substrates, most commonly in the (111) orientation with large wafer diameters up to 6-inch, have not been reported.

In this work, individually addressable 10×10 micro-LED arrays were fabricated from a GaN-based LED structure grown on a Si substrate (material grown at the University of Cambridge). These are top-emitting, or *p*-up devices, with a geometry not fully optimised for light extraction. However, the scope for Si substrate removal will allow future development of analogous flip-chip arrays. The direct current (DC) characteristics of these micro-LEDs were analysed and compared with those of broad-area LEDs. The potential applications of these devices for micro-displays and visible light communication of micro-LEDs were investigated by characterizing their emission uniformity, bandwidth and data stream transmission. The mechanisms underlying the bandwidth dependence on current are also investigated in detail.

6.2 Experimental details

The LED structures were grown on Si(111) by MOVPE, performed on 6-inch round substrates. Further details of growth and the epitaxial layer sequence are available elsewhere [2, 3]. In brief, the epistructures consist of an AlN nucleation layer, an AlGaN strain management layer, and a Si-doped GaN layer, followed by InGaN/GaN multiple quantum wells (MQWs), an AlGaN current blocking layer, and a *p*-type GaN layer. The total III-nitride thickness is ∼2μm, and threading dislocation densities are estimated at $\sim 2 \times 10^9$ cm^{-2}. 10×10 micro-LED arrays, with pixel diameters of 45 μm on a 100 μm pitch, were fabricated, and the processing steps of one micro-LED pixel can be seen in figure 6.3. At the start of the processing sequence, Ni/Au (10 nm/25 nm) metal layers were deposited on *p*-GaN to perform a current spreading role. Then, reactive-ion etching and inductively coupled plasma etching were used to etch the Ni/Au and GaN layers respectively, to define circular micro-LED mesas with a diameter of 45 μm. After the

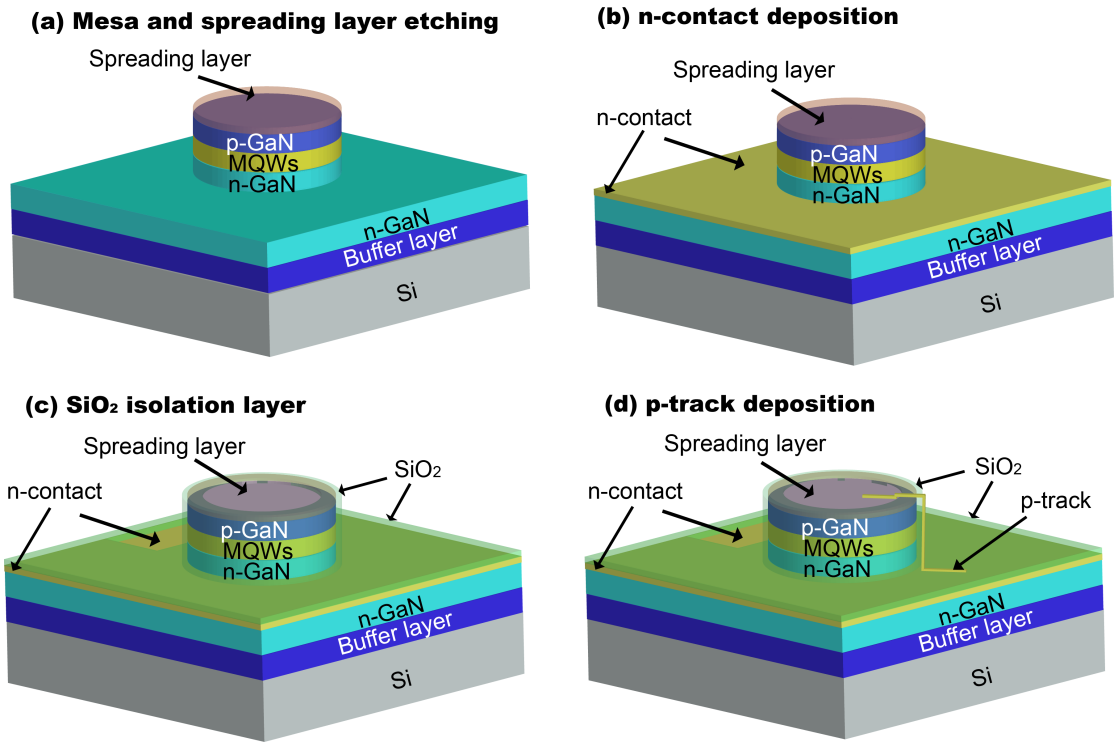

FIGURE 6.3: Processing steps of micro-LEDs on Si substrates: (a) mesa and spreading layer etching, (b) *n*-contact deposition, (c) SiO_2 isolation layer deposition and (d) *p*-track deposition.

mesa etching, the current spreading layer was thermally annealed in purified air. Then Ti/Au (50 nm/200 nm) layers were deposited around the mesas as the *n*-pad common to all pixels. After that step, a silicon dioxide (SiO_2) passivation layer was deposited by plasma-enhanced chemical vapour deposition and SiO_2 apertures on each mesa were then defined by HF-based wet etching. Finally, Ti/Au (layer thicknesses again 50 nm/200 nm) interconnection tracks were fabricated to allow each pixel to be addressed individually. The micro-LEDs were bonded onto a package, allowing light to be extracted through

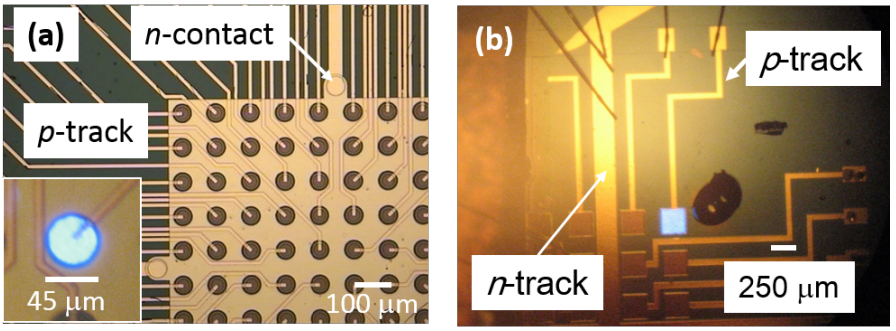

FIGURE 6.4: Micrographs of the individually addressable (a) 10×10 micro-LEDs array (inset at bottom left: light emission through the spreading layer of a representative pixel) and (b) the broad-area LEDs array.

the spreading layer. Optical micrographs of a completed micro-LED array are shown in figure 6.4(a), in which the inset shows the uniform light emission from a representative pixel. 250 μm×250 μm broad-area LEDs were also fabricated with the same epitaxial material using similar processes for comparison purposes, as shown in figure 6.4(b).

The current versus voltage (I-V) characteristics of the as-fabricated micro-LEDs were measured by a current source, through scanning each data point under DC conditions. The light output power versus current (L-I) characteristics of micro-LEDs were measured using a Si detector in proximity to the device. Thus only the light emitted in the upward direction was collected, corresponding to the directed output power relevant for most applications. The electroluminescence (EL) spectra of the LEDs were measured by using a spectrometer (Ocean Optics USB4000 Spectrometer; ∼0.3 nm resolution). The optical -3dB modulation bandwidth of these LED pixels was measured as follows. A small-signal modulation, of fixed amplitude, from an HP8753ES network analyser was combined with a direct current (DC) bias using a bias-tee and applied to a representative LED pixel using a high-speed probe. The light output from the pixel was measured using a 1.4 GHz bandwidth photoreceiver and the frequency response was recorded by the network analyser [22, 23]. Data stream transmission was tested by using pseudo-random binary sequences with a standard pattern length of 2^7-1 bits and a peak-to-peak voltage swing of 0 to 2 V.

6.3 Performance of GaN-on-Si micro-LED arrays

To evaluate the pixel-to-pixel electrical and optical uniformity of a 10×10 micro-LED array, the current at a fixed bias of 5 V and the light output power at a fixed current of 1.6 mA (current density 100 A/cm^2) were measured for 10 randomly selected pixels, as shown in figure 6.5(a). Analysis of the data reveals that the current and light output power variations are uniform to within ±10% and ±2%, respectively. The good pixel-to-pixel uniformity, especially for light output power, is attributed to the specially designed n-type Ti/Au contact, which fills the area between the micro-LEDs and facilitates uniform current distribution between pixels. Figure 6.5(b) compares the power density versus current density characteristics of a micro-LED and a 250 μm×250 μm broad-area LED. It is found that the micro-LED can sustain a high current density, up to 6.6 kA/cm^2 (105 mA), before thermal rollover, whereas the broad-area LED exhibits thermal saturation at

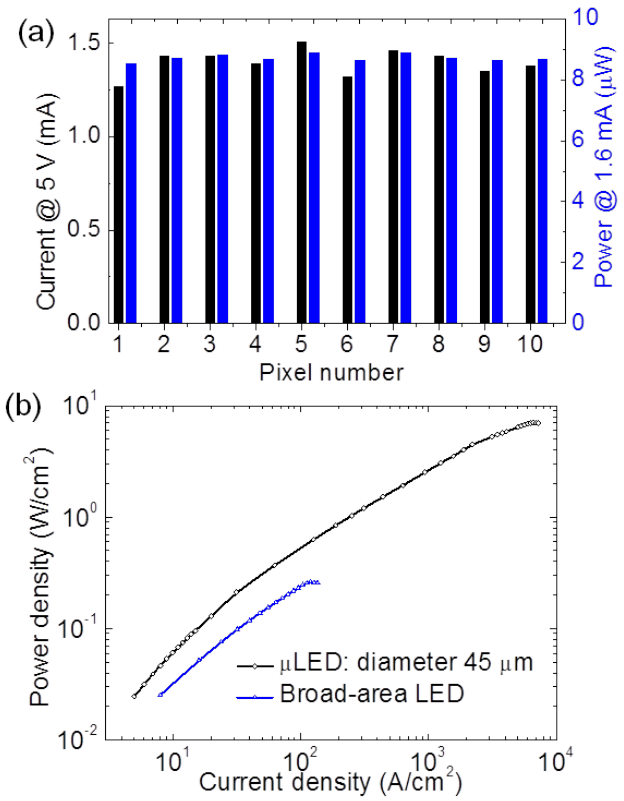

FIGURE 6.5: (a)Electrical and optical uniformity of 10 randomly selected pixels of a 10×10 micro-LED array. (b) Comparison of power density versus current density characteristics of micro-LED and broad-area LED.

only 120 A/cm^2. This behaviour is attributed to the advantages of more uniform current spreading in micro-LEDs and improved thermal management compared with broad-area LEDs [17–19].

6.4 Application in micro-displays

The good pixel-to-pixel uniformity, high light output power density, and individual addressability of the micro-LED arrays on Si substrates are all relevant to the applications in low-cost micro-displays. To illustrate these aspects of performance we present an EL spectrum and a micro-display pattern in figure 6.6. The EL spectrum (figure 6.6(a)) of one micro-LED shows that its maximum light output is around 470 nm at 1.6 mA under DC drive conditions. The multiple interference peaks are caused by the reflections at the various interfaces present, and the intensity variation between interference maxima and minima is substantial owing to the large refractive index contrasts at both

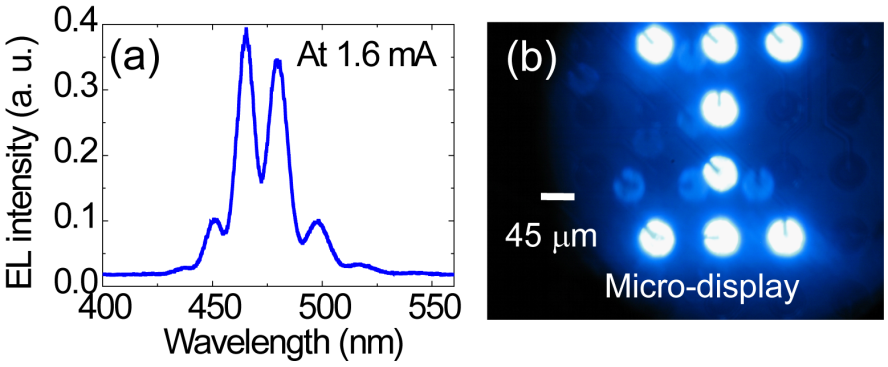

FIGURE 6.6: (a) EL spectrum and (b) light emission of a micro-display pattern of the 10×10 micro-LED array. A reflection pattern of letter "I", reflected by the cover glass on the package, can also be partly seen, and the dark lines seen with each pixel are due to the metal tracks.

the GaN/Si and air/GaN interfaces [29]. The EL spectra of 10 randomly selected pixels within an array were compared to check their uniformity, and the maxima of the corresponding interference peaks in different spectra are at wavelengths differing by less than the resolution of the spectrometer (∼0.3 nm). In any application where suppressions of these interference peaks were desirable, this could be achieved for top-emitting devices by growth on patterned substrates, and/or surface roughening [1]. Shown in figure 6.6(b) is a representative micro-display pattern of a capital letter "I", indicating that controllable pattern generation can be achieved through individually controlling each LED pixel. Within the pattern, the brightness of all 8 illuminated pixels is very consistent which confirms the uniform pixel-to-pixel electrical and optical characteristics.

6.5 Modulation bandwidths of GaN-on-Si micro-LEDs

It was previously reported that micro-LEDs exhibit very high electrical-to-optical (E-O) modulation bandwidths, compared to their broad-area counterparts, which we have attributed to their low capacitance and their ability to be operated at high current densities [22, 23]. Furthermore, the pixel addressing scheme also lends itself to future demonstrations of parallel data transmission for VLC applications [30], which partly motivates the current investigation of GaN-on-Si micro-LEDs. In this work, the E-O modulation bandwidth of a representative individual micro-LED was measured from 0.1 mA to 110 mA. Three stages of the variation of modulation bandwidth can be seen in figure 6.7(a). Firstly, the bandwidth of the micro-LED rapidly increases with injection

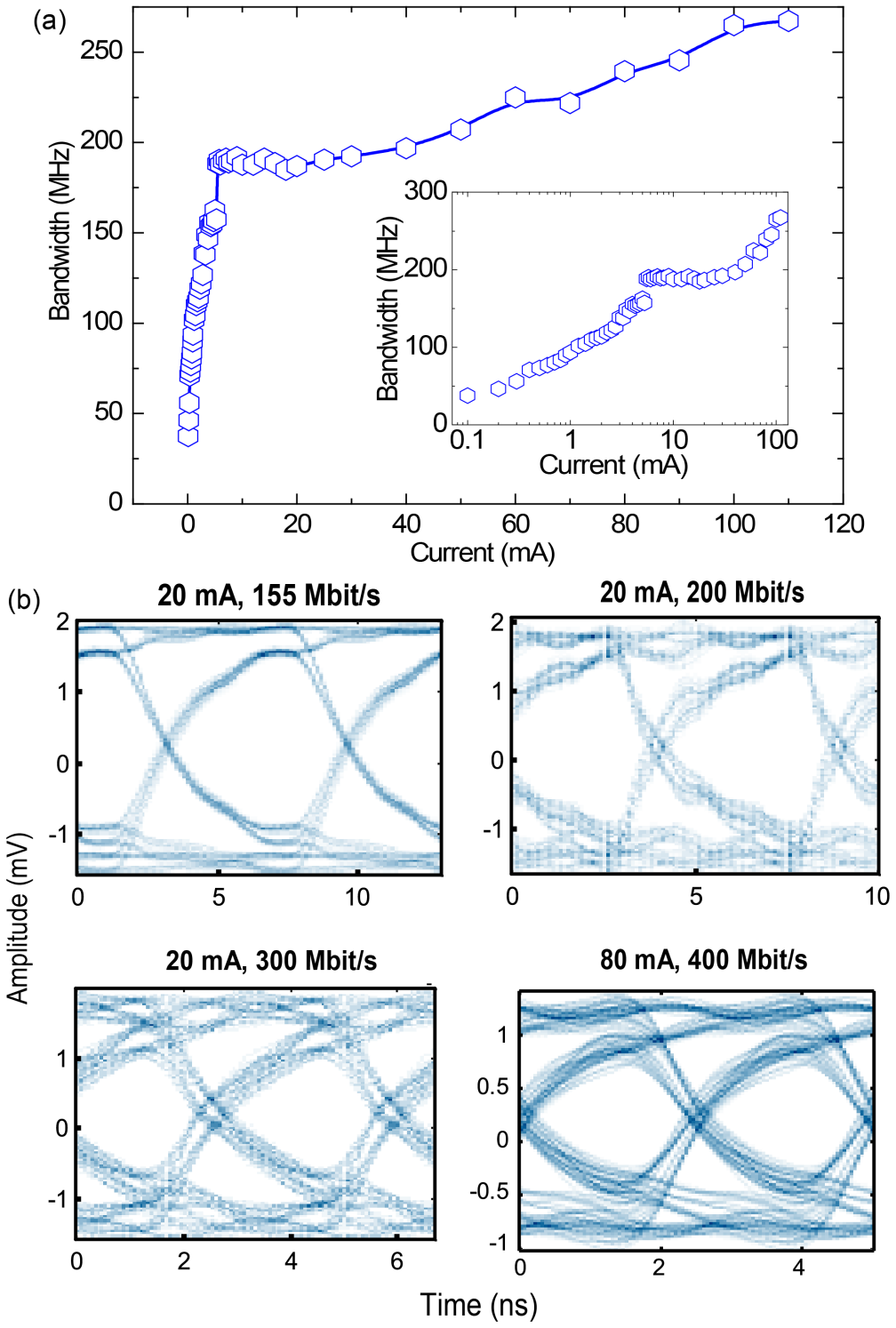

FIGURE 6.7: (a) Bandwidth of one representative micro-LED versus current. Inset: bandwidth versus log(current). (b) The eye diagrams taken at 155 Mbit/s (at 20 mA), 200 Mbit/s (at 20 mA), 300 Mbit/s (at 20 mA), and 400 Mbit/s (at 80 mA, smoothed).

current up to ∼6 mA, before saturating at ∼190 MHz. Secondly, the saturation of bandwidth continues from ∼6 mA to ∼35 mA. Finally, above ∼35 mA, a gradual increase of bandwidth to ∼270 MHz can be seen again until 110 mA. A clearer trend of the three stages can be seen in the inset to figure 6.7(a). Here, the bandwidth saturation current density 375 A/cm^2 (6 mA) of micro-LEDs is much higher than the thermal saturation current density of comparable broad-area LEDs, 120 A/cm^2. Assuming the bandwidth of micro-LEDs and broad-area LEDs are similar at the same current density [22], due to their higher sustainable current density micro-LEDs have advantages on E-O modulation for VLC applications.

A previous paper reported the modulation bandwidth of blue micro-LEDs on sapphire substrates with similar size [22]. For a 44 μm micro-LED on sapphire, a maximum bandwidth ∼435 MHz was achieved. In comparison, a 45 μm micro-LED on Si achieved a maximum bandwidth ∼270 MHz. The lower maximum bandwidth of micro-LEDs on Si substrates is attributed to the higher series resistance, which will be analysed in section 6.6. With optimization of micro-LED structures on Si substrate, the series resistance could be further reduced and higher bandwidths could be achieved.

In order to show the micro-LEDs can be used for data transmission, pseudo-random binary sequences were applied as modulation signals to individual LED pixels, and the resulting eye diagrams are shown in figure 6.7(b). Open eye diagrams at 155 Mbit/s, 200 Mbit/s, and 300 Mbit/s could be obtained at 20 mA. However, an open eye diagram at 400 Mbit/s is only obtained at higher currents, e.g. 80 mA, at which the micro-LEDs have higher modulation bandwidth and higher light output power. It is demonstrated that, to achieve high data transmission speed, both modulation bandwidth and light output power should be enhanced.

6.6 Mechanisms affecting modulation bandwidth

The sharp increase of modulation bandwidth at current less than ∼6 mA is attributed to the carrier recombination in the active region of the LEDs. To explore the underlying carrier recombination mechanisms related to the current dependent bandwidth, a rate equation model is employed to analyse the dominant mechanisms expected at different current ranges. Using the E-O -3dB bandwidth f_{3dB}, the differential lifetime τ can be

obtained from the equation $f_{3dB} = \sqrt{3}/2\pi\tau$. Then τ and the carrier concentration n can be related by the total rate R_{recom} of carrier recombination through equation [6, 31, 32]

$$\frac{1}{\tau(n)} = \frac{dR_{recom}(n)}{dn} = A + 2Bn + 3Cn^2 \tag{6.1}$$

where $R_{recom}(n) = An + Bn^2 + Cn^3$, and A, B, and C represent the coefficients for defect-related Shockley-Read-Hall (SRH) non-radiative recombination, radiative recombination, and cubic non-radiative recombination. The latter term is most commonly assumed to correspond to interband Auger processes in the InGaN active material [33], and its increasing significance at high current densities to account for the efficiency droop phenomenon [34, 35]. Supporting experimental evidence for this model comes from the work by Iveland et al [34], which recently reported direct emission into the vacuum from a cesiated LED structure of electrons whose characteristics matched the predictions of an Auger-mediated efficiency droop model. The sensitivity of Auger recombination to detailed band structure also promises mitigations through material design, as exemplified by recent theoretical studies of dilute-arsenide GaNAs material [36]. However, other analyses of nitride LED performance emphasise carrier leakage from quantum wells at high injection currents [37–39]. It is likely that the detailed balance of microscopic processes depends on specific device structures, and those other processes, including carrier delocalization [40], may play significant roles.

The carrier recombination processes are modelled to extract the fraction of each recombination and to identify the dominant recombination in different current/current density range. The previous work used bandwidth/differential lifetime to calculate the carrier concentration and further extracted the A, B, and C coefficients [31]. However, in this work the bandwidths at current larger than ~6 mA saturate and thus cannot be used for n calculation. Thus, the following model is employed. In this model, the light output power P can be expressed as $P = kBn^2$, and the parameter k is defined as $k = \eta_{EXE} h\upsilon V_{active}$, where η_{EXE} is light extraction efficiency, $h\upsilon$ is the photon energy, and V_{active} is the effective volume of active region (MQWs). So n can be expressed as $n = \sqrt{P/kB}$. Based on $I = qV_{active}R_{recom}(n)$, where q is the electron charge, the total current is given as follows

$$I = \frac{A}{\sqrt{kB}} qV_{active}\sqrt{P} + \frac{1}{k} qV_{active}\sqrt{P}^2 + \frac{C}{\sqrt{kB}^3} qV_{active}\sqrt{P}^3. \tag{6.2}$$

Thus, through a polynomial fit of I as a function of $\sqrt{P}$, the relative contributions of the different-order terms can be obtained. The fit has been adjusted by the peak internal quantum efficiency (η_{IQE}) ~20% of the 470 nm wafer at room temperature [41, 42], so either defect-related SRH non-radiative recombination or high-order non-radiative recombination will dominate over radiative recombination in the whole current range. As shown in figure 6.8, defect-related SRH recombination is dominant at very low current densities, below ~20 A/cm^2, after which high-order non-radiative recombination dominates. Fitting results after 500 A/cm^2 are not shown where high-order non-radiative recombination still dominates. These results agree with previous work that the non-radiative lifetime dominates at high current densities for GaN-based LEDs [43]. It should be noted that the phase space filling effect can cause the decrease of B and C coefficients at high current densities [31, 43], and as such assuming B and C coefficients as constants may induce some uncertainty at high current densities (roughly larger than ~100 A/cm^2). But the uncertainty will not affect the dominance of high-order non-radiative recombination at high current densities. The large fraction of high-order non-radiative recombination can reduce the η_{IQE} of LEDs, but contributes to a short differential lifetime and a large modulation bandwidth.

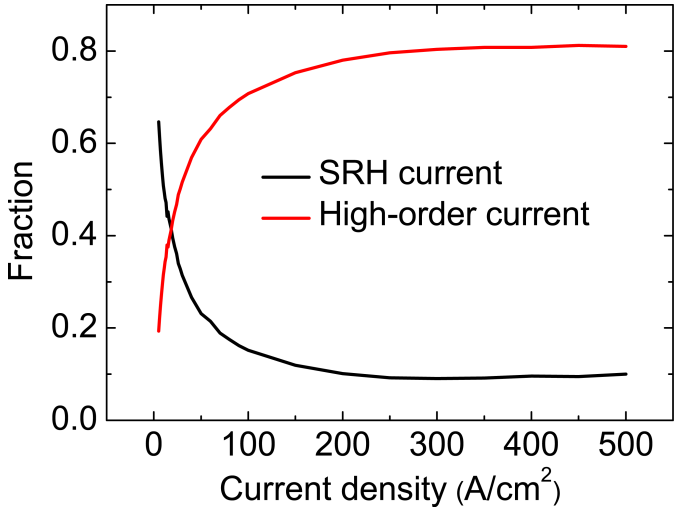

FIGURE 6.8: Fitted defect-related SRH current and high-order current fraction as a function of current density.

It has been shown that the current versus bandwidth behaviour of GaN-on-sapphire micro-LEDs can be described by equation 6.1 [31]. However, this equation cannot fully describe the bandwidth saturation from ~6 mA to ~35 mA and the further increase seen from ~35 mA, as shown in figure 6.7(a). Here it is assumed that at currents larger than 6 mA the current versus bandwidth trend is related to the $R_{series}C_D$ time constant that

is the product of the device capacitance C_D and a relatively high series resistance R_{series} of these micro-LEDs, compared to their GaN-on-sapphire counterparts. The gradual increase of modulation bandwidth from ~35 mA indicates that the $R_{series}C_D$ value may vary with current. To explore the underlying mechanism, the series resistance R_{series}, calculated from the *I-V* characteristics by $R_{series} = dV/dI$, is shown in figure 6.9. In comparing the series resistance in the low-current regime with values for comparable broad-area LEDs, a basic consideration is the approximate proportionality expected to D^{-2}, where D is the LED pixel diameter, as demonstrated in a previous study of devices on sapphire substrates [17]. Standard analysis of the contributions to series resistance from individual parts of the device points to the dominance of the resistances of *p*-contact, *p*-GaN and AlGaN current blocking layers for the top-emitting LED format studied here [44]. A secondary issue is that the *n*-GaN thickness is some 3-4 times less than is common in LED structures on sapphire, adding resistance to the current path between the *n*-metal and active region. However, this factor is not expected to enhance series resistance significantly with the *n*-metallisation scheme used. To reduce the series resistance in the future, combining optimization of the epitaxial structure and processing will be necessary. Below ~35 mA, the self-heating effect in micro-LEDs is not significant [17–19] and thus has little effect on the series resistance. Then, from ~35 mA (2.2 kA/cm^2), the self-heating effect causes an increase of junction temperature [17] and thus a decrease of series resistance in figure 6.9 due to the increased hole concentration,

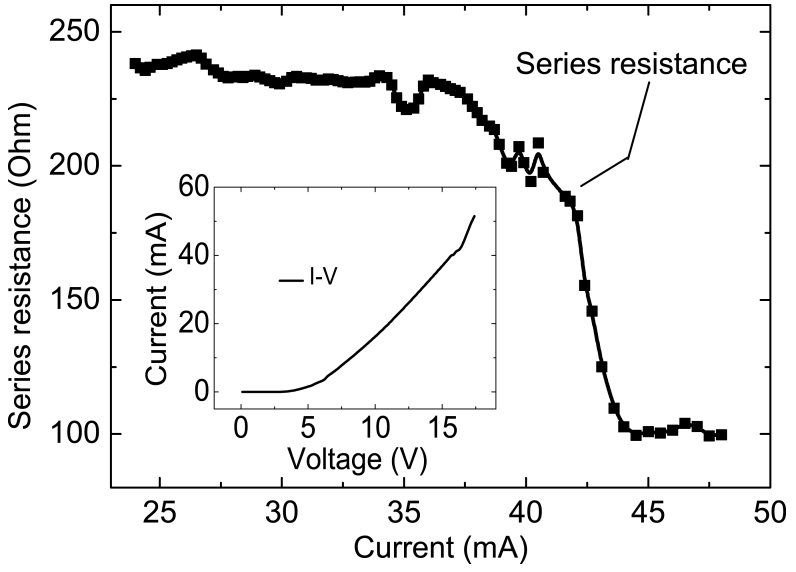

FIGURE 6.9: Series resistance of micro-LEDs with a reduction from ~35 mA. Inset: *I-V* characteristics of one micro-LED.

etc. [45] Thus, series resistance variation should be one important reason for the gradual increase of bandwidth from ~35 mA in figure 6.7(a). We recognize that the trend in series resistance is insufficient to fully explain the trend in modulation bandwidth, and the capacitance contribution will be studied using approaches reported elsewhere [46].

6.7 Summary

In summary, individually addressable 10×10 micro-LEDs arrays have been fabricated from GaN-based LED epistructures on Si. The electrical and optical properties of these new LED arrays were characterized and analysed. The good pixel-to-pixel uniformity and higher thermal saturation current density compared with broad-area LEDs demonstrate the devices are suitable for micro-displays, for which the growth on Si substrates offers advantages of cost and scalability. The high saturation current density, high power density and micro-scale pixel dimension also facilitate LED pixel fast optical modulation which is required for VLC application. A maximum optical modulation bandwidth of ~270 MHz and data transmission rate of pseudo-random binary sequences at up to 400 Mbit/s are obtained. The modulation bandwidth shows a characteristic three-stage dependence on current: an initial increase at low currents explained by carrier recombination, a region in which the bandwidth saturates near ~190 MHz, limited by the $R_{series}C_D$ parameter, and the final increase to ~270 MHz at the highest currents in which self-heating reduces the series resistance. These results demonstrate that the GaN-on-Si LED material is already suitable for specialized device applications in the micro-pixelated format, including micro-displays and data communications.

References

[1] D. Zhu, D. J. Wallis, and C. J. Humphreys. Prospects of III-nitride optoelectronics grown on Si. *Reports on Progress in Physics*, 76(10):106501, 2013.

[2] D. Zhu, C. McAleese, K. K. McLaughlin, M. Häberlen, C. O. Salcianu, E. J. Thrush, M. J. Kappers, W. A. Phillips, P. Lane, D. J. Wallis, T. Martin, M. Astles, S. Thomas, A. Pakes, M. Heuken, and C. J. Humphreys. GaN-based LEDs grown on 6-inch diameter Si (111) substrates by MOVPE. *Proceedings of SPIE*, 7231:723118, 2009.

[3] D. Zhu, C. McAleese, M. Häberlen, M. J. Kappers, N. Hylton, P. Dawson, G. Radtke, M. Couillard, G. A. Botton, S.-L. Sahonta, and C. J. Humphreys. High-efficiency InGaN/-GaN quantum well structures on large area silicon substrates. *Physica Status Solidi (a)*, 209(1):13–16, 2012.

[4] A. Dadgar, C. Hums, A. Diez, J. Bläsing, and A. Krost. Growth of blue GaN LED structures on 150-mm Si (111). *Journal of Crystal Growth*, 297(2):279–282, 2006.

[5] A. Dadgar, F. Schulze, M. Wienecke, A. Gadanecz, J. Bläsing, P. Veit, T. Hempel, A. Diez, J. Christen, and A. Krost. Epitaxy of GaN on silicon-impact of symmetry and surface reconstruction. *New Journal of Physics*, 9(10):389, 2007.

[6] B. Galler, P. Drechsel, R. Monnard, P. Rode, P. Stauss, S. Froehlich, W. Bergbauer, M. Binder, M. Sabathil, B. Hahn, and J. Wagner. Influence of indium content and temperature on Auger-like recombination in InGaN quantum wells grown on (111) silicon substrates. *Applied Physics Letters*, 101(13):131111, 2012.

[7] F. W. Smith and G. Ghidini. Reaction of oxygen with Si (111) and (100): critical conditions for the growth of SiO_2. *Journal of the Electrochemical Society*, 129(6):1300–1306, 1982.

[8] W. E. Fenwick, A. Melton, T. Xu, N. Li, C. Summers, M. Jamil, and I. T. Ferguson. Metal organic chemical vapor deposition of crack-free GaN-based light emitting diodes on Si (111) using a thin Al_2O_3 interlayer. *Applied Physics Letters*, 94(22):222105, 2009.

[9] J. Komiyama, Y. Abe, S. Suzuki, and H. Nakanishi. Stress reduction in epitaxial GaN films on Si using cubic SiC as intermediate layers. *Journal of Applied Physics*, 100(3):033519, 2006.

[10] R. Armitage, Q. Yang, H. Feick, J. Gebauer, E. R. Weber, S. Shinkai, and K. Sasaki. Lattice-matched HfN buffer layers for epitaxy of GaN on Si. *Applied Physics Letters*, 81(8): 1450–1452, 2002.

[11] L. Dobos, B. Pecz, E. Feltin, B. Beaumont, and P. Gibart. Microstructure of GaN layers grown on Si (111) revealed by TEM. *Vacuum*, 71(1):285–291, 2003.

[12] G. Radtke, M. Couillard, G. A. Botton, D. Zhu, and C. J. Humphreys. Structure and chemistry of the Si (111)/AlN interface. *Applied Physics Letters*, 100(1):011910, 2012.

[13] B. Zhang, H. Liang, Y. Wang, Z. Feng, K. W. Ng, and K. M. Lau. High-performance III-nitride blue LEDs grown and fabricated on patterned Si substrates. *Journal of Crystal Growth*, 298:725–730, 2007.

[14] J. E. Ayers. Compliant substrates for heteroepitaxial semiconductor devices: theory, experiment, and current directions. *Journal of Electronic Materials*, 37(10):1511–1523, 2008.

[15] M. J. Kappers, R. Datta, R. A. Oliver, F. D. G. Rayment, M. E. Vickers, and C. J. Humphreys. Threading dislocation reduction in (0001) GaN thin films using SiN_x interlayers. *Journal of Crystal Growth*, 300(1):70–74, 2007.

[16] Osram. Osram Opto unveils R&D results from GaN LEDs grown on silicon. `http://ledsmagazine.com/news/9/1/19`, 2012.

[17] Z. Gong, S. Jin, Y. Chen, J. McKendry, D. Massoubre, I. M. Watson, E. Gu, and M. D. Dawson. Size-dependent light output, spectral shift, and self-heating of 400 nm InGaN light-emitting diodes. *Journal of Applied Physics*, 107(1):013103, 2010.

[18] T. I. Kim, Y. H. Jung, J. Song, D. Kim, Y. Li, H. S. Kim, I. S. Song, J. J. Wierer, H. A. Pao, Y. Huang, and J. A. Rogers. High-efficiency, microscale GaN light-emitting diodes and their thermal properties on unusual substrates. *Small*, 8(11):1643–9, 2012.

[19] P. Tian, J. J. D. McKendry, Z. Gong, B. Guilhabert, I. M. Watson, E. Gu, Z. Chen, G. Zhang, and M. D. Dawson. Size-dependent efficiency and efficiency droop of blue InGaN micro-light emitting diodes. *Applied Physics Letters*, 101(23):231110, 2012.

[20] J. Day, J. Li, D. Y. C. Lie, C. Bradford, J. Y. Lin, and H. X. Jiang. III-Nitride full-scale high-resolution microdisplays. *Applied Physics Letters*, 99(3):031116, 2011.

[21] Z. Y. Fan, J. Y. Lin, and H. X. Jiang. III-nitride micro-emitter arrays: development and applications. *Journal of Physics D: Applied Physics*, 41(9):094001, 2008.

[22] J. J. D. McKendry, D. Massoubre, S. Zhang, B. R. Rae, R. P. Green, E. Gu, R. K. Henderson, A. E. Kelly, and M. D. Dawson. Visible-light communications using a CMOS-controlled micro-light-emitting-diode array. *Journal of Lightwave Technology*, 30(1):61–67, 2012.

[23] J. J. D. McKendry, R. P. Green, A. E. Kelly, Z. Gong, B. Guilhabert, D. Massoubre, E. Gu, and M. D. Dawson. High-speed visible light communications using individual pixels in a micro light-emitting diode array. *IEEE Photonics Technology Letters*, 22(18):1346–1348, 2010.

[24] P. P. Maaskant, H. Shams, M. Akhter, W. Henry, M. J. Kappers, D. Zhu, C. J. Humphreys, and B. Corbett. High-speed substrate-emitting micro-light-emitting diodes for applications requiring high radiance. *Applied Physics Express*, 6(2):2102, 2013.

[25] B. Guilhabert, D. Massoubre, E. Richardson, J. J. D. McKendry, R. K. Henderson, I. M. Watson, E. Gu, and M. D. Dawson. Sub-micron lithography using InGaN micro-LEDs: mask-free fabrication of LED arrays. *IEEE Photonics Technology Letters*, 24(24):2221–2224, 2012.

[26] V. Poher, N. Grossman, G. T. Kennedy, K. Nikolic, H. X. Zhang, Z. Gong, E. M. Drakakis, E. Gu, M. D. Dawson, P. M. W. French, P. Degenaar, and M. A. A. Neil. Micro-LED arrays: a tool for two-dimensional neuron stimulation. *Journal of Physics D: Applied Physics*, 41 (9):094014, 2008.

[27] M. Scanziani and M. Häusser. Electrophysiology in the age of light. *Nature*, 461(7266): 930–939, 2009.

[28] A. Zarowna-Dabrowska, S. L. Neale, D. Massoubre, J. McKendry, B. R. Rae, R. K. Henderson, M. J. Rose, H. Yin, J. M Cooper, E. Gu, and M. D. Dawson. Miniaturized optoelectronic tweezers controlled by GaN micro-pixel light emitting diode arrays. *Optics Express*, 19(3):2720–2728, 2011.

[29] C. Hums, T. Finger, T. Hempel, J. Christen, A. Dadgar, A. Hoffmann, and A. Krost. Fabry-Perot effects in InGaN/ GaN heterostructures on Si-substrate. *Journal of Applied Physics*, 101(3):033113, 2007.

[30] S. Zhang, S. Watson, J. J. D. McKendry, D. Massoubre, A. Cogman, E. Gu, R. K. Henderson, A. E. Kelly, and M. D. Dawson. 1.5 Gbit/s multi-channel visible light communications using CMOS-controlled GaN-based LEDs. *Journal of Lightwave Technology*, 31(8):1211–1216, 2013.

[31] R. P. Green, J. J. D. McKendry, D. Massoubre, E. Gu, M. D. Dawson, and A. E. Kelly. Modulation bandwidth studies of recombination processes in blue and green InGaN quantum well micro-light-emitting diodes. *Applied Physics Letters*, 102(9):091103, 2013.

[32] R. Olshansky, C. Su, J. Manning, and W. Powazinik. Measurement of radiative and non-radiative recombination rates in InGaAsP and AlGaAs light sources. *IEEE Journal of Quantum Electronics*, 20(8):838–854, 1984.

[33] K. T. Delaney, P. Rinke, and C. G. Van de Walle. Auger recombination rates in nitrides from first principles. *Applied Physics Letters*, 94(19):191109, 2009.

[34] J. Iveland, L. Martinelli, J. Peretti, J. S. Speck, and C. Weisbuch. Direct measurement of Auger electrons emitted from a semiconductor light-emitting diode under electrical injection: identification of the dominant mechanism for efficiency droop. *Physical Review Letters*, 110 (17):177406, 2013.

[35] Y. C. Shen, G. O. Mueller, S. Watanabe, N. F. Gardner, A. Munkholm, and M. R. Krames. Auger recombination in InGaN measured by photoluminescence. *Applied Physics Letters*, 91(14):141101, 2007.

[36] C.-K. Tan, J. Zhang, X.-H. Li, G. Liu, B. O. Tayo, and N. Tansu. First-principle electronic properties of dilute-As GaNAs alloy for visible light emitters. *Journal of Display Technology*, 9(4):272–279, 2013.

[37] D. S. Meyaard, G.-B. Lin, J. Cho, E. F. Schubert, H. Shim, S.-H. Han, M.-H. Kim, C. Sone, and Y. S. Kim. Identifying the cause of the efficiency droop in GaInN light-emitting diodes by correlating the onset of high injection with the onset of the efficiency droop. *Applied Physics Letters*, 102(25):251114, 2013.

[38] H. Zhao, G. Liu, J. Zhang, R. A. Arif, and N. Tansu. Analysis of internal quantum efficiency and current injection efficiency in III-nitride light-emitting diodes. *Journal of Display Technology*, 9(4):212–225, 2013.

[39] I. E. Titkov, D. A. Sannikov, Y.-M. Park, and J.-K. Son. Blue light emitting diode internal and injection efficiency. *AIP Advances*, 2(3):032117, 2012.

[40] J. Hader, J. V. Moloney, and S. W. Koch. Temperature-dependence of the internal efficiency droop in GaN-based diodes. *Applied Physics Letters*, 99(18):181127, 2011.

[41] D. Zhu, C. McAleese, M. Haberlen, C. Salcianu, M. Thrush, T.and Kappers, A. Phillips, M. Lane, P.and Kane, D. Wallis, T. Martin, M. Astles, N. Hylton, P. Dawson, and C. Humphreys. Efficiency measurement of GaN-based quantum well and light-emitting diode structures grown on silicon substrates. *Journal of Applied Physics*, 109(1):014502, 2011.

[42] D. Zhu, C. McAleese, M. Häberlen, C. Salcianu, T. Thrush, M. Kappers, A. Phillips, P. Lane, M. Kane, D. Wallis, T. Martin, M. Astles, and C. Humphreys. InGaN/GaN LEDs

grown on Si (111): dependence of device performance on threading dislocation density and emission wavelength. *Physica Status Solidi (c)*, 7(7-8):2168–2170, 2010.

[43] A. David and M. J. Grundmann. Droop in InGaN light-emitting diodes: a differential carrier lifetime analysis. *Applied Physics Letters*, 96(10):103504, 2010.

[44] X. Guo and E. F. Schubert. Current crowding in GaN/InGaN light emitting diodes on insulating substrates. *Journal of Applied Physics*, 90(8):4191–4195, 2001.

[45] Y. Xi and E. F. Schubert. Junction–temperature measurement in GaN ultraviolet light-emitting diodes using diode forward voltage method. *Applied Physics Letters*, 85(12):2163–2165, 2004.

[46] C. Y. Zhu, L. F. Feng, C. D. Wang, H. X. Cong, G. Y. Zhang, Z. J. Yang, and Z. Z. Chen. Negative capacitance in light-emitting devices. *Solid-State Electronics*, 53(3):324–328, 2009.

Chapter 7

Summary and perspective

7.1 Summary

This thesis gives a systematic study of fabrication, efficiency and applications of GaN-based micro-pixelated light emitting diodes (micro-LEDs). At the beginning, the history of LED was reviewed, and fabrication and characterization techniques in this work were detailed. In following chapters, the size dependence and temperature dependence of the micro-LED efficiency have been analysed, suggesting related efficiency droop mechanisms and also demonstrating superior advantages of micro-LEDs over broad-area LEDs. Then, micro-LEDs on Si substrates and flexible substrates were fabricated, which helps to reduce the device cost and to expand the applications of the micro-LEDs, respectively.

Chapter 1 introduced the LED development history, GaN-based LEDs and the LED efficiency research. LED based white-light sources are expected to replace traditional incandescent and fluorescent sources for general lighting. GaN-based LEDs contribute significantly to improve the LED efficiency across the visible spectrum, although problems still exist such as the "green gap". The growth, chip design, packaging and applications of GaN-based broad-area LEDs were presented. Fabrication technologies of micro-LEDs are partly compatible with broad-area LEDs, and the micro-LEDs have special applications, such as micro-displays and visible light communication. The efficiency droop section started with the basic LED operation principles regarding electrical and optical characteristics, and reviewed the research progresses of efficiency droop. Defect-assisted recombination, reduction of radiation recombination with increasing current

density, Auger recombination, and electron leakage are the possible mechanisms leading to efficiency droop. The corresponding efficiency droop remedies were also introduced.

In chapter 2, the LED fabrication techniques were detailed, including the processing principles of photolithography, dry and wet etchings, metal depositions by electron beam evaporation and sputtering, rapid thermal annealing, plasma enhanced chemical vapour deposition for SiO_2 deposition, metal bonding and laser lift-off. Then, the characterization techniques for photoluminescence and LED modulation tests were described.

The micro-LED efficiency droop characteristics were analysed in Chapter 3 concerning the size dependence and in Chapter 4 concerning the temperature dependence. The micro-LEDs with smaller sizes have uniform current spreading and superior heat dissipation capability, leading to their higher efficiency at same current densities and higher thermal saturation current densities. However, sidewall defects may degrade the micro-LED efficiency at low current densities, which can be recovered by increasing thermal annealing time. Regarding the temperature dependence of micro-LEDs, an ABC model was used to extract the carrier recombination coefficients. With increasing temperature, the defect-related Shockley-Read-Hall (SRH) recombination coefficient increases, while the radiative and Auger recombination coefficients decrease. The temperature dependence of the radiative and Auger recombination coefficients is weaker at high current densities, which agrees with the published theoretical work well. The phase spacing filling effect is the key factor which induces the temperature dependence at different current densities. These efficiency analyses of micro-LEDs demonstrate the advantages of micro-LEDs. Compared with broad-area LEDs, the micro-LEDs have higher efficiency and higher thermal saturation current density, and can achieve stabler efficiency at different temperatures when operating at a very high current density.

Due to the superior characteristics, the micro-LEDs have been fabricated on flexible substrates and Si substrates for applications in micro-displays and visible light communication. In chapter 5, the flexible broad-area LEDs were fabricated by metal bonding and laser lift-off with only one transfer step, which can be bent to a bending radius $\sim$3.5 mm with uniform light emission within the LED die, but the light output power shows degradation at high current under smaller bending radii. The blue EL peak shift under bending states is related to the piezoelectric field change in multiple quantum wells (MQWs). Then the flexible micro-LEDs were fabricated which showed potential

applications in flexible micro-displays and visible light communication. In chapter 6, micro-LEDs on Si substrates have been fabricated which can reduce the cost of micro-LEDs and expand their market. The applications in micro-displays and visible light communication were also demonstrated. The analysis of modulation bandwidth suggests the series resistance of micro-LEDs can limit the possible maximum bandwidth, and thus should be minimized.

7.2 Perspective

Based on the analyses of micro-LED efficiency droop in Chapters 3 and 4, it is possible to develop high-efficiency LEDs and LEDs with stable temperature-dependent efficiency for solid state lighting (SLL). The cluster LEDs have been developed employing micro-LEDs to improve the light output power/efficiency [1]. However, the commonly used sapphire substrates and the gap between the micro-LED pixels affect the heat dissipation of these micro-LEDs, so the fabricated cluster micro-LED device will have weaker heat dissipation ability than a single micro-LED pixel. Several methods can help to solve this problem. First, the cluster vertical micro-LED array can be developed through transferring the micro-LED pixels to other substrates with high heat dissipation ability. Laser lift-off or wet chemical etching are commonly used techniques to remove original substrates for LEDs grown on sapphire or Si substrates, respectively. Another method is to enlarge the gap between these pixels, but the LED material in the gap will be wasted and the fabrication cost will increase. To minimize the wafer cost, transfer printing can be employed to pick each micro-LED pixel from the initial substrate and then spread them on other substrates [2]. These methods can help to design LEDs with higher efficiency and higher thermal saturation current densities. In addition, the higher operation current densities lead to weaker temperature dependence of LED efficiency.

In addition, the temperature-dependent efficiency droop study in Chapter 4 could be expanded to more devices with different QW designs, i.e. structures with different carrier confinement. Since the QW structures have significant effect on the extracted value of Auger recombination coefficient, it is possible to suppress the Auger recombination and achieve stable temperature-dependent Auger recombination through special design of QWs [3].

Besides the SSL application by using micro-LEDs, the micro-LEDs can be used for other applications. Flexible micro-LEDs have been demonstrated in Chapter 5. Their bio-compatibility enables the future applications in biomedicine [4]. Their flexibility also helps to develop hybrid device through combining the flexible LEDs and organic material together [5]. For micro-LEDs on Si substrates as shown in Chapter 6, as the Si substrates can be easily removed by wet chemical etching or mechanical polishing, it is possible to transfer the micro-LEDs onto other substrates, e.g. flexible substrates. Then, special structures on n-GaN, e.g. photonic crystal structure, can be developed to improve the LED efficiency.

References

[1] N. L. Ploch, H. Rodriguez, C. Stölmacker, M. Hoppe, M. Lapeyrade, J. Stellmach, F. Mehnke, T. Wernicke, A. Knauer, V. Kueller, M. Weyers, S. Einfeldt, and M. Kneissl. Effective thermal management in ultraviolet light-emitting diodes with micro-LED arrays. *IEEE Transactions on Electron Devices*, 60(2):782–786, 2013.

[2] H.-S. Kim, E. Brueckner, J. Song, Y. Li, S. Kim, C. Lu, J. Sulkin, K. Choquette, Y. Huang, R. G. Nuzzo, and J. A. Rogers. Unusual strategies for using indium gallium nitride grown on silicon (111) for solid-state lighting. *Proceedings of the National Academy of Sciences*, 108 (25):10072–10077, 2011.

[3] R. Vaxenburg, E. Lifshitz, and Al. L. Efros. Suppression of Auger-stimulated efficiency droop in nitride-based light emitting diodes. *Applied Physics Letters*, 102(3):031120, 2013.

[4] S. Y. Lee, K.-I. Park, C. Huh, M. Koo, H. G. Yoo, S. Kim, C. S. Ah, G. Y. Sung, and K. J. Lee. Water-resistant flexible GaN LED on a liquid crystal polymer substrate for implantable biomedical applications. *Nano Energy*, 1(1):145–151, 2012.

[5] J. Herrnsdorf, B. Guilhabert, J. J. D. McKendry, Z. Gong, D. Massoubre, S. Zhang, S. Watson, A. E. Kelly, E. Gu, N. Laurand, and M. D. Dawson. Hybrid organic/GaN photonic crystal light-emitting diode. *Applied Physics Letters*, 101(14):141122, 2012.